DTU Nanotech
Department of Micro- and Nanotechnology

Master Thesis, s062104

Acoustofluidics in microsystems: investigation of acoustic streaming

Peter Barkholt Muller

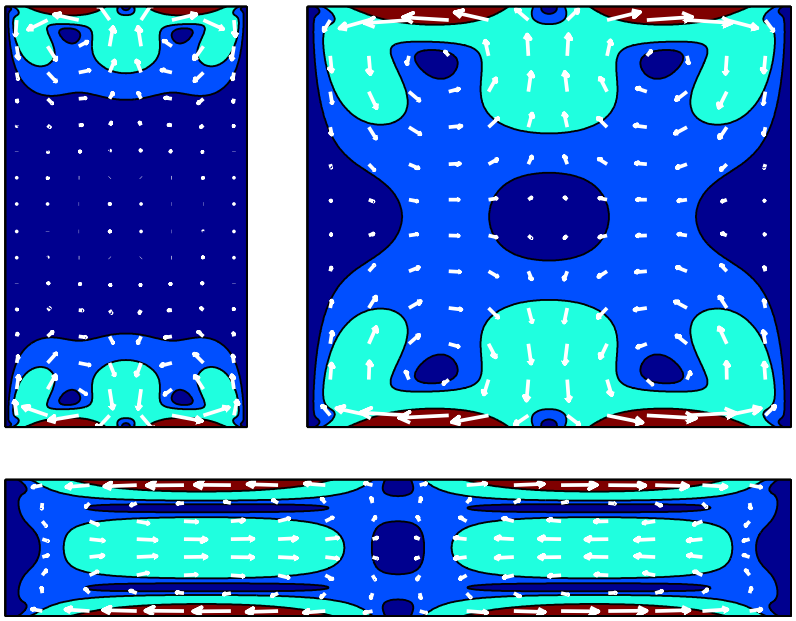

Supervisor: Professor Henrik Bruus

Department of Micro– and Nanotechnology
Technical University of Denmark

12 March 2012

Frontpage illustration
The illustration at the frontpage shows color and vector plot of the acoustic streaming velocity field in the vertical cross-sectional plane of three rectangular channels with different aspect ratios.

Abstract

During the past decade applications for particle and fluid handling using acoustic forces in microfluidic systems have received an increasing interest. Some devices utilize direct momentum transfer from the acoustic wave to the suspended particles, in terms of the acoustic radiation force, while others utilize momentum transfer from the acoustic wave to the fluid, in terms of the acoustic streaming. In the present work we investigate the phenomena of acoustic streaming in microfluidic systems through analytical analysis and numerical simulations. All models proposed in this work are based on a perturbation method to second order of isothermal systems.

Motivated by an inconsistency in the common analytical approach to the problem of acoustic streaming, we propose a novel approach, in which the flow close to the boundaries is considered compressible. The novel approach leads to an acoustic streaming boundary condition for the bulk flow in agreement with results reported by Rayleigh [1]. Rayleigh's derivation of the acoustic streaming velocity field is valid only for a thin parallel-plates channel, in which the distance between the plates is much smaller than the acoustic wavelength, however, it is often used for comparison with experimental systems well beyond this assumption. We present the theory for acoustic streaming in a high parallel-plates channel, in which the distance between the plates is comparable to the acoustic wavelength. The theory is extended to account for the effect of the side walls of a rectangular channel, an effect so far neglected in the theory of acoustic streaming. This effect is important for the acoustic streaming in near quadratic microfluidics channels, typically used in acoustofluidic systems. We propose an iterative Fourier expansion approach, by which we determine the acoustic streaming velocity field for the rectangular channel to arbitrary high precision. This allows for prediction of the acoustic streaming in experimental acoustofluidic devices, presenting an important contribution to the theory of acoustic streaming and to the acoustofluidic research field.

In addition to the analytical work, we present numerical simulations of acoustic streaming in rectangular channels. The tendency of the numerical solutions are in agreement with the analytical results, with deviations close to the boundaries. The analytical iterative Fourier expansion approach is validated by comparison to a simple numerical model, based on the analytical acoustic streaming boundary condition for the bulk flow.

Resumé

Op gennem det sidste årti har der været en stigende interesse omkring anvendelsen af akustiske kræfter til at kontrollere partikler og væsker i mikrofluid systemer. Nogle systemer anvender direkte overførsel af impuls fra den akustiske bølge til partikler i form af den akustiske strålingskraft, mens andre anvender impulsoverførsel fra den akustiske bølge til væsken i form af den akustiske strømning. I denne afhandling undersøger vi den akustiske strømning i mikrofluid systemer gennem analytisk analyse og numeriske simuleringer. Alle præsenterede modeller er baseret på en perturbationsmetode til anden orden af isoterme systemer.

Motiveret af en inkonsistens in den gængse analytiske tilgang til den akustiske strømning, præsenterer vi en ny tilgang, i hvilken strømningen tæt på væggene betragtes som værende kompressibel. Denne nye tilgang leder til en akustisk strømningsgrænsebetingelse for væskestrømningen, der stemmer overens med resultater rapporteret af Rayleigh [1]. Rayleighs udledning af det akustiske strømningshastighedsfelt er kun gyldig for strømningen mellem to parallelle plader, når afstanden mellem pladerne er meget mindre end den akustiske bølgelængde. Alligevel anvendes den ofte til at sammenligne med eksperimentelle systemer, der ikke opfylder denne antagelse. Vi præsenterer teorien for den akustiske strømning mellem to parallelle plader, hvor afstanden mellem pladerne er sammenlignelig med den akustiske bølgelængde. Teorien videreudvikles til at tage højde for effekten af sidevæggene i en rektangulær kanal, en effekt der hidtil er blevet negligeret i teorien for den akustiske strømning. Denne effekt er betydningsfuld for den akustiske strømning i nær kvadratiske mikrofluid kanaler, som typisk anvendes i akustiske mikrofluid systemer. Vi præsenterer en iterativ Fourier ekspansions tilgang, med hvilken vi bestemmer den akustiske strømning i en rektangulær kanal til arbitrær høj præcision. Dette muliggør forudsigelse af den akustiske strømning i eksperimentelle akustiske mikrofluid systemer, og er derved et vigtig bidrag til teorien omkring den akustiske strømning.

Udover det analytiske arbejde præsenterer vi numeriske simuleringer af den akustiske strømning i rektangulære kanaler. Tendensen i den numeriske løsning stemmer overens med de analytiske resultater, men afviger tæt på væggene. Den analytiske iterative Fourier ekspansions tilgang valideres ved sammenligning med en simpel numerisk model baseret på den analytiske akustiske strømningsgrænsebetingelse for væskestrømningen.

Preface

This thesis is submitted as fulfillment of the prerequisites for obtaining the degree in Master of Science in Engineering at the Technical University of Denmark (DTU). The thesis work is carried out at the Department of Micro- and Nanotechnology (DTU Nanotech) in the Theoretical Microfluidics group (TMF) headed by Professor Henrik Bruus. The duration of the thesis work was 6 months from 12 September 2011 to 12 March 2012 corresponding to a credit of 30 ECTS points.

During the project work many people have been of great help and support. First of all, I would like to thank my supervisor Henrik Bruus for outstanding supervision and motivation. Henrik has been of great inspiration to me with his huge enthusiasm about physics.

During this project I have visited the group of Professor Thomas Laurell at the Department of Electrical Measurements (Elmat), Lund University (LTH), on several occasions. I would like to thank them, especially PhD Per Augustsson, for great discussions and insight into the experimental world of acoustofluidics. I enjoy the collaboration with our Swedish "kompisar" and the great Swedish food, and I look forward to further collaboration in my continuation of the project as a PhD student.

I would also like to thank all members of the TMF group for great discussions and fun. A special thanks goes to PhD student Rune Barnkob, my acoustic-brother, for always keeping a positive and energetic attitude.

I would like to thank my family and friends for their support and shared enthusiasm about physics, especially June Holm Rasmussen for proofreading this thesis.

At last I would like to express my gratitude to my loving wife Line Muller Tribler. She has been an immense support throughout this project and all of my studies.

Peter Barkholt Muller
Department of Micro– and Nanotechnology
Technical University of Denmark
12 March 2012

Contents

List of Figures

List of symbols

Symbol	Description	Unit/value
$\equiv$	Equal to by definition	
$\sim$	Of the same order	
$\approx$	Approximately equal to	
α	Proportional to	
$\gg, \ll$	Much greater than, much smaller than	
$\cdot$	Scalar product	
$\times$	Cross-product or multiplication sign	
$\partial_i = \partial/\partial_i$	Partial derivative with respect to i	$[i]^{-1}$
$\boldsymbol{\nabla}$	Nabla or gradient vector operator	m^{-1}
$\boldsymbol{\nabla}\cdot$	Divergence vector operator	m^{-1}
$\boldsymbol{\nabla}\times$	Rotation vector operator	m^{-1}
∇^2	Laplacian scalar operator	m^{-2}
$\langle\circ\rangle$	Time average of $\circ$	
$\lvert\circ\rvert$	Absolute value of $\circ$	
$(\circ)^*$	Complex conjugate of $\circ$	
$\mathrm{Re}\{\circ\}$	Real part of $\circ$	
$\mathrm{Im}\{\circ\}$	Imaginary part of $\circ$	
i	Imaginary unit	
e	Euler's number, $\ln(\mathrm{e}) = 1$	
$\mathcal{O}(\circ)$	Terms of relative order $\circ$ or lower	
x, y, z	Rectangular coordinates	m
$\mathbf{e}_i$	Unit vector in the i-direction	
$\boldsymbol{r}$	Position vector	m
$\boldsymbol{n}$	Surface normal vector	m

Continued on next page

Symbol	Description	Unit/value
Ω	Domain	
$\partial\Omega$	Boundary of domain Ω	
p_i	i'th order pressure	$\mathrm{kg\,m^{-1}\,s^{-2}}$
ρ_i	i'th order mass density	$\mathrm{kg\,m^{-3}}$
v_i	i'th order velocity	$\mathrm{m\,s^{-1}}$
$\boldsymbol{v}_i$	i'th order velocity vector	$\mathrm{m\,s^{-1}}$
t	Time	s
f	Frequency	$\mathrm{s^{-1}}$
$\omega = 2\pi f$	Angular frequency	$\mathrm{s^{-1}}$
η	Dynamic viscosity	$\mathrm{kg\,m^{-1}\,s^{-1}}$
$\beta = \frac{1}{3}$	Viscosity ratio, value for simple fluids	
$\nu = \eta/\rho_0$	Kinematic viscosity	$\mathrm{m^2\,s^{-1}}$
λ	Acoustic wavelength	m
$\delta = \sqrt{2\nu/\omega}$	thickness of the viscous acoustic boundary layer	m
h	height of channel	m
w	width of channel	m
c	speed of sound, Isentropic	$\mathrm{m\,s^{-1}}$
$k = 2\pi/\lambda$	Wave number	$\mathrm{m^{-1}}$
$\boldsymbol{k}$	Wave vector	$\mathrm{m^{-1}}$
$\kappa = (1 - \mathrm{i})/\delta$	Acoustic decay constant	$\mathrm{m^{-1}}$
l	Characteristic length scale	m
τ	Characteristic time scale	s
$\rho' = \rho - \rho_0$	non-constant part of ρ	$\mathrm{kg\,m^{-3}}$
$\epsilon = \frac{1}{2}k^2\delta^2$	Characteristic number in acoustofluidics	
$\gamma = \frac{1+\beta}{2}\epsilon$	Viscous damping factor	
$\boldsymbol{U}_1$	First-order bulk velocity field	$\mathrm{m\,s^{-1}}$
$\boldsymbol{u}_1$	First-order boundary velocity field	$\mathrm{m\,s^{-1}}$
$\boldsymbol{U}_2$	Second-order bulk velocity field	$\mathrm{m\,s^{-1}}$
$\boldsymbol{u}_2$	Second-order boundary velocity field	$\mathrm{m\,s^{-1}}$
Ψ_2	Second-order bulk stream function	$\mathrm{m^2\,s^{-1}}$
ψ_2	Second-order boundary stream function	$\mathrm{m^2\,s^{-1}}$
ϕ_2	Second-order boundary velocity potential	$\mathrm{m^2\,s^{-1}}$
Q_2	Second-order pressure, homogeneous solution	$\mathrm{kg\,m^{-1}\,s^{-2}}$

Continued on next page

Symbol	Description	Unit/value
X_2	Second-order pressure, particular bulk solution	$\mathrm{kg\,m^{-1}\,s^{-2}}$
χ_2	Second-order pressure, particular boundary solution	$\mathrm{kg\,m^{-1}\,s^{-2}}$
$\zeta = \boldsymbol{\nabla} \times \boldsymbol{v}$	Vorticity	$\mathrm{s^{-1}}$
S	Vorticity source density	$\mathrm{s^{-2}}$
u_0	Amplitude of first-order bulk velocity field	$\mathrm{m\,s^{-1}}$
$u_{\mathrm{str}} = \frac{3}{8}\frac{u_0^2}{c}$	Acoustic streaming velocity	$\mathrm{m\,s^{-1}}$
$\alpha = kh$	Scaled aspect ratio of channel	
$\Gamma(\alpha)$	Geometry dependent scaling factor	
d_{rc}	Distance from channel wall to rotation center of $\langle U_{2x} \rangle$	m
d_{min}	Distance from channel wall to local minimum in $\langle U_{2x} \rangle$	m
$U_{2x,\mathrm{min}}$	$\langle U_{2x} \rangle$ at local minimum.	$\mathrm{m\,s^{-1}}$
$\langle \boldsymbol{U}_2^{\mathrm{plates}} \rangle$	Velocity field for parallel-plates	$\mathrm{m\,s^{-1}}$
$\langle Q_2^{\mathrm{plates}} \rangle$	Pressure field for parallel-plates	$\mathrm{kg\,m^{-1}\,s^{-2}}$
$\langle \boldsymbol{U}_2^{\mathrm{cor}} \rangle$	Velocity field for rectangular correction	$\mathrm{m\,s^{-1}}$
$\langle Q_2^{\mathrm{cor}} \rangle$	Pressure field for rectangular correction	$\mathrm{kg\,m^{-1}\,s^{-2}}$
l, m, n, q	Summation index	
$\circ_n^m$	$\circ$ for the n'th Fourier term and the m'th iteration	
b_n^m	Fourier expansion coefficients	
C_{1n}^m, C_{2n}^m	Form coefficients	
M	Number of iterations	
N	Number of Fourier components	
σ_{rms}	Root mean square deviation	
$\left\langle \boldsymbol{U}_2^{\Delta} \right\rangle$	Approximate envelope solution	$\mathrm{m\,s^{-1}}$
$g(x)$	Envelope function	
Δ	Envelope parameter	m
Δ_{min}	Value of Δ for optimal $\boldsymbol{U}_2^{\Delta}$	m
d_{mesh}	Maximum side length of numerical mesh elements	m

Chapter 1

Introduction

1.1 Lab-on-a-chip systems

The technology of lab-on-a-chip (LOC) systems aims at carrying out chemical and biological processes on a microchip. There are several advantages of downscaling the processes usually carried out in conventional macroscopic laboratories to the sub-millimeter scale; (i) smaller sample volume is needed, (ii) faster reaction rates for chemical and biological processes due to the large surface to volume ratio, (iii) potentially low cost by utilizing mass production, and (iv) development of portable analysis systems, bringing the analysis closer to the point of care. However, with downscaling new challenges arise. The large surface to volume ratio introduces new dynamics, requiring rethinking of the existing techniques for production and operation.

LOC systems often utilize fluidic channels for transport of samples and as reaction chambers. Microfluidics refers to the discipline of handling fluids on the sub-millimeter scale. At this scale the fluid flows behave much differently compared to macroscopic flows. Due to the large surface to volume ratio, viscous effects dominate inertial effects. The Reynolds number is typically of order unity or below, resulting in no turbulence, but a laminar flow following predictable streamlines. This predictability of the flow can be utilized to control the path of suspended samples, however, it also leads to new challenges concerning mixing, which in microfluidics is often induced by diffusion only.

A common task encountered in LOC systems utilizing microfluidics is control of suspended particles, such as biological cells or microbeads. Particle control includes moving, sorting, and trapping particles, and can be done using various techniques such as electrophoresis, dielectrophoresis or magnetophoresis. Good results have been achieved with these techniques, however, several issues limit their usability. For these techniques, the sample particles are often required to have specific electric or magnetic properties, which in many cases requires electric or magnetic labeling of the sample prior to the analysis. Furthermore, the electric and magnetic fields might perturb the physical state of the par-

ticles or the surrounding fluid, and thus in some cases influence the measured variables. For review papers and textbooks on microfluidics see [2–9].

1.2 Acoustofluidics

Another way of controlling suspended particles is by acoustic forces. Acoustofluidics refer to the use of ultrasound in microfluidic systems. An acoustic wave or a sound wave is commonly regarded as a wave carrying a perturbation in the local pressure. However, as the three thermodynamic variables; pressure, density, and temperature are related through the thermodynamic equation of state, the acoustic wave carry perturbations in all of these variables. As the dimensions of microfluidic channels are typically in the order of 1 mm and the speed of sound in water is 1497 m/s, ultrasound frequencies in the order of MHz is needed for the acoustic wavelength to be comparable to the microchannel dimensions.

In the field of acoustofluidics two effects are primarily considered; the acoustic radiation force, and the acoustic streaming. The acoustic radiation force acts on suspended particles and originates from scattering of the acoustic wave on the particle. Its magnitude and direction depend on the relative density and compressibility of the particle and the suspending fluid. The acoustic radiation force rely on momentum transfer from the acoustic wave to the suspended particle, resulting in a translational movement of the particle relative to the fluid. The acoustic streaming rely on momentum transfer from the acoustic wave to the fluid. This momentum transfer can occur either due to bulk attenuation of a traveling acoustic wave (known as Quartz wind) or by interaction between an acoustic wave and a solid boundary (known as boundary-driven acoustic streaming). The acoustic streaming indirectly acts on suspended particles through drag forces.

Both the acoustic radiation force and the acoustic streaming were described in 1831 by Faraday [10], while experiments carried out in 1874 by Kundt [11], known as Kundt's tube, acted as a source of inspiration for the following theoretical treatment. The theoretical treatment was initiated by Rayleigh [1] and King [12] for the acoustic streaming and the acoustic radiation force, respectively. Since their seminal work, there has been many contributions to the further development of the theory [13–26]. For review articles on acoustofluidics see [27–29].

1.3 Experimental motivation

The field of acoustofluidics has received a renewed interest following the turn of the millennium with application in microfluidic systems. Many applications utilizing acoustofluidics for functions, such as pumping, mixing, particle sorting and trapping, have been demonstrated [30–50]. Much of the development has been experimentally driven, focusing on applications, while less emphasis has been given to the theoretical understanding of the physics involved. For the acoustic streaming it is often seen that the experimental results are compared to the results of Rayleigh, even though the dimensions of the experiment is well beyond the limitations of Rayleigh's theory.

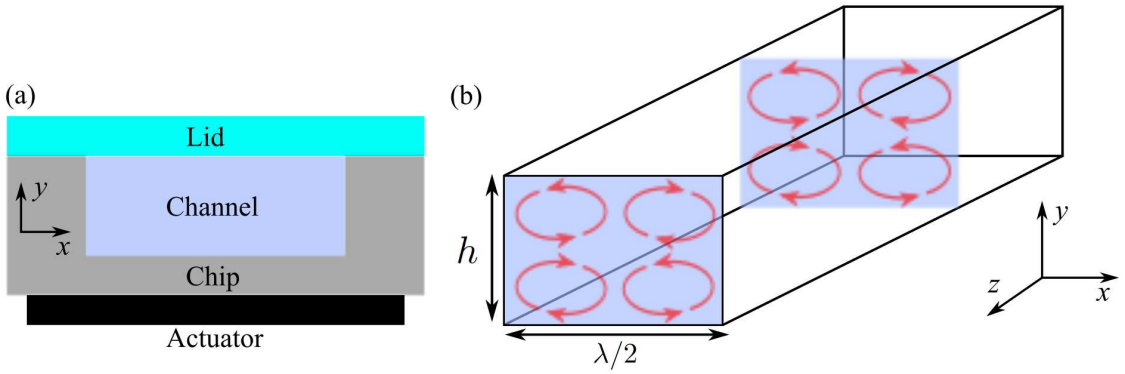

Figure 1.1: (a) Cross-sectional sketch of a typical microfluidic chip for acoustophoresis. A rectangular channel is etched into a chip, and a transparent lid is bonded on top to close the channel and allow for visual inspection. An acoustic actuator is attached to the chip. The chip and lid is often made of silicon and glass, respectively, while the actuator is a piezo ceramic, and the channel is filled with water [52]. (b) Sketch of the water filled channel. The steady rotational flow, created by the acoustic streaming, is in the vertical cross-sectional plane of the channel. This makes it difficult to measure experimentally, using conventional microscope techniques, as we only have visual access from the top through the glass lid.

On the other hand the acoustic streaming observed in experiments has been difficult to predict theoretically, as it is affected by acoustic losses in the experimental systems. Moreover, it is difficult to design an experiment in which a well-controlled and simple acoustic streaming flow can be measured quantitatively, allowing for comparison with theoretical models. However, the experimental group of Laurell at Lund University and the theoretical group of Bruus at the Technical University of Denmark have recently demonstrated a well-controlled setup for quantitative measurements of particle-velocity fields in an acoustically actuated microchannel [51, 52]. A stable resonance in a microfluidic channel can be obtained with this setup, primarily due to the introduced temperature control and minimization of acoustic losses.

As the acoustic streaming is present in the vertical cross-sectional plane of the channel, it is difficult to measure with conventional microscopy, see sketch in Figure 1.1. However, very recently the collaboration has been extended to include the group of Kähler at Bundeswehr University Munich, who has demonstrated the use of astigmatism particle tracking velocimetry in microfluidics [53, 54]. This technique allows for quantitative measurements of the acoustic streaming velocity field, and thus calls for theoretical models for the acoustic streaming in rectangular microfluidic channels.

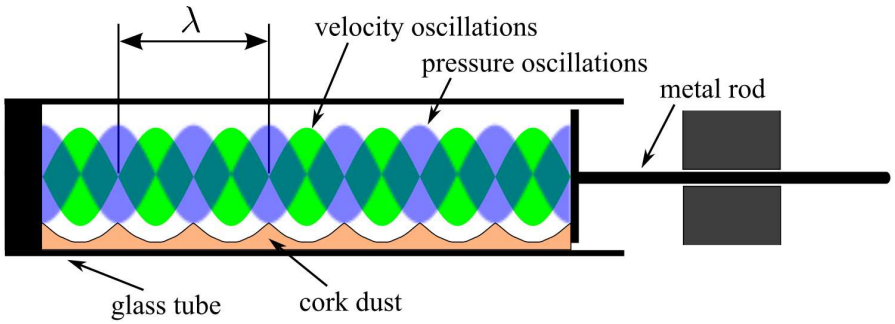

Figure 1.2: Sketch of Kundt's tube experiment [11]. A standing sound wave is generated inside a glass tube by a vibrating metal rod. Small dust particles inside the air-filled tube accumulate at the pressure anti-nodes due to the acoustic streaming. The figure is a modified version of that found at [55].

1.4 Theoretical motivation

In this thesis only boundary-driven acoustic streaming is considered and the phrase *acoustic streaming* will be used to refer to this type only. In Kundt's experiment the speed of sound is measured, using a resonator tube and a source vibrating at a single frequency, see the sketch in Figure 1.2. At resonance small dust particles in the air-filled tube accumulate at the pressure anti-nodes, and the wavelength of the sound wave can be measured as twice the distance between the piles of particles.

This phenomenon arises due to the acoustic streaming, a steady rotational motion of the fluid in the vicinity of the boundaries, and was explained theoretically by Rayleigh [1]. Rayleigh considered a standing acoustic wave between two parallel plates, as sketched in Figure 1.3 (a), where the amplitude of the oscillating velocity is indicated by the size of the bidirectional arrows.

Close to the boundary the amplitude of the oscillating fluid velocity have to decay to zero because of the shear viscosity of the fluid and the molecular forces between the solid boundary and the fluid molecules, as shown in Figure 1.3 (b). This requirement for zero velocity at the wall is denoted the no-slip boundary condition. The decay of the oscillating velocity happens on a length scale of δ, the thickness of the viscous acoustic boundary layer, from now on referred to as the boundary layer thickness. The magnitude of the boundary layer thickness is shown in Table 1.1 for different fluids and sound frequencies.

Rayleigh showed that the decay of the oscillating velocity gives rise to a steady rotational flow between the plates, as sketched in Figure 1.3 (c). Rayleigh's derivation relies on the assumption that the thickness of the boundary layer is much smaller than the height h of the parallel-plates channel, which in turn is much smaller than the acoustic

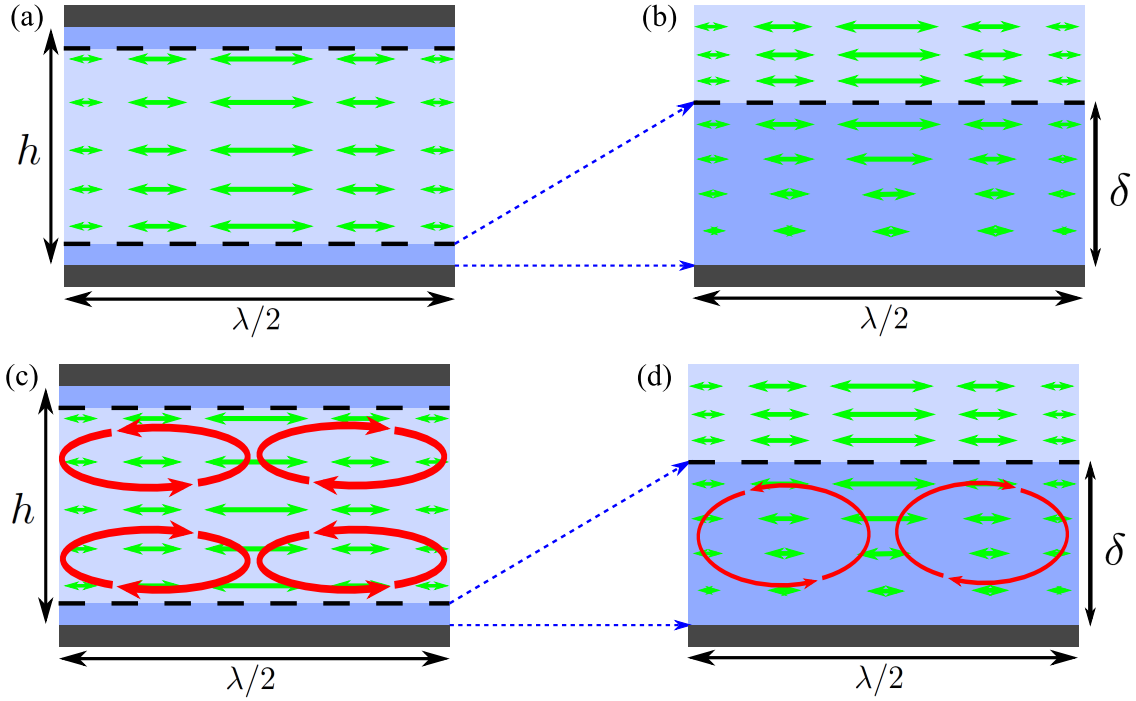

Figure 1.3: (a) The horizontal oscillating velocity (green arrows) of a standing acoustic wave between two parallel plates. Far from the wall the amplitude of the velocity oscillations is invariant in the vertical direction. (b) The oscillating velocity inside the acoustic boundary layer close to the wall. The velocity decays to zero at the wall due to the no-slip boundary condition. The decay happens on a length scale of δ, denoted the boundary layer thickness. (c) The steady velocity (red arrows) between two parallel plates generated by the standing acoustic wave. Rayleigh [1] described how non-linear interactions of the oscillating velocity field (green arrows) lead to a steady rotational flow, referred to as the outer streaming rolls (or bulk streaming rolls). The magnitude of the steady velocity is much smaller than the amplitude of the oscillating velocity. (d) The steady velocity (red arrows) inside the acoustic boundary layer. Schlichting [13] described the existence of the inner streaming rolls (or boundary streaming rolls).

Medium	δ at kHz	δ at MHz
Water	18 µm	0.6 µm
Air	76 µm	2.4 µm
Glycerol	542 µm	17 µm

Table 1.1: Boundary layer thickness δ for different fluids at audio frequencies (kHz) and ultrasound frequencies (MHz). The boundary layer thickness scales as the square root of the viscosity divided by the density and frequency. Even though air is much lighter than water, it is also less viscous, and consequently δ is of the same order of magnitude. Glycerol is a very viscous organic liquid with viscosity and density similar to honey, resulting in a large boundary layer thickness.

wavelength λ, $\delta \ll h \ll \lambda$. Based on Prandtl's boundary-layer theory [56], Schlichting later described the existence of streaming rolls inside the boundary layer [13], as sketched in Figure 1.3 (d). In 2003, Hamilton [25] presented an analytical solution to the acoustic streaming in a parallel-plates channel, where the thickness of the boundary layer is comparable to the channel height but much smaller than the acoustic wavelength, $\delta \sim h \ll \lambda$. This work was motivated by the development of thermoacoustic engine stacks (acoustic heat pumps used in refrigerators), in which the channel dimensions are comparable to the boundary layer thickness.

For microfluidic acoustophoresis, i.e. microfluidic devices utilizing acoustic forces to control particles, the channel height is most often comparable to the wavelength, and the solution given by Rayleigh is no longer adequate, see the diagram in Figure 1.4. Surprisingly, not much emphasis seems to be given to this, possibly due to a lack of awareness of the limitations of Rayleigh's result. There is thus a need for development of the theory in the case of $\delta \ll h \sim \lambda$ and disseminate the knowledge to the acoustofluidic research community.

Moreover, Rayleigh's result on acoustic streaming is for the case of an infinite parallel-plates channel. The height to width ratio of microfluidic channels used for acoustophoresis is often close to unity, making the infinite parallel-plates assumption an unsuitable choice, as it neglects the influence of the no-slip condition on the side walls. This presents a need for the derivation of the acoustic streaming in rectangular channels, where the no-slip conditions on all four wall are considered. Furthermore, the literature study for this thesis showed an inconsistency in the common approach to the problem of acoustic streaming,

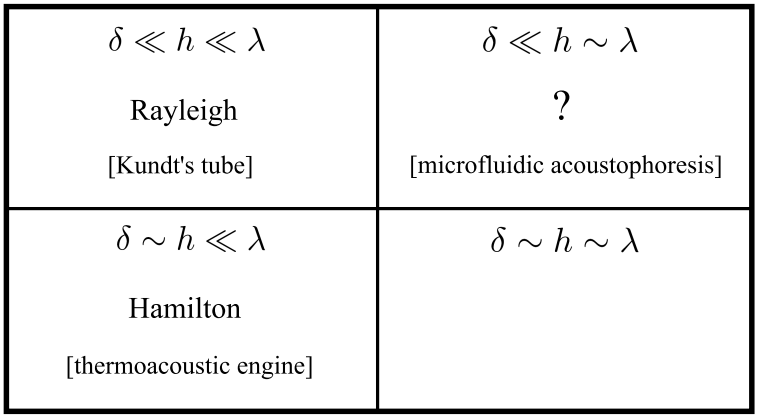

Figure 1.4: Overview of the different cases of acoustic streaming between two parallel plates, governed by the three length scales; the boundary layer thickness δ, the distance between the plates h, and the acoustic wavelength λ. The development of the theory in the case of $\delta \ll h \ll \lambda$, by Rayleigh [1] among others, was motivated by Kundt's experiments [11]. Recent developments of the theory in the case of $\delta \sim h \ll \lambda$, by Hamilton [25] among others, was motivated by the use of thermoacoustic engines. As indicated in the top right square, a need exist for development of the theory in the case of $\delta \ll h \sim \lambda$, as this is relevant for microfluidic devices utilizing acoustic forces.

such as in Landau [57]. This concerns the assumption of incompressibility of the fluid close to the walls and will be discussed in greater details in Section 2.4. The treatment of this inconsistency has led to a novel formulation of the acoustic streaming problem, described in Section 2.5.

1.5 Foundation and objective

This thesis is based on the foundation of the work done by several students in the group of Bruus on the theoretical aspects of acoustofluidics. Among these are Thomas Glasdam Jensen [58], Peder Skafte-Pedersen [59], Lasse Mejling Andersen, Anders Nysteen, and Mikkel Settnes [60], and finally Rune Barnkob [61]. From previous work, it is clear that a better theoretical understanding of the acoustic streaming is needed in order to extent the theory. A thorough analysis and reformulation of the basic physics of the acoustic streaming is the first objective of this thesis. This analysis is then used to extent the theory to include the case of the high parallel-plates channel. The overall objective of this thesis is to make the analytical model resemble the real microfluidic devices, and consequently we approach the problem of acoustic streaming in a rectangular channel. These results form the basis for comparison between analytical models and experimental results, and we discuss the experimental methods needed to measure acoustic streaming. In order to verify the analytical models, a numerical investigation is performed and we point out several challenges in the problem of solving acoustic streaming numerically.

1.6 Outline

Chapter 2: Basic acoustofluidics theory

In this chapter, the framework for the thesis is created by introducing the governing equations of acoustofluidics along with the second-order perturbation scheme. We point out an inconsistency in the common approach to acoustic streaming in terms of the assumed incompressibility close to the boundaries, and we propose a novel approach to the problem of acoustic streaming, in which the fluid is considered compressible everywhere.

Chapter 3: Acoustic streaming at a planar wall

We employ the novel approach to the case of acoustic streaming at a single wall. This approach leads to an acoustic streaming in agreement with the results presented by Rayleigh [1]. The accuracy of the derivation is limited by the approximate solution to the first-order problem, and we point out which measures should be taken in order to improve the analytical result.

Chapter 4: Acoustic streaming in microfluidic channels

In this chapter, the analytical boundary solution from Chapter 3 is utilized to derive the bulk acoustic streaming flow in microfluidic channels. We derive the acoustic streaming in a thin parallel-plates channel, before extending the derivation to the case of the high

parallel-plates channel. Finally, we derive the acoustic streaming in a rectangular channel, using an iterative Fourier expansion approach.

Chapter 5: Numerical simulations

We outline the challenges involved with solving the problem of acoustic streaming numerically, and point out different approaches to meet these challenges. A numerical scheme using the commercial software COMSOL MULTIPHYSICS is set up and characterized, and preliminary results are discussed.

Chapter 6: Experimental outlook

This chapter acts an experimental outlook. We describe how measurements of acoustic streaming can be achieved using a cylindrical lens, allowing for quantitative comparison between experimental, analytical, and numerical results.

Chapter 7: Conclusion

Chapter 2

Basic acoustofluidic theory

In this chapter we present the governing equations, upon which the work in this thesis is based. The theory of acoustics deal with coupled oscillations in pressure, density and temperature. However, in this thesis only isothermal systems are considered. Moreover, we treat only acoustic waves in fluids. The approach to the basic theory presented here is inspired by Landau [57], Bruus [5], Barnkob [61], Skafte-Pedersen [59] and the tutorial series on acoustofluidics currently being published in *Lab on a Chip* [29], mainly [62] and [63].

After introducing the basic theory, we describe the common theoretical approach to the problem of acoustic streaming, as presented in [57,63]. We point out an inconsistency in this approach, in terms of the assumed incompressibility of the fluid in the vicinity of the boundaries, and we propose a novel approach to the problem of acoustic streaming.

2.1 Governing equations

The three governing equations, describing acoustics in microfluidic systems, are the thermodynamic equation of state expressing pressure in terms density, the kinematic continuity equation for the density, and the dynamic Navier–Stokes equation for the velocity field of a compressible Newtonian fluid. In the Eulerian field description, and considering only isothermal systems, they become

$$\rho\partial_t \boldsymbol{v} = -\boldsymbol{\nabla} p - \rho\left(\boldsymbol{v}\cdot\boldsymbol{\nabla}\right)\boldsymbol{v} + \eta\nabla^2\boldsymbol{v} + \beta\eta\boldsymbol{\nabla}\left(\boldsymbol{\nabla}\cdot\boldsymbol{v}\right), \tag{2.1a}$$

$$\partial_t \rho = -\boldsymbol{\nabla}\cdot(\rho\boldsymbol{v}), \tag{2.1b}$$

$$p = p\left(\rho\right), \tag{2.1c}$$

where $p = p\left(\mathbf{r},t\right)$ is the pressure field, $\rho = \rho\left(\mathbf{r},t\right)$ is the density field, $\boldsymbol{v} = \boldsymbol{v}\left(\boldsymbol{r},t\right)$ is the velocity field, η is the dynamic viscosity, and β is the viscosity ratio. For simple

liquids $\beta = 1/3$. Considering a fluid domain Ω the velocity field should fulfill the no-slip boundary condition at rigid walls

$$\boldsymbol{v} = \mathbf{0}, \quad \text{for } \boldsymbol{r} \in \partial\Omega. \tag{2.2}$$

To gain insight into the solutions of the set Eq. (2.1) of coupled non-linear partial differential equations, in problems with no exact analytical solution, we apply perturbation theory to obtain approximate solutions.

2.1.1 Perturbation scheme

We consider a homogeneous fluid initially in a quiescent state $\{p_0, \rho_0, \boldsymbol{v}_0\}$ of thermal equilibrium with $\boldsymbol{v}_0 = \mathbf{0}$. Considering small perturbations to this state we can expand the three fields representing velocity, pressure, and density,

$$\boldsymbol{v} = \mathbf{0} + \boldsymbol{v}_1 + \boldsymbol{v}_2 + \dots , \tag{2.3a}$$
$$p = p_0 + p_1 + p_2 + \dots , \tag{2.3b}$$
$$\rho = \rho_0 + \rho_1 + \rho_2 + \dots , \tag{2.3c}$$

where the subscripts denote the first and second-order perturbations with the perturbation parameter being implicit.

Performing an isentropic second-order Taylor expansion of the thermodynamic equation of state (2.1c) around $p(\rho_0) = p_0$ yields

$$p(\rho) = p_0 + c^2\rho_1 + c^2\rho_2 + \frac{1}{2}\left(\partial_\rho c^2\right)\rho_1^2, \tag{2.4}$$

where the constant c^2 has been introduced as the isentropic derivative of the pressure with respect to density

$$c^2 = \left(\frac{\partial p}{\partial \rho}\right)_S\Big|_{\rho=\rho_0}. \tag{2.5}$$

It will later be shown that c is indeed the isentropic speed of sound in the fluid.

Zeroth-order equations

Inserting the perturbations Eqs. (2.3) into the governing equations (2.1) the zeroth-order equations become

$$\boldsymbol{\nabla} p_0 = \mathbf{0}, \tag{2.6a}$$
$$\partial_t \rho_0 = 0, \tag{2.6b}$$
$$p_0 = p(\rho_0), \tag{2.6c}$$

which have the solution p_0 and ρ_0 being constant in space and time.

First order equations

Considering only first-order terms the first-order governing equations become

$$\rho_0 \partial_t \boldsymbol{v}_1 = -c^2 \boldsymbol{\nabla} \rho_1 + \eta \nabla^2 \boldsymbol{v}_1 + \beta \eta \boldsymbol{\nabla} (\boldsymbol{\nabla} \cdot \boldsymbol{v}_1), \tag{2.7a}$$

$$\partial_t \rho_1 = -\rho_0 \boldsymbol{\nabla} \cdot \boldsymbol{v}_1, \tag{2.7b}$$

$$p_1 = c^2 \rho_1, \tag{2.7c}$$

where the first-order pressure in Eq. (2.7a) has been expressed in terms of the first-order density and the constant zeroth-order fields have been pulled outside the differential operators.

The first-order equation (2.7a) is a linearization of the full Navier–Stokes equation. To determine the implicit perturbation parameter we consider a harmonic velocity field with angular frequency ω and wave vector k such that $\omega = kc$. Comparing the two terms $\rho \partial_t \boldsymbol{v} \sim \rho \omega v$ and $\rho (\boldsymbol{v} \cdot \boldsymbol{\nabla}) \boldsymbol{v} \sim \rho k v^2$ of Eq. (2.1a), it can be concluded that linearization is permissible when $kv^2 \ll \omega v$ or equivalently $v \ll c$. The implicit perturbation parameter is thus the ratio v/c, the characteristic flow velocity v divided by the speed of sound c.

Second-order equations

Similarly, the second-order equations become

$$\rho_0 \partial_t \boldsymbol{v}_2 = -\boldsymbol{\nabla} p_2 - \rho_1 \partial_t \boldsymbol{v}_1 - \rho_0 (\boldsymbol{v}_1 \cdot \boldsymbol{\nabla}) \boldsymbol{v}_1 + \eta \nabla^2 \boldsymbol{v}_2 + \beta \eta \boldsymbol{\nabla} (\boldsymbol{\nabla} \cdot \boldsymbol{v}_2), \tag{2.8a}$$

$$\partial_t \rho_2 = -\rho_0 \boldsymbol{\nabla} \cdot \boldsymbol{v}_2 - \boldsymbol{\nabla} \cdot (\rho_1 \mathbf{v}_1), \tag{2.8b}$$

$$p_2 = c^2 \rho_2 + \frac{1}{2} \left(\partial_\rho c^2 \right) \rho_1^2. \tag{2.8c}$$

The terms consisting of products of first-order terms are referred to as source terms, as the non-linear interactions of the first-order fields acts as sources for weaker second-order fields.

2.1.2 Inviscid fluid

For an ideal inviscid fluid there is no viscous loss, $\eta = 0$, and instead of the viscous Navier–Stokes equation (2.1a) the flow is governed by the inviscid Euler equation

$$\rho \partial_t \boldsymbol{v} = -\boldsymbol{\nabla} p - \rho (\boldsymbol{v} \cdot \boldsymbol{\nabla}) \boldsymbol{v}. \tag{2.9}$$

The inviscid boundary condition at rigid walls only constrain the perpendicular velocity component,

$$\boldsymbol{n} \cdot \boldsymbol{v} = 0, \quad \text{for } \boldsymbol{r} \in \partial\Omega, \tag{2.10}$$

and an inviscid fluid can thus have a velocity component parallel to the wall, referred to as a slip velocity.

2.1.3 Incompressible fluid

For an incompressible fluid the density is constant and the continuity equation (2.1b) becomes

$$\boldsymbol{\nabla} \cdot \boldsymbol{v} \quad = \quad 0. \tag{2.11}$$

Inserting this in Eq. (2.1a) the Navier–Stokes equation for an incompressible fluid becomes

$$\rho \partial_t \boldsymbol{v} \quad = \quad -\boldsymbol{\nabla} p - \rho \left(\boldsymbol{v} \cdot \boldsymbol{\nabla} \right) \boldsymbol{v} + \eta \nabla^2 \boldsymbol{v}. \tag{2.12}$$

In order to determine, when a fluid can be considered incompressible, we consider the inviscid Euler equation (2.9). In steady state it becomes

$$\rho \left(\boldsymbol{v} \cdot \boldsymbol{\nabla} \right) \boldsymbol{v} \quad = \quad -\boldsymbol{\nabla} p. \tag{2.13}$$

Dimensional analysis of this equation using the thermodynamic equation of state (2.7c) yields

$$\frac{v^2}{c^2} \quad \sim \quad \frac{\rho'}{\rho}, \tag{2.14}$$

where the general expansion $\rho = \rho_0 + \rho'$ has been introduced, with ρ' being the spatially varying part of ρ. For the fluid to be considered as incompressible, i.e. $\frac{\rho'}{\rho} \ll 1$, we must demand

$$\frac{v^2}{c^2} \quad \ll \quad 1. \tag{2.15}$$

This is the first condition for incompressibility, implying that the fluid velocity must be much smaller than the speed of sound in the medium. This is the only condition for incompressibility when considering steady state flow.

For time-dependent flow a second condition for incompressibility arises, which should be fulfilled as well as the condition Eq. (2.15). Considering the first-order Euler equation we have

$$\rho_0 \partial_t \boldsymbol{v}_1 \quad = \quad -\boldsymbol{\nabla} p_1. \tag{2.16}$$

Dimensional analysis using the thermodynamic equation of state (2.7c) yields

$$\frac{l v \rho_0}{\tau c^2} \quad \sim \quad \rho' \tag{2.17}$$

where l and τ are characteristic length and time scales over which the first-order perturbation fields change. Turning to the first-order continuity equation (2.7b) we have

$$\partial_t \rho_1 \quad = \quad -\rho_0 \boldsymbol{\nabla} \cdot \boldsymbol{v}_1 = -\rho_0 \sum_{i=1}^{3} \partial_i v_i, \tag{2.18}$$

where we have written the divergence as a sum to indicate that it contains several terms. For the fluid to be considered incompressible we must demand that the left hand term is much smaller than the magnitude of one of the terms in the sum

$$\partial_t \rho_1 \quad \ll \quad \rho_0 \partial_i v_i, \tag{2.19}$$

which by dimensional analysis leads to

$$\frac{1}{\tau}\rho' \quad \ll \quad \rho_0 \frac{v}{l}. \tag{2.20}$$

Inserting Eq. (2.17) in Eq. (2.20) we find

$$\frac{l^2}{c^2} \quad \ll \quad \tau^2. \tag{2.21}$$

This is the second condition for incompressibility which should be fulfilled by time-dependent flow along with the first condition Eq. (2.15). l/c is the time it takes for acoustic perturbations to transverse the characteristic length l of the system. If this time scale is much smaller than the time scale τ of the changes of the perturbations, then acoustic interactions can be considered to be instantaneous. The fluid can thus be considered incompressible, if the perturbation amplitudes are small as well. If the system is actuated harmonically the characteristic time scale is $\tau = 1/f$ and the condition becomes

$$l^2 \quad \ll \quad \lambda^2. \tag{2.22}$$

The second condition in the case of time-harmonic fields thus becomes that the characteristic length scale should be much shorter than the acoustic wavelength. In problems with several or none characteristic length scales, care should be taken, when determining whether the fluid can be considered incompressible or not.

2.2 First-order acoustofluidics

To describe the linear effects in acoustofluidics we consider the first-order perturbation equations (2.7). In the first-order theory the variations in pressure and density are in phase and proportional in magnitude according to Eq.(2.7c). In the following derivations we state the equation in terms of ρ_1, keeping in mind that the same equations are valid for p_1.

We will in general assume that all first-order perturbation fields vary harmonically in time, and to ease the theoretical formulation we use the complex phase notation for the time dependence,

$$\boldsymbol{v}_1(\boldsymbol{r},t) = \boldsymbol{v}_1(\boldsymbol{r})\,\mathrm{e}^{-\mathrm{i}\omega t}, \tag{2.23a}$$
$$\rho_1(\boldsymbol{r},t) = \rho_1(\boldsymbol{r})\,\mathrm{e}^{-\mathrm{i}\omega t}, \tag{2.23b}$$
$$p_1(\boldsymbol{r},t) = c^2\rho_1(\boldsymbol{r})\,\mathrm{e}^{-\mathrm{i}\omega t}, \tag{2.23c}$$

where $\omega = 2\pi f$ is the angular frequency and f is the frequency of the acoustic field. The physical quantities of the fields can be obtained by taking the real part of the complex fields. In this complex phase notation the partial time derivative ∂_t can be replaced by the factor $-\mathrm{i}\omega$.

2.2.1 Helmholtz equation

Firstly, we obtain a single equation for ρ_1 by taking the time derivative of the first-order continuity equation (2.7b) and substituting the velocity terms by use of Eqs. (2.7a) and (2.7b)

$$\begin{aligned} \partial_t^2 \rho_1 &= c^2 \nabla^2 \rho_1 - (1+\beta)\,\eta \nabla^2 \left(\boldsymbol{\nabla} \cdot \boldsymbol{v}_1\right) \\ &= c^2 \left[1 + \frac{(1+\beta)\,\eta}{\rho_0 c^2} \partial_t\right] \nabla^2 \rho_1 \end{aligned} \tag{2.24}$$

Substitution the time derivative in Eq. (2.24) we obtain the Helmholtz equation for the density

$$\nabla^2 \rho_1 = -\tilde{k}^2 \rho_1, \tag{2.25a}$$

$$\tilde{k} = k\,(1 + \mathrm{i}\gamma)\,, \tag{2.25b}$$

$$k = \frac{\omega}{c}, \tag{2.25c}$$

$$\gamma = \frac{(1+\beta)\,\eta\omega}{2\rho_0 c^2}, \tag{2.25d}$$

where we have introduced the complex wave number $\tilde{k}$, the real wave number k, and the viscous damping factor γ. The viscous damping factor γ has been assumed to be much smaller than unity. Possible solutions to the Helmholtz equation (2.25a) are damped plane waves

$$\rho_1\left(\boldsymbol{r}, t\right) = \rho_A \mathrm{e}^{\mathrm{i}\left(\tilde{\boldsymbol{k}}\cdot\boldsymbol{r} - \omega t\right)} = \rho_A \mathrm{e}^{\mathrm{i}(\boldsymbol{k}\cdot\boldsymbol{r} - \omega t)}\, \mathrm{e}^{-\gamma \boldsymbol{k}\cdot\boldsymbol{r}}, \tag{2.26}$$

where ρ_A is the initial amplitude of the wave and γ is indeed seen to be the damping factor of the wave. In the analysis presented in this thesis the following characteristic dimensionless number ϵ plays an important role

$$\epsilon = \frac{\eta\omega}{\rho_0 c^2} = \frac{1}{2} k^2 \delta^2, \tag{2.27}$$

where we have introduced the thickness of the viscous acoustic boundary layer δ, which in terms of the kinematic viscosity $\nu = \eta/\rho_0$ is given by

$$\delta = \sqrt{\frac{2\nu}{\omega}}. \tag{2.28}$$

For MHz acoustics in water the viscous penetration depth is $\delta \approx 0.5\ \mu$m and $\epsilon \approx 3 \times 10^{-6}$. Throughout the thesis we will refer to the two orders of magnitude ϵ and $k\delta \approx \sqrt{\epsilon}$. The viscous damping factor γ can also be rewritten in terms of ϵ

$$\gamma = \frac{(1+\beta)}{2}\epsilon \tag{2.29}$$

In the regime of $\epsilon \ll 1$ the first-order Navier–Stokes equation (2.7a) and the continuity equation (2.7b) reduce to

$$\boldsymbol{v}_1 \approx -\mathrm{i}\frac{c}{\rho_0 k}\boldsymbol{\nabla}\rho_1 + \mathrm{i}\frac{\epsilon}{k^2}\nabla^2\boldsymbol{v}_1 + \mathcal{O}(\epsilon), \tag{2.30}$$

$$\boldsymbol{\nabla}\cdot\boldsymbol{v}_1 = \mathrm{i}\frac{\omega}{\rho_0}\rho_1, \tag{2.31}$$

where in Eq. (2.30) the following approximation using Eq. (2.31) has been made

$$-c^2\boldsymbol{\nabla}\rho_1 + \beta\eta\boldsymbol{\nabla}(\boldsymbol{\nabla}\cdot\boldsymbol{v}_1) = -(1-\mathrm{i}\beta\epsilon)c^2\boldsymbol{\nabla}\rho_1 = -c^2\boldsymbol{\nabla}\rho_1 + \mathcal{O}(\epsilon). \tag{2.32}$$

The Laplace term in Eq. (2.30) cannot in general be neglected as $\nabla^2\boldsymbol{v}_1$ becomes of order $\frac{1}{\delta^2}v$ near rigid walls. This is due to the no-slip boundary condition making the velocity field decay towards the wall on a length scale of δ, the length scale of the viscous boundary layer. By inserting Eq. (2.30) in Eq. (2.31) the inviscid Helmholtz equation is obtained

$$-\frac{\omega^2}{c^2}\rho_1 = (1-\mathrm{i}\epsilon)\nabla^2\rho_1 = \nabla^2\rho_1 + \mathcal{O}(\epsilon). \tag{2.33}$$

This shows that the first-order density field to zeroth order in ϵ is independent of viscous effects, which is an important point when deriving the acoustic streaming velocity field.

2.2.2 Inviscid acoustofluidics

Far from rigid obstacles the bulk velocity field $\boldsymbol{U}_1$ varies on a length scales of λ and the viscous term in Eq. (2.30) becomes $\frac{\epsilon}{k^2}\nabla^2\boldsymbol{U}_1 \sim \frac{\epsilon}{k^2}k^2\boldsymbol{U}_1 \ll \boldsymbol{U}_1$. For the bulk field the viscosity can thus be neglected altogether and the bulk field is to zeroth order in ϵ characterized by the equations

$$\boldsymbol{U}_1 = -\mathrm{i}\frac{c}{\rho_0 k}\boldsymbol{\nabla}\rho_1, \tag{2.34a}$$

$$\boldsymbol{\nabla}\cdot\boldsymbol{U}_1 = \mathrm{i}\frac{\omega}{\rho_0}\rho_1, \tag{2.34b}$$

$$\nabla^2\rho_1 = -k^2\rho_1. \tag{2.34c}$$

From Eq. (2.34a) we note that an inviscid velocity field is a gradient field and hence rotation free. The bulk velocity field $\boldsymbol{U}_1$ does not take into account viscous effects at the rigid walls and thus does not fulfill the no-slip boundary condition at the walls

$$\boldsymbol{U}_1(\boldsymbol{r}) \neq \boldsymbol{0}, \quad \text{for } \boldsymbol{r} \in \partial\Omega. \tag{2.35}$$

The full solution to the viscous first-order acoustic wave problem in a domain with rigid walls thus requires the addition of another velocity field component.

From the inviscid Helmholtz equation (2.33) we can obtain the inviscid wave equation for the acoustic wave by back-substituting $-\mathrm{i}\omega$ with ∂_t,

$$\nabla^2 \rho_1 = \frac{1}{c^2} \partial_t^2 \rho_1. \tag{2.36}$$

The solutions to this classical wave equation are in 1D given by d'Alembert's formula and have the form

$$\rho_1 (x,t) = \rho_1 (x \pm ct). \tag{2.37}$$

During the time t the perturbation in density $\rho_1 (x)$ is displaced by $\mp ct$, proving that c is indeed the propagation speed of the acoustic wave in the inviscid limit and to first order in the perturbation $\rho_1 \ll \rho_0$.

2.3 Second-order acoustofluidics

In the linear acoustic theory all fields are proportional to a harmonic time dependence and the resulting effects will thus average to zero over a full oscillation period. To achieve a time-averaged effect we have to go to second-order acoustics. In the second-order equations, source terms enter, containing products of first-order fields. This result in terms oscillating in time at twice the first-order frequency and terms constant in time. This can be recognized from the cosine relation, $\cos^2 (\omega t) = \frac{1}{2} \cos (2\omega t) + \frac{1}{2}$. As the time-varying second-order effects are negligible in magnitude compared to the first-order effects we will only concern ourselves with the time-averaged second-order fields.

Taking the time average of the second-order Navier–Stokes equation (2.8a) we get

$$\eta \nabla^2 \langle \boldsymbol{v}_2 \rangle + \beta\eta \boldsymbol{\nabla} (\boldsymbol{\nabla} \cdot \langle \boldsymbol{v}_2 \rangle) - \boldsymbol{\nabla} \langle p_2 \rangle = \langle \rho_1 \partial_t \boldsymbol{v}_1 \rangle + \rho_0 \langle (\boldsymbol{v}_1 \cdot \boldsymbol{\nabla}) \boldsymbol{v}_1 \rangle, \tag{2.38}$$

where $\langle \partial_t \boldsymbol{v}_2 \rangle = \boldsymbol{0}$, since $\boldsymbol{v}_2$ can only have a constant term and an oscillatory term.

The time-averaged second-order continuity equation (2.8b) becomes

$$\rho_0 \boldsymbol{\nabla} \cdot \langle \boldsymbol{v}_2 \rangle = -\boldsymbol{\nabla} \cdot \langle \rho_1 \boldsymbol{v}_1 \rangle. \tag{2.39}$$

In the inviscid case, i.e. far from rigid walls, Eq. (2.34a) indicates that $\boldsymbol{U}_1$ and ρ_1 are exactly $\pi/2$ out of phase and thus $\langle \rho_1 \boldsymbol{U}_1 \rangle = \boldsymbol{0}$. The second-order velocity field is thereby incompressible in the bulk

$$\boldsymbol{\nabla} \cdot \left\langle \boldsymbol{v}_2^{\mathrm{bulk}} \right\rangle = 0. \tag{2.40}$$

The second-order velocity leads to acoustic streaming, a steady rotational flow, which is a result of absorption of momentum by the fluid from the acoustic wave. The second-order pressure give rise to the acoustic radiation force, a gradient force on suspended particles due to scattering of the acoustic wave on the particles.

2.4 Acoustic streaming using boundary-layer theory

In this section we discuss the usual approach to analytical analysis of acoustic streaming. In order to determine the oscillatory first-order velocity field in the vicinity of rigid walls for $\epsilon \ll 1$, we need to solve Eq. (2.30). The primary challenge, solving this equation, is how to deal with the term proportional to $\epsilon\nabla^2\boldsymbol{v}_1$, where the small perturbation factor ϵ is multiplied by the highest-order (second-order) derivative. As discussed in Section 2.2.2, this term is negligible far from rigid walls where $\nabla^2 \sim k^2$. Close to the walls, the velocity decay to fulfill the no-slip boundary condition, resulting in $\nabla^2 \sim 1/\delta^2$, and thus the term $\epsilon\nabla^2\boldsymbol{v}_1$ cannot be neglected. This type of problem is referred to as singular perturbation theory, where "singular" refers to the crucial difference between ϵ being zero (inviscid fluid) or finite but very small. The usual way of dealing with this problem is to apply boundary-layer theory, originally introduced by Prandtl [56]. In boundary-layer theory the fluid domain is divided into a bulk region and a boundary layer region as sketched in Figure 2.1. The first-order velocity field is first solved in the bulk region and then subsequently in the boundary layer region, demanding the boundary field to match the bulk field when moving far away from the wall. In order to solve the velocity field inside the boundary layer a rescaling of the length scales and the velocities is performed [63].

As the thickness of the viscous boundary layer is usually much smaller than the acoustic wavelength, $\delta \ll \lambda$, the velocity field inside the boundary layer is assumed to be incompressible, with a reference to the second condition of incompressibility Eq. (2.22), see e.g. Landau [57]. However, strictly speaking this not correct. The fluid inside the boundary layer is not compressed in the direction perpendicular to the wall, in which it varies on a length scale of δ. However, in the direction parallel to the wall, the fluid inside the boundary layer is compressed in exactly the same way as the fluid outside the boundary layer. Only when considering the viscous boundary layer around particles of size $a \ll \lambda$ can the incompressibility inside the boundary layer be rightfully assumed, as in this case the length scales δ and a govern the boundary layer in all spatial directions

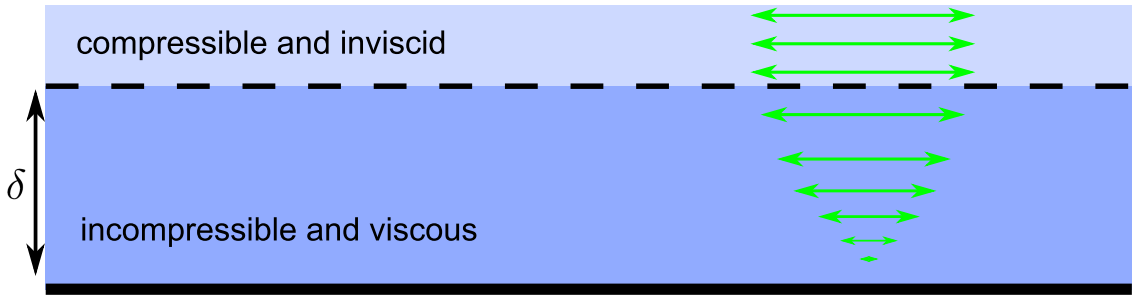

Figure 2.1: Sketch of the division of the fluid domain into a bulk region and a boundary layer region applied in boundary-layer theory. The first-order velocity field is considered to be compressible and inviscid in the bulk region, and incompressible and viscous in the boundary layer region. The arrows indicate how the amplitude of the oscillating first-order velocity field decay towards the wall.

and the condition Eq. (2.22) is fulfilled.

In order to rectify this misleading assumption we develop a novel approach to the problem of acoustic streaming. In this approach each field is decomposed into constituent parts, and it is clarified which part of the velocity fields that should be considered incompressible.

2.5 A novel approach to acoustic streaming

In this section we present a novel approach to the acoustic wave problem near rigid walls. In this approach all parts of the acoustic fields are defined in the entire domain of interest. There is no division of the domain into a bulk and a boundary region, though the phrase *boundary layer* is used to denote the vicinity of the wall. The main objective is to show that the fluid is not incompressible inside the boundary layer. Instead, the inviscid bulk field is present in the whole domain, and an incompressible velocity field, significant only close to the wall, is added to the bulk field. The starting point of the global approach is a known resonant first-order density field ρ_1, which can be calculated from basic resonance theory, thoroughly treated by Barnkob [61]. The goal is to determine the time-averaged second-order velocity and pressure fields. Both the first- and second-order fields are decomposed into constituent parts in order to clarify the structure of the fields.

2.5.1 Decomposition of the first-order velocity field

As shown in Section 2.2.1 the first-order density field ρ_1 does not depend on viscous boundary effects to order ϵ. From the inviscid theory Eq. (2.34) we can determine an inviscid bulk velocity field $\boldsymbol{U}_1$, which also has the structure of the resonance. As discussed in relation to Eq. (2.35) the inviscid bulk field $\boldsymbol{U}_1$ does not in general fulfill the no-slip boundary condition at rigid walls and to account for this we decompose the total first-order velocity field $\boldsymbol{v}_1$ into

$$\boldsymbol{v}_1 = \boldsymbol{U}_1 + \boldsymbol{u}_1, \tag{2.41}$$

where the magnitude of $\boldsymbol{u}_1$ is significant only close to the boundaries and equal to $-\boldsymbol{U}_1$ on the boundaries. Motivated by Eq. (2.33), which states that the first-order density is independent of the viscous boundary effects, we seek a solution to $\boldsymbol{u}_1$ which is incompressible and introduces no pressure gradients, and is thus governed by $\rho_0 \partial_t \boldsymbol{u}_1 = \eta \nabla^2 \boldsymbol{u}_1$. Substituting ∂_t by $-\mathrm{i}\omega$ and introducing $\kappa \equiv (1-\mathrm{i})/\delta$, the complete set of governing equations and boundary conditions for $\boldsymbol{u}_1$ become

$$\nabla^2 \boldsymbol{u}_1 = \kappa^2 \boldsymbol{u}_1, \tag{2.42a}$$

$$\boldsymbol{\nabla} \cdot \boldsymbol{u}_1 = 0, \tag{2.42b}$$

$$\boldsymbol{u}_1(\boldsymbol{r}) = -\boldsymbol{U}_1(\boldsymbol{r}), \quad \text{for } \boldsymbol{r} \in \partial\Omega, \tag{2.42c}$$

$$\boldsymbol{u}_1(\boldsymbol{r}) \to \boldsymbol{0}, \quad \text{for } r_\perp \to \infty, \tag{2.42d}$$

where $r_\perp$ is the perpendicular distance from the wall. These equations determine $\boldsymbol{u}_1$ and complete the treatment of the first-order pressure and density fields. In Section 3.1 the

first-order fields are calculated in the case of a single planar wall. We will now go on to the time-averaged second-order fields.

2.5.2 Decomposition of the second-order fields

In this section the time-averaged second-order velocity field $\langle \boldsymbol{v}_2 \rangle$ and time-averaged second-order pressure field $\langle p_2 \rangle$ are decomposed into constituent parts in order to solve and clarify the structure of the fields. The governing equations are the time-averaged second-order Navier–Stokes equation (2.38) and continuity equation (2.39).

Decomposition of the second-order velocity

We start out by considering the time-averaged Navier–Stokes equation (2.38). The right-hand side includes only source terms determined by the known first-order fields, whereas the left-hand side includes the two unknown second-order fields $\langle \boldsymbol{v}_2 \rangle$ and $\langle p_2 \rangle$. In the interest of determining $\langle \boldsymbol{v}_2 \rangle$, we eliminate $\langle p_2 \rangle$ from the equation by taking the rotation, utilizing that a gradient field is rotation free,

$$\nu \nabla^2 \boldsymbol{\nabla} \times \langle \boldsymbol{v}_2 \rangle \;=\; \boldsymbol{\nabla} \times \left[\langle (\boldsymbol{v}_1 \cdot \boldsymbol{\nabla}) \, \boldsymbol{v}_1 \rangle + \frac{1}{\rho_0} \langle \rho_1 \partial_t \boldsymbol{v}_1 \rangle \right]. \tag{2.43}$$

This equation governs $\langle \boldsymbol{v}_2 \rangle$ along with the continuity equation (2.39) and the no-slip boundary condition,

$$\langle \boldsymbol{v}_2 \rangle \;=\; 0, \quad \text{for } \boldsymbol{r} \in \partial\Omega. \tag{2.44}$$

To solve Eq. (2.43) we perform a threefold decomposition of $\langle \boldsymbol{v}_2 \rangle$

$$\langle \boldsymbol{v}_2 \rangle \;=\; \langle \boldsymbol{U}_2 \rangle + \langle \boldsymbol{W}_2 \rangle + \langle \boldsymbol{u}_2 \rangle \,, \tag{2.45}$$

where $\langle \boldsymbol{U}_2 \rangle$ is the complete homogeneous solution to Eq. (2.43), $\langle \boldsymbol{W}_2 \rangle$ is a particular solution to the inhomogeneous equation (2.43) in the bulk, and $\langle \boldsymbol{W}_2 \rangle + \langle \boldsymbol{u}_2 \rangle$ is a particular solution everywhere. $\langle \boldsymbol{U}_2 \rangle$ and$\langle \boldsymbol{W}_2 \rangle$ are thus significant everywhere, similar to $\boldsymbol{U}_1$, whereas $\langle \boldsymbol{u}_2 \rangle$ is significant only close to the boundaries, similar to $\boldsymbol{u}_1$. The governing momentum equations and boundary condition for $\langle \boldsymbol{U}_2 \rangle$, $\langle \boldsymbol{W}_2 \rangle$ and $\langle \boldsymbol{u}_2 \rangle$ become

$$\nabla^2 \boldsymbol{\nabla} \times \langle \boldsymbol{U}_2 \rangle \;=\; \boldsymbol{0}, \tag{2.46a}$$

$$\nu \nabla^2 \boldsymbol{\nabla} \times \langle \boldsymbol{W}_2 \rangle \;=\; \boldsymbol{\nabla} \times \left[\langle (\boldsymbol{U}_1 \cdot \boldsymbol{\nabla}) \, \boldsymbol{U}_1 \rangle + \frac{1}{\rho_0} \langle \rho_1 \partial_t \boldsymbol{U}_1 \rangle \right] = \boldsymbol{0}, \tag{2.46b}$$

$$\nu \nabla^2 \boldsymbol{\nabla} \times \langle \boldsymbol{u}_2 \rangle \;=\; \boldsymbol{\nabla} \times \left[\langle (\boldsymbol{v}_1 \cdot \boldsymbol{\nabla}) \, \boldsymbol{u}_1 \rangle + \langle (\boldsymbol{u}_1 \cdot \boldsymbol{\nabla}) \, \boldsymbol{U}_1 \rangle + \frac{1}{\rho_0} \langle \rho_1 \partial_t \boldsymbol{u}_1 \rangle \right] \tag{2.46c}$$

$$\langle \boldsymbol{U}_2 \rangle + \langle \boldsymbol{W}_2 \rangle + \langle \boldsymbol{u}_2 \rangle \;=\; \boldsymbol{0}, \quad \text{for } \boldsymbol{r} \in \partial\Omega. \tag{2.46d}$$

However, as indicated in Eq. (2.46b) the rotation of the bulk source terms is by definition zero, and consequently $\langle \boldsymbol{W}_2 \rangle = \boldsymbol{0}$. This is because $\boldsymbol{U}_1$ is the gradient of a potential proportional to ρ_1, as given by Eq. (2.34a). There are no degrees of freedom in Eq. (2.46c) as the homogenous solution is covered by Eq. (2.46a). The boundary condition

Eq. (2.46d) is thus implemented through determining $\langle \boldsymbol{u}_2 \rangle$ with no constraints on the boundary and then constraining $\langle \boldsymbol{U}_2 \rangle$ by

$$\langle \boldsymbol{U}_2 \rangle = -\langle \boldsymbol{u}_2 \rangle, \quad \text{for } \boldsymbol{r} \in \partial\Omega. \tag{2.47}$$

According to the decomposition of $\langle \boldsymbol{v}_2 \rangle$ the continuity equation (2.39) become

$$\rho_0 \boldsymbol{\nabla} \cdot \langle \boldsymbol{U}_2 \rangle = -\boldsymbol{\nabla} \cdot \langle \rho_1 \boldsymbol{U}_1 \rangle = 0, \tag{2.48a}$$
$$\rho_0 \boldsymbol{\nabla} \cdot \langle \boldsymbol{u}_2 \rangle = -\boldsymbol{\nabla} \cdot \langle \rho_1 \boldsymbol{u}_1 \rangle = -\langle \boldsymbol{\nabla} \rho_1 \cdot \boldsymbol{u}_1 \rangle, \tag{2.48b}$$

where we have used Eq. (2.40) to conclude that the bulk field $\langle \boldsymbol{U}_2 \rangle$ is incompressible.

Decomposition of the second-order pressure

As we previously considered the rotation of the Navier–Stokes equation in order to determine the velocity, the divergence of Eq. (2.38) is now considered in order to obtain a Poisson equation for the pressure

$$\nabla^2 \langle p_2 \rangle = -\boldsymbol{\nabla} \cdot \langle \rho_1 \partial_t \boldsymbol{v}_1 \rangle - \rho_0 \boldsymbol{\nabla} \cdot \langle (\boldsymbol{v}_1 \cdot \boldsymbol{\nabla}) \boldsymbol{v}_1 \rangle - (1+\beta) \nu \nabla^2 (\langle \boldsymbol{\nabla} \rho_1 \cdot \boldsymbol{u}_1 \rangle), \tag{2.49}$$

where Eq. (2.48) has been used to express $\boldsymbol{\nabla} \cdot \langle \boldsymbol{v}_2 \rangle$ in terms of the first-order fields. In order to solve Eq. (2.49) we perform a threefold decomposition of $\langle p_2 \rangle$

$$\langle p_2 \rangle = \langle Q_2 \rangle + \langle X_2 \rangle + \langle \chi_2 \rangle, \tag{2.50}$$

where $\langle Q_2 \rangle$ solves the homogeneous Laplace equation, $\langle X_2 \rangle$ is a particular solution in the bulk, and $\langle X_2 \rangle + \langle \chi_2 \rangle$ is a particular solution everywhere. $\langle Q_2 \rangle$ and $\langle X_2 \rangle$ are thus significant everywhere, similar to $\boldsymbol{U}_1$, whereas $\langle \chi_2 \rangle$ is significant only close to the boundaries, similar to $\boldsymbol{u}_1$. The governing equations for $\langle Q_2 \rangle$, $\langle X_2 \rangle$ and $\langle \chi_2 \rangle$ thus become

$$\nabla^2 \langle Q_2 \rangle = 0, \tag{2.51a}$$
$$\nabla^2 \langle X_2 \rangle = -\boldsymbol{\nabla} \cdot \langle \rho_1 \partial_t \boldsymbol{U}_1 \rangle - \rho_0 \boldsymbol{\nabla} \cdot \langle (\boldsymbol{U}_1 \cdot \boldsymbol{\nabla}) \boldsymbol{U}_1 \rangle, \tag{2.51b}$$
$$\nabla^2 \langle \chi_2 \rangle = -\boldsymbol{\nabla} \cdot \langle \rho_1 \partial_t \boldsymbol{u}_1 \rangle - \rho_0 \boldsymbol{\nabla} \cdot \langle (\boldsymbol{v}_1 \cdot \boldsymbol{\nabla}) \boldsymbol{u}_1 \rangle - \rho_0 \boldsymbol{\nabla} \cdot \langle (\boldsymbol{u}_1 \cdot \boldsymbol{\nabla}) \boldsymbol{U}_1 \rangle - (1+\beta) \nu \nabla^2 (\langle \boldsymbol{\nabla} \rho_1 \cdot \boldsymbol{u}_1 \rangle). \tag{2.51c}$$

We have now performed a general decomposition of the time-averaged second-order velocity field and pressure field, along with their governing equations and boundary conditions. The implementation of this novel approach in Chapter 3 shows why the introduction of the boundary-layer theory is necessary as a similar measure is applied to bound the incompressible boundary field $\boldsymbol{u}_1$. For the planar wall the novel approach leads to the same result for the acoustic streaming in the bulk, as obtained with the boundary layer approach. This is because the errors due to the incorrect assumption of incompressibility in the boundary-layer theory are neglected due to their low magnitude. The physical form of the acoustic field and the details of the flow in the vicinity of the wall is better described by our novel approach, and this insight is important when considering acoustic streaming in more complex cavities.

2.6 Concluding remarks

We have presented the basic acoustofluidic theory upon which the work in this thesis is based. Moreover, we have pointed out an inconsistency in the common approach to the problem of acoustic streaming, in terms of the assumption of incompressibility of the fluid close to the boundaries. We have proposed a novel approach to the problem of acoustic streaming, in which the fluid is considered compressible everywhere. In the following chapter, we will apply this approach to problem of a standing acoustic wave in the vicinity of a rigid wall.

Chapter 3

Acoustic streaming at a planar wall

In this chapter an analytical solution to the acoustic wave problem in the vicinity of a rigid wall is derived, using the novel approach described in Section 2.5. Considering a single planer wall in the (x, z)-plane positioned at $y = 0$, the acoustic wave problem is treated in the half space $y > 0$. It is shown that the first-order fields are overdetermined and a constraint similar to Prandtl's boundary-layer theory is applied to the incompressible first-order boundary field $\boldsymbol{u}_1$, in order to keep it bounded at the wall.

After dealing with the first-order fields in Section 3.1, the second-order boundary velocity field $\langle \boldsymbol{u}_2 \rangle$, pressure field $\langle p_2 \rangle$, and bulk velocity field $\langle \boldsymbol{U}_2 \rangle$ are dealt with in Sections 3.2, 3.3, and 3.4, respectively. In Section 3.5 the results for the second-order fields are visualized and discussed.

In Section 3.6.1 we make a comment on how the analytical derivation should be improved in the future work.

3.1 First-order fields

Far from the rigid wall $y \gg \delta$ the acoustic wave is to zeroth order in ϵ governed by the set of equations (2.34) and we will concern ourselves with the simple standing wave solution

$$\boldsymbol{U}_1 = u_0 \cos(kx)\, \mathrm{e}^{-\mathrm{i}\omega t} \boldsymbol{e}_x, \tag{3.1a}$$

$$\rho_1 = \mathrm{i}\rho_0 \frac{u_0}{c} \sin(kx)\, \mathrm{e}^{-\mathrm{i}\omega t}. \tag{3.1b}$$

Considering the boundary field $\boldsymbol{u}_1$ we are not able to find an exact analytical solution to the set of equations (2.42). To obtain an approximate solution the x-component of Eq. (2.42a) is first solved to zeroth order in ϵ with the boundary conditions Eq. (2.42c). Thereafter u_{1y} is determined from the incompressibility condition Eq. (2.42b) and the

boundary condition $u_{1y}|_{y=0} = 0$ yielding

$$u_{1x} = -u_0 \cos(kx)\, \mathrm{e}^{-\kappa y} \mathrm{e}^{-\mathrm{i}\omega t}, \tag{3.2a}$$

$$u_{1y} = -u_0 \sin(kx)\, \frac{k\delta}{1-\mathrm{i}} \left(1 - \mathrm{e}^{-y/\delta} \mathrm{e}^{\mathrm{i}y/\delta}\right) \mathrm{e}^{-\mathrm{i}\omega t}, \tag{3.2b}$$

where in the last equation the expression for κ has been substituted in order to illustrate the magnitude and form of the expression. It is noted that the solution for $\boldsymbol{u}_1$ Eq. (3.4) fulfills the continuity equation (2.42b) and the boundary condition (2.42c) exact whereas the momentum equation (2.42a) is not fulfilled for the y-component. However, the expressions for u_{1y} and ρ_1 fulfill the general first-order Navier–Stokes equation (2.7a) to zeroth order in ϵ.

The solution Eq. (3.2) is mainly confined within the viscous boundary layer, however, a small y-component spreads into the bulk

$$\boldsymbol{u}_1^{\mathrm{bulk}} = -u_0 \sin(kx)\, \frac{k\delta}{1-\mathrm{i}} \mathrm{e}^{-\mathrm{i}\omega t} \boldsymbol{e}_y. \tag{3.3}$$

Even though the magnitude of this bulk component is small, $\left|\boldsymbol{u}_1^{\mathrm{bulk}}\right| = k\delta\, |\boldsymbol{U}_1| \ll |\boldsymbol{U}_1|$, it has critical influence on the second-order bulk field $\langle \boldsymbol{W}_2 \rangle$ as it results in non-zero source terms in Eq. (2.46b). As a consequence we have to manually limit the extend of $\boldsymbol{u}_1$ through the following expression

$$u_{1x} = -u_0 \cos(kx)\, \mathrm{e}^{-\kappa y} \mathrm{e}^{-\mathrm{i}\omega t}, \qquad \text{for } 0 \le y \le 7\delta, \tag{3.4a}$$

$$u_{1y} = -u_0 \sin(kx)\, \frac{k\delta}{1-\mathrm{i}} \left(1 - \mathrm{e}^{-y/\delta} \mathrm{e}^{\mathrm{i}y/\delta}\right) \mathrm{e}^{-\mathrm{i}\omega t}, \qquad \text{for } 0 \le y \le 7\delta, \tag{3.4b}$$

$$\boldsymbol{u}_1 = \boldsymbol{0}, \qquad \text{for } y > 7\delta. \tag{3.4c}$$

The interface is put at $y = 7\delta$ at which point the x- and y-components are of similar magnitude. Further elaboration on this value is found in Section 3.2.1. This construction of $\boldsymbol{u}_1$ is very similar to the construction of the boundary layer in Prandtl's theory. It illustrates why this artificial bounding of the boundary field is necessary, as we cannot find a solution fulfilling all of the equations (2.42) to order ϵ. At the interface $y = 7\delta$ there is a mismatch in the first-order velocity of order $k\delta$. This error is the Achilles' heel of the analytical derivation and sets the order to which this derivation is accurate. To improve the derivation we would have to find a better solution to $\boldsymbol{u}_1$.

The total first-order velocity field $\boldsymbol{v}_1$ is shown in Figure 3.1 for half a spatial period in the x-direction, $-\pi/2 \le kx \le \pi/2$, at $\omega t = 0$. It is important to note that the axes are not constrained. If the axes were in dimensional units and constrained the width of the graph would be 10^3 times the height, according to $k\delta \sim 10^{-3}$. The variations in the x-direction are thus very slow compared to the variations in the y-direction, and due to the incompressibility of $\boldsymbol{u}_1$ the magnitude of u_{1y} is consequently equally small compared to u_{1x}. Figure 3.2 further shows how u_{1x} is confined to the boundary and makes the total velocity field $\boldsymbol{v}_1$ fulfill the no-slip boundary condition.

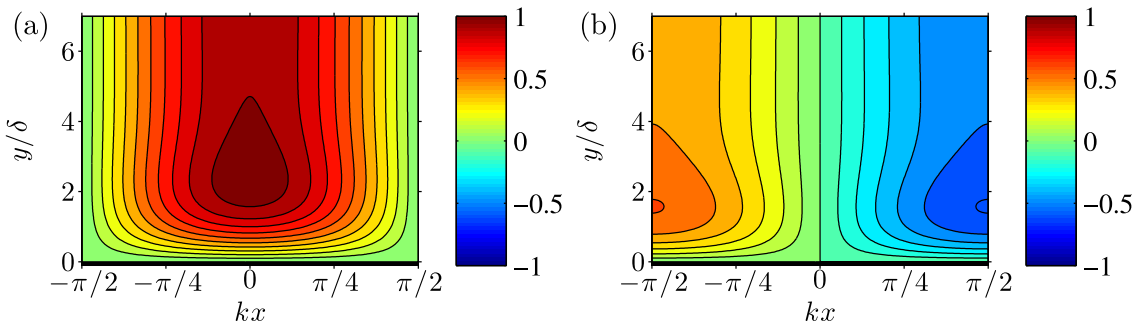

Figure 3.1: Color plot of the first-order velocity field close to a planar wall at $y/\delta = 0$, in the case of a standing bulk wave, $U_{1x} = u_0 \cos(kx)\, \mathrm{e}^{-\mathrm{i}\omega t}$. The velocity field is shown for $\omega t = 0$. (a) x-component of the first-order velocity field v_{1x} normalized to the amplitude of the bulk wave u_0. Far from the wall v_{1x} varies harmonically in the x-direction and is independent of y. Close to the wall the velocity decay to zero, fulfilling the no-slip boundary condition. (b) y-component of the first-order velocity field v_{1y} normalized to $u_0 k\delta$. The velocity field is artificially bounded at $y = 7\delta$ since the expression for u_{1y} does not decay when moving away from the wall.

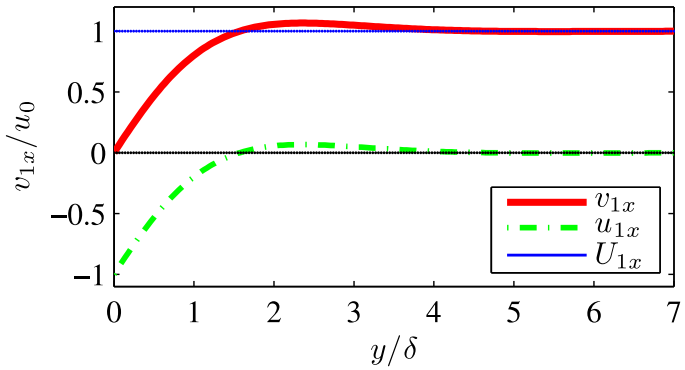

Figure 3.2: The x-component of the decomposition of the first-order velocity field, $\boldsymbol{v}_1 = \boldsymbol{U}_1 + \boldsymbol{u}_1$, on the vertical line at $kx = 0$ and at time $\omega t = 0$. We see how u_{1x} is confined to the boundary and how v_{1x} increases slightly before decaying to zero when closing in on the boundary.

We have now solved the first-order acoustic wave problem for a single wall and a standing wave through determining the first-order velocity field $\boldsymbol{v}_1$ and the first-order density field ρ_1. These first-order fields are then used in the source terms for the time-averaged second-order equations which will be treated in Section 3.2.

3.1.1 Comparison to Rayleigh

At this point we check the result against Rayleigh [1] in order to assess the differences. In equation R.(76) of [1] the first-order velocity fields are stated, in the case a compressible flow between two parallel plates

$$v_{1x}^{\mathrm{R}} = \cos(kx)\left[-1+\mathrm{e}^{-\kappa y}\right]\mathrm{e}^{-\mathrm{i}\omega t}, \tag{3.5a}$$

$$v_{1y}^{\mathrm{R}} = \frac{k}{\kappa}\sin(kx)\left[1-\frac{2y}{h}-\mathrm{e}^{-\kappa y}\right]\mathrm{e}^{-\mathrm{i}\omega t}, \tag{3.5b}$$

where the variables has been changed to our notation and h is the distance between the plates. The main differences between our solution, Eq. (3.4), and Rayleigh's solution, Eq. (3.5), is that v_{1y}^{R} include a term linear in y, and that v_{1y}^{R} is not confined to the boundary layer. The terms of v_{1y}^{R} spreading into the bulk are neglected in the calculations of the second-order field in [1], hence the critical effects pointed out by us in relation to Eq. (3.3) is not assessed in [1]. The linear term of v_{1y}^{R} also contributes to the divergence of the first-order field, which becomes

$$\partial_x v_{1x}^{\mathrm{R}} + \partial_y v_{1y}^{\mathrm{R}} = k\sin(kx)\left(1-\frac{2}{\kappa h}\right). \tag{3.6}$$

This illustrates that according to the velocity field given in [1] the first-order density can only be determined to order $\mathcal{O}(\delta/h)$, using the inviscid Helmholtz equation(2.33), and not to order $\mathcal{O}(\epsilon)$ as we propose.

We now move on to the second-order velocity field, where we will see that despite the differences in the first-order fields, we obtain the same acoustic streaming boundary condition for the bulk flow as Rayleigh [1].

3.2 Second-order velocity inside the boundary layer

In this section we will determine the second-order velocity field close to the boundary, $\langle \boldsymbol{u}_2 \rangle$. We start out by considering a physical interpretation of the Rayleigh streaming problem as a diffusion of vorticity generated in the boundary layer. Afterward, a general decomposition of $\langle \boldsymbol{u}_2 \rangle$ into a gradient field and a rotation is performed, and a particular solution to Eq. (2.46c) is found.

3.2.1 Diffusion of vorticity

In this section we consider the vorticity of the second-order velocity field, $\langle \zeta_2 \rangle \equiv \left[\boldsymbol{\nabla} \times \langle \boldsymbol{v}_2 \rangle\right]_z$. Only the z-component of Eq. (2.43) is non-zero, as we are considering fields in the (x,y)-plane, and this can be considered as a time-averaged diffusion equation for the vorticity

$$\nu \nabla^2 \langle \zeta_2 \rangle = \langle S(x,y) \rangle, \tag{3.7}$$

where the kinematic viscosity ν is the diffusion constant for momentum and hence vorticity. $\langle S(x,y) \rangle$ is the time-averaged local vorticity source density generated by the first-order fields, and from Eq. (2.43) given by

$$\langle S(x,y) \rangle = \left\{ \boldsymbol{\nabla} \times \left[\langle (\boldsymbol{v}_1 \cdot \boldsymbol{\nabla}) \boldsymbol{v}_1 \rangle + \frac{1}{\rho_0} \langle \rho_1 \partial_t \boldsymbol{v}_1 \rangle \right] \right\}_z. \tag{3.8}$$

As noted in Section 2.5 the bulk source terms are rotation free. The rotation of the fluid is generated inside the thin viscous boundary layer and momentum diffuse into the bulk due to large velocity gradients perpendicular to the wall. The boundary source terms on the right hand side of Eq. (3.8) can be divided into two groups depending on their magnitude

$$\left\{\boldsymbol{\nabla}\times\left[\langle(\boldsymbol{U}_1\cdot\boldsymbol{\nabla})\,\boldsymbol{u}_1\rangle+\langle(\boldsymbol{u}_1\cdot\boldsymbol{\nabla})\,\boldsymbol{U}_1\rangle+\langle(\boldsymbol{u}_1\cdot\boldsymbol{\nabla})\,\boldsymbol{u}_1\rangle+\frac{1}{\rho_0}\langle\rho_1\partial_t\boldsymbol{u}_1\rangle\right]\right\}_z =$$
$$-\partial_y\left[\langle(\boldsymbol{U}_1\cdot\boldsymbol{\nabla})\,u_{1x}\rangle+\langle(\boldsymbol{u}_1\cdot\boldsymbol{\nabla})\,U_{1x}\rangle+\langle(\boldsymbol{u}_1\cdot\boldsymbol{\nabla})\,u_{1x}\rangle+\frac{1}{\rho_0}\langle\rho_1\partial_t u_{1x}\rangle\right]+O\left(\epsilon\mathrm{e}^{y/\delta}\right), \quad (3.9)$$

where $\mathcal{O}\left(\epsilon\mathrm{e}^{y/\delta}\right)$ indicates the relative order of magnitude of the neglected terms. Generally we have $\partial_x u_{1y}\sim\epsilon\partial_y u_{1x}$ and thus we have neglected the terms proportional to $\partial_x u_{1y}$. However, since u_{1y} contains a term which does not decay with $\mathrm{e}^{-y/\delta}$ the relative order of the neglected terms is really $\mathcal{O}\left(\epsilon\mathrm{e}^{y/\delta}\right)$ since all remaining terms decay with $\mathrm{e}^{-y/\delta}$. This is the reason we artificially bound $\boldsymbol{u}_1$ at $y=7\delta$. At this value the neglected terms are still of relative order $\mathcal{O}\left(10^{-3}\right)$. Consequently $\langle\boldsymbol{u}_2\rangle$ will also be artificially bounded at $y=7\delta$.

Using the first-order fields, Eq. (3.1), we see that

$$\frac{1}{\rho_0}\langle\rho_1\partial_t u_{1x}\rangle = -\frac{1}{\rho_0}\langle(\partial_t\rho_1)\,u_{1x}\rangle=\langle(\partial_x U_{1x})\,u_{1x}\rangle=\langle(\boldsymbol{u}_1\cdot\boldsymbol{\nabla})\,U_{1x}\rangle. \quad (3.10)$$

In this rewrite it is noted that moving the imaginary constant $\partial_t\to-\mathrm{i}\omega$ from one component to the other, inside the time-average operator, introduces a sign change. Equation (3.8) reduces to

$$\langle S(x,y)\rangle = -\partial_y\left[3\langle(\boldsymbol{U}_1\cdot\boldsymbol{\nabla})\,u_{1x}\rangle+\langle(\boldsymbol{u}_1\cdot\boldsymbol{\nabla})\,u_{1x}\rangle\right], \quad (3.11)$$

where we have exploited that the real operator ∂_x can be interchanged between U_{1x} and u_{1x}, i.e. $\langle U_{1x}\partial_x u_{1x}\rangle=\langle u_{1x}\partial_x U_{1x}\rangle$. Expanding the right hand terms, the final expression for the source field become

$$\langle S(x,y)\rangle = -3\langle U_{1x}\partial_y\partial_x u_{1x}\rangle-\langle u_{1x}\partial_y\partial_x u_{1x}\rangle-\left\langle u_{1y}\partial_y^2 u_{1x}\right\rangle, \quad (3.12)$$

where the following terms have canceled out

$$\langle(\partial_y u_{1x})\,\partial_x u_{1x}\rangle+\langle(\partial_y u_{1y})\,\partial_y u_{1x}\rangle = \langle(\partial_x u_{1x}+\partial_y u_{1y})\,\partial_y u_{1x}\rangle=0, \quad (3.13)$$

since $\boldsymbol{u}_1$ is incompressible.

We could now determine a particular solution for the time-averaged vorticity $\langle\zeta_2\rangle$ using Eqs. (3.7) and (3.12), and the first-order fields. So far no case specific action has been performed. In order to obtain not only the vorticity field but the velocity field, a further decomposition of $\langle\boldsymbol{u}_2\rangle$ is made.

3.2.2 Decomposition of the boundary velocity field

We perform a general vector decomposition of $\langle \boldsymbol{u}_2 \rangle$ into a gradient field and a rotation

$$\langle \boldsymbol{u}_2 \rangle = \boldsymbol{\nabla} \langle \phi_2 (x,y) \rangle + \boldsymbol{\nabla} \times \Big[\langle \psi_2 (x,y) \rangle \, \boldsymbol{e}_z \Big], \tag{3.14}$$

where each component become

$$\langle u_{2x} \rangle = \partial_x \langle \phi_2 \rangle + \partial_y \langle \psi_2 \rangle , \tag{3.15}$$
$$\langle u_{2y} \rangle = \partial_y \langle \phi_2 \rangle - \partial_x \langle \psi_2 \rangle . \tag{3.16}$$

The divergence and the rotation of the decomposition (3.14) leads to

$$\nabla^2 \langle \phi_2 \rangle = \boldsymbol{\nabla} \cdot \langle \boldsymbol{u}_2 \rangle , \tag{3.17}$$
$$\nabla^2 \langle \psi_2 \rangle = - \left[\boldsymbol{\nabla} \times \langle \boldsymbol{u}_2 \rangle \right]_z , \tag{3.18}$$

using the vector identity

$$\boldsymbol{\nabla} \times \boldsymbol{\nabla} \times \langle \psi_2 \rangle \boldsymbol{e}_z = \boldsymbol{\nabla} \left(\boldsymbol{\nabla} \cdot \langle \psi_2 \rangle \boldsymbol{e}_z \right) - \nabla^2 \langle \psi_2 \rangle \boldsymbol{e}_z = - \nabla^2 \langle \psi_2 \rangle \boldsymbol{e}_z . \tag{3.19}$$

Returning to the diffusion equation for the vorticity Eq. (3.7) and using Eq. (3.18) to substitute $\langle \zeta_2 \rangle = -\nabla^2 \langle \psi_2 \rangle$ we obtain a biharmonic equation for the stream function $\langle \psi_2 \rangle$

$$\nu \nabla^2 \nabla^2 \langle \psi_2 \rangle = - \langle S (x,y) \rangle . \tag{3.20}$$

To find a solution to this equation we need to approximate the biharmonic operator. Due to the variation of the first-order source fields in $S(x,y)$, which will be inherited by ψ_2, we approximate the biharmonic operator, considering the order of magnitudes $\partial_x \langle \psi_2 \rangle \sim k \langle \psi_2 \rangle$ and $\partial_y \langle \psi_2 \rangle \sim \frac{1}{\delta} \langle \psi_2 \rangle$

$$\nabla^2 \nabla^2 \langle \psi_2 \rangle = \left(\partial_x^4 + \partial_y^4 + 2 \partial_x^2 \partial_y^2 \right) \langle \psi_2 \rangle = \partial_y^4 \langle \psi_2 \rangle + \mathcal{O}(\epsilon) , \tag{3.21}$$

and the equation for $\langle \psi_2 \rangle$ becomes

$$\nu \partial_y^4 \langle \psi_2 \rangle = - \langle S (x,y) \rangle . \tag{3.22}$$

We now leave $\langle \psi_2 \rangle$ for a moment and turn to the velocity potential $\langle \phi_2 \rangle$ given by Eq. (3.17). In order to determine the right hand side of Eq. (3.17) we rewrite the continuity equation (2.48b) using $\boldsymbol{\nabla} \rho_1 = \mathrm{i} \rho_0 \frac{k}{c} \boldsymbol{U}_1$ from Eq. (2.34a)

$$\boldsymbol{\nabla} \cdot \langle \boldsymbol{u}_2 \rangle = - \frac{k}{c} \langle (\mathrm{i} U_{1x}) \, u_{1x} \rangle . \tag{3.23}$$

From Eqs. (3.23) and (3.17), with the Laplacian approximated by

$$\nabla^2 \langle \phi_2 \rangle = \partial_y^2 \langle \phi_2 \rangle + \mathcal{O}(\epsilon) , \tag{3.24}$$

we find

$$\partial_y^2 \langle \phi_2 \rangle = -\frac{k}{c} \langle (\mathrm{i} U_{1x})\, u_{1x} \rangle . \tag{3.25}$$

Comparing Eq. (3.22) for $\langle \psi_2 \rangle$ and Eq. (3.25) for $\langle \phi_2 \rangle$, rewriting Eq. (3.22) using $\nu = \delta^2 \omega / 2$, we see that $\langle \psi_2 \rangle \sim \delta \frac{u_0^2}{c}$ and $\langle \phi_2 \rangle \sim k\delta^2 \frac{u_0^2}{c} \sim k\delta \langle \psi_2 \rangle$ and the decomposition of $\langle u_{2x} \rangle$ Eq. (3.15) thus becomes

$$\langle u_{2x} \rangle = \partial_x \langle \phi_2 \rangle + \partial_y \langle \psi_2 \rangle = \partial_y \langle \psi_2 \rangle + \mathcal{O}(\epsilon) . \tag{3.26}$$

This is an important result. It means that to zeroth order in ϵ, $\langle u_{2x} \rangle$ can be calculated solely from $\langle \psi_2 \rangle$. In other words $\langle u_{2x} \rangle$ is calculated as if $\langle \boldsymbol{u}_2 \rangle$ was incompressible. Considering the y-component, $\langle u_{2y} \rangle = \partial_y \langle \phi_2 \rangle - \partial_x \langle \psi_2 \rangle$, it is clear that both terms are of order of magnitude $\delta k \langle u_{2x} \rangle$, and consequently they should both be taken into account.

A differential equation for $\langle u_{2x} \rangle$ can now be obtained from Eqs. (3.22) and (3.26)

$$\nu \partial_y^3 \langle u_{2x} \rangle = -\langle S(x,y) \rangle . \tag{3.27}$$

In order to determine $\langle u_{2x} \rangle$, the expressions Eqs. (3.1a) and (3.4) for the first-order fields are inserted in Eq. (3.12) for $\langle S(x,y) \rangle$, and following the calculation shown in Appendix A the source density become

$$\begin{aligned} \langle S(x,y) \rangle = {} & \frac{1}{2} u_0^2 k \frac{1}{\delta} \sin(2kx)\, e^{-y/\delta} \left[2\cos(y/\delta) + \sin(y/\delta) - \mathrm{e}^{-y/\delta} \right] \\ & + \mathcal{O}(k\delta) , \quad \text{for } 0 < \mathrm{y} < 7\delta. \end{aligned} \tag{3.28}$$

It should be implicitly understood that $\langle S(x,y) \rangle$ is otherwise zero. Here we have explicitly stated the relative order of the error on $\langle S(x,y) \rangle$. Integrating Eq. (3.27) three times with the source density given by Eq. (3.28) and rewriting $\nu = \delta^2 \omega / 2$ we get

$$\begin{aligned} \langle u_{2x} \rangle = {} & -\frac{3}{8} \frac{u_0^2}{c} \sin(2kx)\, e^{-y/\delta} \left[\frac{2}{3} \cos(y/\delta) + 2\sin(y/\delta) + \frac{1}{3} e^{-y/\delta} \right] \\ & + \mathcal{O}(k\delta) , \quad \text{for } 0 < \mathrm{y} < 7\delta, \end{aligned} \tag{3.29a}$$

We are seeking a particular solution $\langle \boldsymbol{u}_2 \rangle$ and thus no integration constants are included here, since the homogeneous solution is covered by $\langle \boldsymbol{U}_2 \rangle$.

Considering $\langle u_{2y} \rangle$ we have already concluded that $\langle u_{2y} \rangle \sim \delta k \langle u_{2x} \rangle$, and we are thus not generally interested in $\langle u_{2y} \rangle$ when we are in the regime of $\delta k \ll 1$. Nevertheless, we will derive $\langle u_{2y} \rangle$ to complete the theoretical treatment of the problem.

First $\langle \psi_2 \rangle$ and $\langle \phi_2 \rangle$ are calculated from Eqs. (3.22) and (3.25), and the first-order fields Eqs. (3.1a) and (3.4)

$$\begin{aligned} \langle \psi_2 \rangle = {} & \frac{3}{8} \frac{u_0^2}{c} \delta \sin(2kx)\, e^{-y/\delta} \left[\frac{4}{3} \cos(y/\delta) + \frac{2}{3} \sin(y/\delta) + \frac{1}{6} e^{-y/\delta} \right] \\ & + \mathcal{O}(k\delta) , \quad \text{for } 0 < \mathrm{y} < 7\delta, \end{aligned} \tag{3.29b}$$

$$\begin{aligned} \langle \phi_2 \rangle = {} & \frac{1}{4} \frac{u_0^2}{c} k\delta^2 \cos^2(kx)\, e^{-y/\delta} \cos(y/\delta) \\ & + \mathcal{O}(k\delta) , \quad \text{for } 0 < \mathrm{y} < 7\delta. \end{aligned} \tag{3.29c}$$

Inserting in the decomposition Eq. (3.16) we find

$$\begin{aligned}\langle u_{2y}\rangle &= -\frac{1}{4}\frac{u_0^2}{c}k\delta\cos(2kx)\,e^{-y/\delta}\left[4\cos(y/\delta)+2\sin(y/\delta)+\frac{1}{2}e^{-y/\delta}\right]\\ &\quad -\frac{1}{4}\frac{u_0^2}{c}k\delta\cos^2(kx)\,e^{-y/\delta}\left[\cos(y/\delta)+\sin(y/\delta)\right]\\ &\quad +\mathcal{O}(k\delta), \quad \text{for } 0<\mathrm{y}<7\delta. \end{aligned} \tag{3.29d}$$

The solution to the time-averaged second-order velocity field Eq. (3.29) differs from the solution proposed by Rayleigh in his equation R.(87) and R.(88) [1]. However, the magnitude of $\langle u_{2x}\rangle$ at the wall is in agreement, and that is what determines the bulk velocity field.

This finishes the treatment of the second order boundary velocity field $\langle \boldsymbol{u}_2\rangle$. As $\langle v_{2y}\rangle$ is an order of $k\delta$ smaller than $\langle v_{2x}\rangle$, only the expression (3.29a) will be visualized in Section 3.5. We now move on to derive the expressions for the second order pressure $\langle p_2\rangle$, which will be the subject of the next section.

3.3 Second-order pressure

In this section the magnitude of the three parts of the second-order pressure are compared, and we show that both the homogeneous solution $\langle Q_2\rangle$ and the particular boundary solution $\langle \chi_2\rangle$ are negligible to order ϵ relative to the particular bulk solution $\langle X_2\rangle$. To begin with the expression for $\langle X_2\rangle$ is derived and afterward an order of magnitude comparison to $\langle Q_2\rangle$ and $\langle \chi_2\rangle$ is made.

According to Eq. (2.51b) $\langle X_2\rangle$ is a bulk field driven by bulk source terms and is thus expected to vary on a length scale of λ. Inserting the first-order bulk fields Eq. (3.1) into Eq. (2.51b), calculating the source terms, and integrating twice with respect to x yields

$$\langle X_2\rangle = -\frac{1}{4}\rho_0 u_0^2\cos(2kx)\,. \tag{3.30}$$

As the homogeneous solution is covered by $\langle Q_2\rangle$ no integration constants are included in Eq. (3.30). The order of magnitude of $\langle Q_2\rangle$ and $\langle \chi_2\rangle$ are now considered and compared to Eq. (3.30). According to Eq. (2.51c) $\langle \chi_2\rangle$ is driven by boundary source terms and the Laplace operator can thus be approximated by $\nabla^2\langle \chi_2\rangle \approx \partial_y^2\langle \chi_2\rangle \sim \langle \chi_2\rangle/\delta^2$ and the order of magnitude of $\langle \chi_2\rangle$ become

$$\langle \chi_2\rangle \sim \epsilon\rho_0 u_0^2. \tag{3.31}$$

As the order of magnitude of $\langle Q_2\rangle$ cannot be determined from Eq. (2.51a) we return to the second-order Navier–Stokes equation Eq. (2.38). The gradients of $\langle X_2\rangle$ and $\langle \chi_2\rangle$ cancel out with the right hand source terms by definition using Eqs. (2.51b) and (2.51c), and the homogeneous equation become

$$\eta\nabla^2\langle \boldsymbol{U}_2\rangle - \boldsymbol{\nabla}\langle Q_2\rangle = 0. \tag{3.32}$$

The order of magnitude of $\langle \boldsymbol{U}_2 \rangle \sim u_0^2/c$ is given by $\langle \boldsymbol{u}_2 \rangle$ through the boundary condition Eq. (2.47) and as the bulk fields $\langle \boldsymbol{U}_2 \rangle$ and $\langle Q_2 \rangle$ vary on a length scale of λ the order of magnitude of $\langle Q_2 \rangle$ become

$$\langle Q_2 \rangle \quad \sim \quad \epsilon \rho_0 u_0^2, \tag{3.33}$$

where we have used $\eta \sim \rho_0 \omega \delta^2$. Comparing Eqs. (3.30), (3.31) and (3.33) it is clear that the time-averaged second-order pressure can be approximated by

$$\langle p_2 \rangle \quad \approx \quad \langle X_2 \rangle + \mathcal{O}(\epsilon). \tag{3.34}$$

Consequently, $\langle p_2 \rangle$ is given entirely in terms of the first-order bulk fields and does not depend on viscous boundary effects. We now move on to derive the expressions for $\langle \boldsymbol{U}_2 \rangle$, which will be the subject of the next section.

3.4 Second-order velocity outside the boundary layer

In this section we are going to solve the homogeneous Navier–Stokes equation (3.32) in order to obtain the expressions for $\langle \boldsymbol{U}_2 \rangle$ and $\langle Q_2 \rangle$ in the case of a single wall. According to Eq. (2.48a) $\langle \boldsymbol{U}_2 \rangle$ is incompressible, and as $\langle \boldsymbol{U}_2 \rangle$ is only driven by the boundary condition Eq. (2.47) it is expected to vary on a length scale of λ in either direction. It is important to note that $\langle \boldsymbol{U}_2 \rangle$ is not inviscid. $\langle \boldsymbol{U}_2 \rangle$ does indeed depend on the position of the wall, which $\boldsymbol{U}_1$ did not, due to the boundary condition Eq. (2.47) determined by $\langle \boldsymbol{u}_2 \rangle$. Evaluating Eq. (3.29) at $y = 0$ the boundary condition for $\langle \boldsymbol{U}_2 \rangle$ become

$$\langle U_{2x} \rangle \Big|_{y=0} \quad = \quad \frac{3}{8} \frac{u_0^2}{c} \sin(2kx), \tag{3.35a}$$

$$\langle U_{2y} \rangle \Big|_{y=0} \quad = \quad \frac{1}{4} \frac{u_0^2}{c} k\delta \left[\cos^2(kx) + \frac{9}{2} \cos(2kx) \right] = 0 + \mathcal{O}(k\delta), \tag{3.35b}$$

where to zeroth order in $k\delta$ the boundary condition on $\langle U_{2y} \rangle$ becomes zero. This is the acoustic streaming boundary condition for the bulk velocity field, as sketched in Figure 3.3. This boundary condition will also be used when deriving the acoustic streaming in microfluidic channels in Chapter 4.

Since $\langle \boldsymbol{U}_2 \rangle$ is expected to vary on a length scale of λ in either direction we cannot approximate the Laplace operator in Eq. (2.46a) and instead of solving the rotation of the Navier–Stokes equation we return to the homogeneous time-averaged second-order Navier–Stokes equation (3.32). Considering the Laplace equation (2.51a), the boundary condition Eq. (3.35), the geometry, and requiring $\langle \boldsymbol{U}_2 \rangle \to \boldsymbol{0}$ for $y \to \infty$, we make the ansatz

$$\langle Q_2 \rangle \quad = \quad A \cos(2kx) \, \mathrm{e}^{-2ky}. \tag{3.36}$$

Since $\langle \boldsymbol{U}_2 \rangle$ is incompressible it can be expressed through a stream function $\langle \Psi_2 \rangle$

$$\langle U_{2x} \rangle \quad = \quad \partial_y \langle \Psi_2 \rangle, \tag{3.37a}$$

$$\langle U_{2y} \rangle \quad = \quad -\partial_x \langle \Psi_2 \rangle, \tag{3.37b}$$

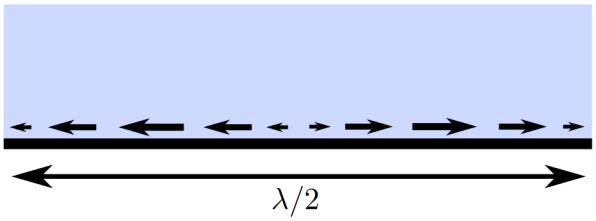

Figure 3.3: Sketch of the acoustic streaming boundary condition for the bulk velocity field. This effective boundary condition is correct to order $\mathcal{O}(k\delta)$ and result from non-linear interactions of the first-order fields in the acoustic boundary layer.

and considering Eq. (3.36) our ansatz for the stream function becomes

$$\langle \Psi_2 \rangle = \sin(2kx) f(y). \tag{3.38}$$

In order to determine $f(y)$ we insert Eqs. (3.36) and (3.38) into the y-component of the homogeneous Navier–Stokes equation (3.32) to obtain

$$f''(y) - 4k^2 f(y) = \frac{A}{\eta} \mathrm{e}^{-2ky}, \tag{3.39}$$

where the prime indicates differentiation with respect to the argument, in this case y. The complete solution to Eq. (3.39) become

$$f(y) = -\frac{A}{4k\eta} y \mathrm{e}^{-2ky} + B\mathrm{e}^{2ky} + C\mathrm{e}^{-2ky}, \tag{3.40}$$

where $f(y) = -\frac{A}{4k\eta} y \mathrm{e}^{-2ky}$ is a particular solution to Eq. (3.39) and $B\mathrm{e}^{2ky} + C\mathrm{e}^{-2ky}$ solves the homogeneous equation. The boundary conditions Eq. (3.35) require $f'(0) = \frac{3}{8}\frac{u_0^2}{c}$ and $f(0) = 0$, and the condition $\langle \boldsymbol{U}_2 \rangle \to \mathbf{0}$ for $y \to \infty$ demands $f(\infty) = 0$, leading to

$$A = -\frac{3}{2}\frac{u_0^2}{c} k\eta, \tag{3.41a}$$
$$B = 0, \tag{3.41b}$$
$$C = 0, \tag{3.41c}$$

and $\langle \boldsymbol{U}_2 \rangle$ become

$$\langle U_{2x} \rangle = \frac{3}{8}\frac{u_0^2}{c} \sin(2kx)(1 - 2ky)\mathrm{e}^{-2ky} + \mathcal{O}(k\delta), \tag{3.42a}$$
$$\langle U_{2y} \rangle = -\frac{3}{8}\frac{u_0^2}{c} \cos(2kx) 2ky \mathrm{e}^{-2ky} + \mathcal{O}(k\delta). \tag{3.42b}$$

We have now calculated the time-averaged second-order velocity field and pressure field to zeroth order in $k\delta$. In the next section the results will be illustrated and discussed.

3.5 Results and Discussion

We will now have a closer look at the second-order velocity field $\langle \boldsymbol{v}_2 \rangle = \langle \boldsymbol{U}_2 \rangle + \langle \boldsymbol{u}_2 \rangle$ given by Eqs. (3.29) and (3.42). In order to normalize the velocity field we define the streaming velocity constant $u_{\text{str}} = \frac{3}{8}\frac{u_0^2}{c}$. Figure 3.4 shows the x-component of the time-averaged second-order velocity field close to the boundary, normalized to u_{str}. Moving away from the boundary $\langle v_{2x} \rangle$ converge towards $u_{\text{str}} \sin(2kx)$. Close to the wall there is a sign change of $\langle v_{2x} \rangle$ which results in a steady rotational motion of the fluid inside the viscous boundary layer. Close to the wall the streaming velocity is directed towards the first-order pressure node at $kx = 0$, while outside the boundary layer the streaming velocity is directed away from the pressure node. This is known as the inner vortices or Schlichting streaming, see Boluriaan [27].

We now return to the physical interpretation of the generation of the streaming velocity shown in Figure 3.4. As indicated in Eq. (3.7) the non-linear interactions of the first-order fields give rise to a steady vorticity source density S inside the boundary layer. Figure 3.5 shows the time-averaged vorticity $\langle \zeta_2 \rangle$, normalized to u_{str}/δ, along with arrows indicating the magnitude of $\langle v_{2x} \rangle$. The rotational motion is generated inside the boundary layer and momentum diffuse away from the boundary as the velocity gradients in the y-direction are much larger than those in the x-direction, which is realized by recalling the different scaling in the two directions on the graph.

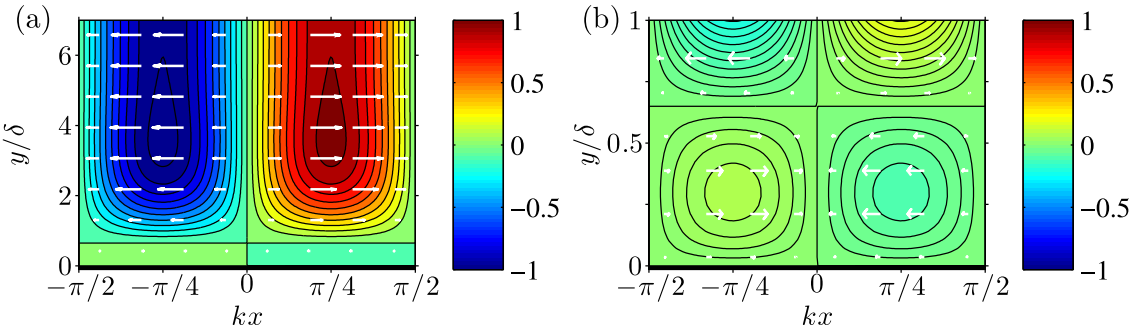

Figure 3.4: Color and vector plot of the x-component of the time-averaged second-order velocity field $\langle v_{2x} \rangle$ close to the boundary, normalized to $u_{\text{str}} = \frac{3}{8}u_0^2/c$. The whole boundary layer of thickness 7δ is shown in (a), while a zoom in close to the wall in shown in (b). (a) Moving away from the wall $\langle v_{2x} \rangle$ converge towards $u_{\text{str}} \sin(2kx)$, which is the acoustic streaming boundary condition for the second-order bulk velocity field. (b) Close to the wall the sign change of $\langle v_{2x} \rangle$ result in a rotational flow inside the boundary layer.

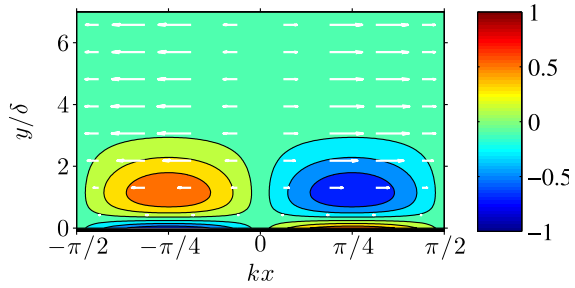

Figure 3.5: Color plot of the time-averaged second-order vorticity $\langle \zeta_2 \rangle$ normalized to u_{str}/δ and vector plot of $\langle v_{2x} \rangle$. The vorticity is generated close to the boundary by the non-linear interactions of the first-order velocity field. Momentum diffuse away from the boundary region due to large velocity gradients in the y-direction.

We now turn to the bulk velocity field $\langle \boldsymbol{U}_2 \rangle$ given by Eq. (3.42) and shown in Figure 3.6. The rotational flow consist of flow rolls with a width of $\lambda/4$ and the center of rotation a distance $\lambda/(4\pi)$ from the wall. Close to the wall the streaming velocity is given by $u_{\text{str}} \sin(2kx)$, directed away from the pressure node in the center of the channel. Further away from the wall the velocity decays exponentially while turning towards the pressure node in the center. These bulk flow rolls are referred to as outer vortices or Rayleigh streaming, see Boluriaan [27] and Rayleigh [1]. It is important to remember that the steady rotational flow is driven entirely by the non-linear interactions of the first-order fields inside the thin viscous boundary layer of thickness δ, which is not resolved in Figure 3.6.

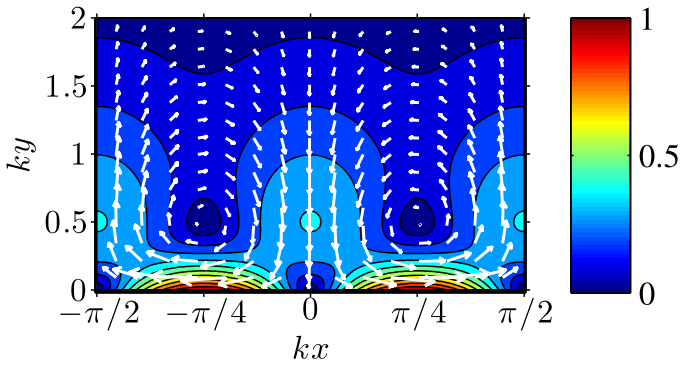

Figure 3.6: Color and vector plot of the time-averaged second-order bulk velocity field $\langle \boldsymbol{U}_2 \rangle$, giving by Eq. (3.42), normalized to u_{str}. It should be noted that the scaling is equal in this figure. The bulk flow rolls are generated by non-linear interactions of the first-order fields inside the thin viscous boundary layer and decay exponentially away from the wall. Close to the wall the flow is directed away from the first-order pressure node at $kx = 0$, while out in the bulk the flow turns towards the center.

3.6 Concluding remarks

In this chapter we have treated the acoustic streaming at a single planar wall in the case of a standing first-order bulk wave. Expressions for the inner and outer second-order streaming velocity fields have been derived, accounting for both the inner boundary layer streaming rolls and the outer bulk streaming rolls. Following our novel approach, we encountered a limitation in the derivation of an analytical solution to the first-order boundary velocity field, which demanded the implementation of an artificial bounding, ensuring that the solution for the first-order boundary velocity field did not spread into the bulk. This artificial bounding is similar to the division into a bulk and a boundary region, used in the common approach to acoustic streaming [57,63]. This illustrated why it is necessary to apply boundary-layer theory or similar measures in order to solve the acoustic streaming problem analytically. The acoustic streaming boundary condition for the second-order bulk velocity field forms the basis for the derivation of acoustic streaming in different microfluidic channels, treated in the next chapter.

3.6.1 Analytical outlook

To improve the analytical derivation of the acoustic fields inside the boundary layer we should focus on improving the analytical first-order solution. At the very end of this project, we realized that the solution for the first-order density would be affected by the presence of the wall, in contrast to the assumption made in Section 2.5. The expression for the first-order density is only correct to order $\mathcal{O}(k\delta)$, and not to order $\mathcal{O}(\epsilon)$ as assumed. This explains why we can only determine the first-order velocity to order $\mathcal{O}(k\delta)$. The density is also assumed to be independent of the wall in the common approach to acoustic streaming [57, 63], utilizing boundary-layer theory. This calls for a further improvement of the theory of acoustic streaming. For now we briefly outline the revised assumptions and consequences.

The influence of bulk losses on the first-order density is negligible to order $\mathcal{O}(\epsilon)$, while the influence of the wall is only negligible to order $\mathcal{O}(k\delta)$ (or $\mathcal{O}(\sqrt{\epsilon})$) . This introduces a y-dependent component of the first-order density, and consequently a y-component of the first-order velocity, spreading into the bulk. Because of this y-component of the first-order bulk velocity, we can no longer treat the single wall case, instead we must consider a domain between two parallel plates. This allows us to solve the problem of acoustic streaming with our novel approach, without introducing the artificial bounding.

We do not expect this revision of the first-order theory to alter the acoustic streaming boundary condition for the second-order bulk velocity field, and consequently the results of Chapter 4 for the acoustic streaming in microfluidic channels will still be valid.

Chapter 4

Acoustic streaming in microfluidic channels

In this chapter the acoustic streaming in microfluidic channels is considered, limited to square geometries with one dimensional resonances. We only consider cases where the boundary layer thickness is much smaller than the channel height, $\delta \ll h$, as this is typical for microchannel acoustophoresis devices. The case of $\delta \sim h$ is treated by Hamilton [25]. To start with we consider the streaming between two parallel plates in the two cases of $h \ll \lambda$ and $h \sim \lambda$. Finally, the rectangular channel is considered, which is relevant in relation to experimental devices utilizing standing ultrasound waves, such as Barnkob [51] and Augustsson [52]. To our knowledge the acoustic streaming in rectangular channels has not been treated in the literature before.

4.1 Thin parallel-plates channel

In this section we investigate the acoustic streaming between two parallel planar walls separated by a distance $h \ll \lambda$. This restriction of the height ensures that the variations in the vertical direction of the time-averaged second-order velocity is much greater than the variations along the horizontal direction, i.e. $\nabla^2 \langle \boldsymbol{v}_2 \rangle = \partial_y^2 \langle \boldsymbol{v}_2 \rangle + \mathcal{O}\left((kh)^2\right)$ everywhere, which greatly simplifies the governing equations for the bulk field. The case considered in this section is thus described by

$$\delta \ll h \ll \lambda. \tag{4.1}$$

When the walls are far apart relative to the thickness of the viscous boundary layer, the viscous boundary field $\boldsymbol{u}_1$ at one wall does not depend on the presence of the other wall. This is because "information" about the presence of the wall vanishes on a length scale of a few δ, when considering the first-order fields. We can thus use the first-order boundary fields of Section 3.1, applying the boundary field $\boldsymbol{u}_1$ at both walls. Consequently, the

non-linear interactions of the first-order fields lead to the same second-order boundary field $\langle \boldsymbol{u}_2 \rangle$, as calculated in the one wall case, and thus also the same acoustic streaming boundary condition, Eq. (3.35), for the second-order bulk field $\langle \boldsymbol{U}_2 \rangle$. Changing the y-coordinate so that the walls are positioned at $\pm h/2$ the governing equations and boundary conditions for $\langle \boldsymbol{U}_2 \rangle$ to zeroth order in $k\delta$ become

$$\begin{aligned}
\eta \nabla^2 \langle \boldsymbol{U}_2 \rangle - \boldsymbol{\nabla} \langle Q_2 \rangle &= \mathbf{0}, && \text{(4.2a)} \\
\boldsymbol{\nabla} \cdot \langle \boldsymbol{U}_2 \rangle &= 0, && \text{(4.2b)} \\
\nabla^2 \langle Q_2 \rangle &= 0, && \text{(4.2c)} \\
\langle U_{2x} \rangle \Big|_{y=\pm h/2} &= \frac{3}{8} \frac{u_0^2}{c} \sin(2kx), && \text{(4.2d)} \\
\langle U_{2y} \rangle \Big|_{y=\pm h/2} &= 0, && \text{(4.2e)}
\end{aligned}$$

where Eqs. (4.2a), (4.2b) and (4.2c) are reprints of Eqs. (3.32), (2.48a) and (2.51a), respectively. The set of equations (4.2) governs the parallel-plates problem in the case of $\delta \ll h$. Expressing the incompressible $\langle \boldsymbol{U}_2 \rangle$ through a stream function as in Eq. (3.37), it proves advantageous to take the rotation of Eq. (4.2a) to obtain a biharmonic equation for $\langle \Psi_2 \rangle$

$$\nabla^2 \nabla^2 \langle \Psi_2 \rangle = 0. \tag{4.3}$$

In the case of $h \ll \lambda$ the Laplace operator can be approximated by

$$\nabla^2 \langle \Psi_2 \rangle = \partial_y^2 \langle \Psi_2 \rangle + \mathcal{O}\left((kh)^2\right), \tag{4.4}$$

and Eq. (4.3) become

$$\partial_y^4 \langle \Psi_2 \rangle = 0. \tag{4.5}$$

This leads to the general solution

$$\langle \Psi_2 \rangle = A(x)\, y^3 + B(x)\, y^2 + C(x)\, y + D(x), \tag{4.6}$$

and applying the boundary conditions Eqs. (4.2d) and (4.2e) we obtain

$$\begin{aligned}
\langle U_{2x} \rangle &= \frac{3}{8} \frac{u_0^2}{c} \sin(2kx) \left[\frac{3}{2} \frac{y^2}{\left(\frac{1}{2}h\right)^2} - \frac{1}{2} \right], && \text{(4.7a)} \\
\langle U_{2y} \rangle &= \frac{3}{16} \frac{u_0^2}{c} kh \cos(2kx) \left[\frac{y}{\frac{1}{2}h} - \frac{y^3}{\left(\frac{1}{2}h\right)^3} \right]. && \text{(4.7b)}
\end{aligned}$$

These field expressions are in agreement with those found in Rayleigh [1] equation R.(93) and R.(94). In this case of a thin channel $h \ll \lambda$ the variations in the x-direction are much

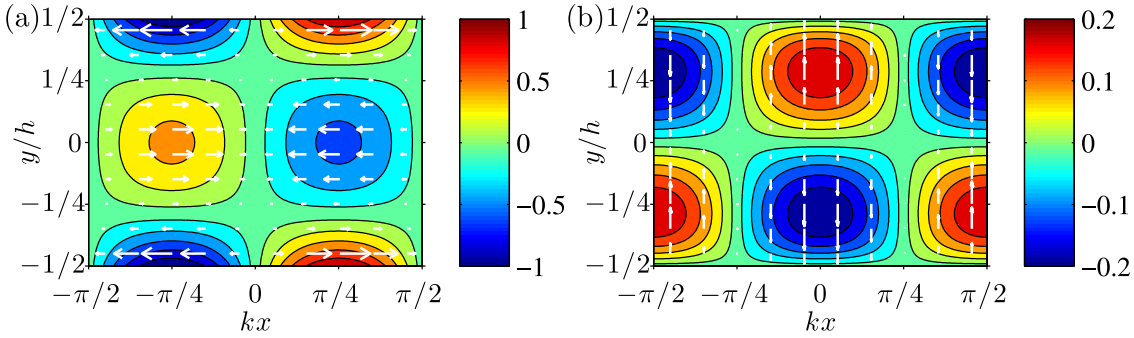

Figure 4.1: Color and vector plot of the time-averaged second-order velocity field $\langle \boldsymbol{U}_2 \rangle$ between two parallel plates positioned at $y/h = \pm\frac{1}{2}$ and separated by a distance $h \ll \lambda$. (a) The x-component of the acoustic streaming velocity, $\langle U_{2x} \rangle$, normalized to u_{str}. The amplitude of $\langle U_{2x} \rangle$ in the horizontal center plane of the channel, $y/h = 0$, is $\frac{1}{2}u_{\text{str}}$, independent of the channel height, as long as the criteria $h \ll \lambda$ is fulfilled. (b) The y-component of the acoustic streaming velocity, $\langle U_{2y} \rangle$, normalized to $u_{\text{str}}kh$.

slower than those in the y-direction, and consequently $\langle U_{2y} \rangle$ is an order of kh smaller than $\langle U_{2x} \rangle$, since $\langle \boldsymbol{U}_2 \rangle$ is incompressible. The two velocity components Eqs. (4.7a) and (4.7b) are plotted separately in Figure 4.1. There are two flow rolls in the height of the channel and the rolls have a width of $\lambda/4$, as in the single wall case. The perpendicular distance from the wall to the rotation centers is $d_{rc} = \frac{3-\sqrt{3}}{6}h$. The amplitude of $\langle U_{2x} \rangle$ is largest at the walls, where it is driven by the non-linear interactions of the first-order fields within the viscous boundary layer. A local minimum in $\langle U_{2x} \rangle$, considering the vertical line at $kx = \pi/4$, is found at the center plane of the channel, $y/h = 0$, and the velocity at this minimum is $U_{2x,min} = \frac{1}{2}u_{\text{str}}$, independent of the channel height, as long as $h \ll \lambda$.

4.2 High parallel-plates channel

In devices used for acoustophoresis the height of the channel is usually not much smaller than the wavelength, [52]. It is thus relevant to consider the acoustic streaming in a parallel plate channel with $h \sim \lambda$, bringing the theoretical model one step closer to the physical devices. The governing equations and boundary conditions Eq. (4.2) are also valid for the case of $h \sim \lambda$. However, we cannot approximate the Laplace operator like we did in the thin channel case Eq. (4.4). Instead we follow the derivation carried out for $\langle \boldsymbol{U}_2 \rangle$ in the single planar wall case of Section 3.4. The ansatz for the homogeneous solution for the pressure now becomes

$$\langle Q_2 \rangle = A \cos(2kx) \cosh(2ky), \tag{4.8}$$

where only terms proportional to $\cosh(2ky)$ has been chosen, since the boundary condition for $\langle U_{2x} \rangle$ is even in y. We thus search for a stream function of the form $\langle \Psi_2 \rangle =$

$\sin(2kx)\, f(y)$ where $f(y)$ solves the differential equation

$$f''(y) - 4k^2 f(y) = -\frac{A}{\eta}\sinh(2ky), \tag{4.9}$$

obtained by inserting in the homogeneous Navier–Stokes equation (3.32). The solution to this ordinary differential equation, fulfilling the demand of $\langle U_{2x}\rangle$ being even in y, is

$$f(y) = -\frac{A}{4k\eta} y\cosh(2ky) + B\sinh(2ky), \tag{4.10}$$

where $\sinh(2ky)$ solves the homogeneous equation and $-\frac{A}{4k\eta} y\cosh(2ky)$ is a particular solution to the inhomogeneous equation (4.9). This general structure of the stream function is mentioned in Rayleigh [1] equation (85), however, in the further treatment he only considers the case $h \ll \lambda$. The boundary conditions Eqs. (4.2d) and (4.2e) demands $f'(0) = \frac{3}{8}\frac{u_0^2}{c}$ and $f(0) = 0$, yielding

$$A = -\frac{3}{2}k\eta\frac{u_0^2}{c}\frac{\sinh(kh)}{\sinh(kh)\cosh(kh) - kh}, \tag{4.11a}$$

$$B = -\frac{3}{16}h\frac{u_0^2}{c}\frac{\cosh(kh)}{\sinh(kh)\cosh(kh) - kh}. \tag{4.11b}$$

The expression for the stream function becomes

$$\langle \Psi_2\rangle = \frac{3}{8}\frac{u_0^2}{c}\sin(2kx)\,\Gamma(\alpha)\left[y\cosh(2ky) - \coth(\alpha)\,\frac{h}{2}\sinh(2ky)\right], \tag{4.12}$$

where we have defined two geometric variables α and $\Gamma(\alpha)$

$$\alpha = kh, \tag{4.13}$$

$$\Gamma(\alpha) = \frac{\sinh(\alpha)}{\sinh(\alpha)\cosh(\alpha) - \alpha}. \tag{4.14}$$

Finally the expression for $\langle \boldsymbol{U}_2\rangle$ becomes

$$\langle U_{2x}\rangle = \frac{3}{8}\frac{u_0^2}{c}\sin(2kx)\,\Gamma(\alpha)\left\{\left[1 - \coth(\alpha)\,\alpha\right]\cosh(2ky) + 2ky\sinh(2ky)\right\}, \tag{4.15a}$$

$$\langle U_{2y}\rangle = -\frac{3}{8}\frac{u_0^2}{c}\cos(2kx)\,\Gamma(\alpha)\left\{2ky\cosh(2ky) - \alpha\coth(\alpha)\sinh(2ky)\right\}. \tag{4.15b}$$

The expression Eq. (4.15) for the high parallel-plates channel converges towards the expression Eq. (4.7) for the thin parallel-plates channel when $\alpha \to 0$.

The acoustic streaming velocity field $\langle \boldsymbol{U}_2 \rangle$ for the high parallel plate channel, Eq. (4.15), is shown in Figure 4.2. The velocity field is normalized to u_{str} and shown for the three aspect ratios $h/w = 2$, $h/w = 1$, and $h/w = 1/5$. The relation between the aspect ratio and the α-parameter is $\alpha = \pi h/w$. The clear difference, compared to the thin channel Figure 4.1, is that $\langle U_{2y} \rangle$ is now of the same order of magnitude as $\langle U_{2x} \rangle$, and hence the vector field $\langle \boldsymbol{U}_2 \rangle$ can be visualized. The width of the rolls are still $\lambda/4$ as this is governed solely by the wavelength and not the dimensions in the y-direction. Figure 4.3 (a) show $\langle U_{2x} \rangle$ along the vertical line at $kx = \pi/4$, going through the rotation center of the roll. For low aspect ratios the local minimum is found in the center of the channel

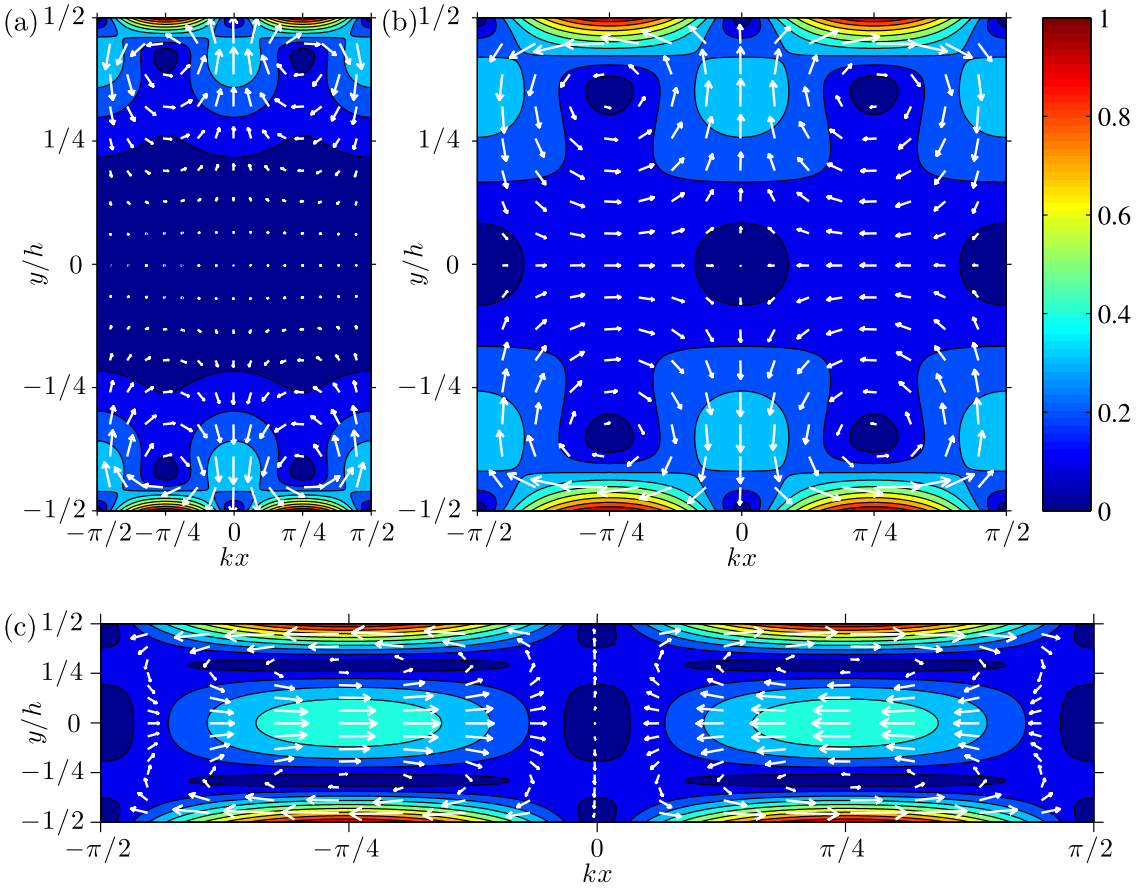

Figure 4.2: Color and vector plot of the time-averaged second-order velocity field $\langle \boldsymbol{U}_2 \rangle$ between two parallel plates positioned at $y/h = \pm\frac{1}{2}$ and separated by a distance $h \sim \lambda$. $\langle \boldsymbol{U}_2 \rangle$ is given by Eq. (4.15) and has been normalized to u_{str}. The acoustic streaming velocity field is shown for three different aspect ratios: (a) $h/w = 2$, (b) $h/w = 1$, and (c) $h/w = 1/5$, where w is the width of a half-wavelength section of the infinite plates, $w = \lambda/2$. (a) The magnitude of the velocity field is significant only close to the plates. (b) The magnitude of the velocity field is significant everywhere, but the amplitude in the horizontal center plane is lower than $\frac{1}{2}u_{\text{str}}$. (c) The velocity field resembles that of the thin parallel-plates channel, and the amplitude in the horizontal center plane is close to $\frac{1}{2}u_{\text{str}}$.

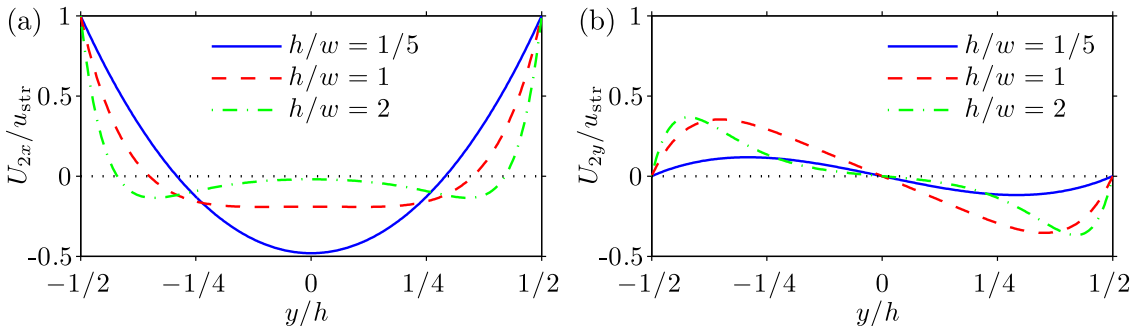

Figure 4.3: (a) The horizontal second-order velocity, $\langle U_{2x}\rangle$, along the vertical line at $kx = \pi/4$, going through the rotation center of the flow roll. For the low aspect ratio, $h/w = 1/5$, the flow rolls meet in the center, resulting in a local minimum. For the large aspect ratio, $h/w = 2$, each roll decay towards the center, and the local minimum is reaches before the center. The positions of the rotation centers are given by the nodes of the curves, where $\langle U_{2x}\rangle = 0$. (b) Vertical second-order velocity, $\langle U_{2y}\rangle$, along the vertical line at $kx = \pi/2$. For low aspect ratios $\langle U_{2y}\rangle$ resembles a sine, while for larger aspect ratios it decays towards the center.

where the two flow roll meet. For larger aspect ratios the flow rolls decay before they meet in the center, and a minimum exist on either side away from the center. Figure 4.3 (b) shows $\langle U_{2y}\rangle$ along the vertical line at $kx = \pi/2$. For low aspect ratios the y-dependence of $\langle U_{2y}\rangle$ resembles a sine, while for larger aspect ratios it decays towards the center. This velocity on the boundary of the domain remind us that the parallel-plates channel is in principle infinite in the x-direction. The width, w, considered here corresponds a section of the channel of width $\lambda/2$, and the boundaries at $kx = \pm\pi/2$ are symmetry axes for the second-order fields.

The distance from the wall to the centers of rotation is now more difficult to determine, compared to the thin plates channel. The y-coordinate of the rotation centers is given by the roots in the equation $\langle U_{2x}\rangle(y) = 0$ leading to

$$\Big[1 - \coth(\alpha)\,\alpha\Big]\cosh(2ky) + 2ky\sinh(2ky) \quad = \quad 0. \tag{4.16}$$

We are not able to obtain an analytical solution to this equation, and we must thus limit ourselves to numerical solutions. Figure 4.4 (a) shows the perpendicular distance from the wall to the local minimum in $\langle U_{2x}\rangle$, d_{min}, and to the rotation center, d_{rc}, as a function of the aspect ratio h/w. Both length scales have been normalized to the domain width $w = \lambda/2$. Considering d_{min}, the linear region for low h/w corresponds to the local minimum being at the center plane, and consequently d_{min} increases linearly with h. Just before the aspect ratio reaches unity, the amplitude of $\langle U_{2x}\rangle$ starts to decay slightly before reaching the center, and the local minimum is no longer found at the center. For large h/w the structure of the rolls is independent of the channel height, since the rolls on either side do not "feel" each other. As a consequence both the d_{min} and d_{rc} become independent of h. For d_{rc} the linear region for low h/w corresponds to the thin parallel-plates case, where d_{rc} is given by $d_{\mathrm{rc}} = \frac{3-\sqrt{3}}{6}h$.

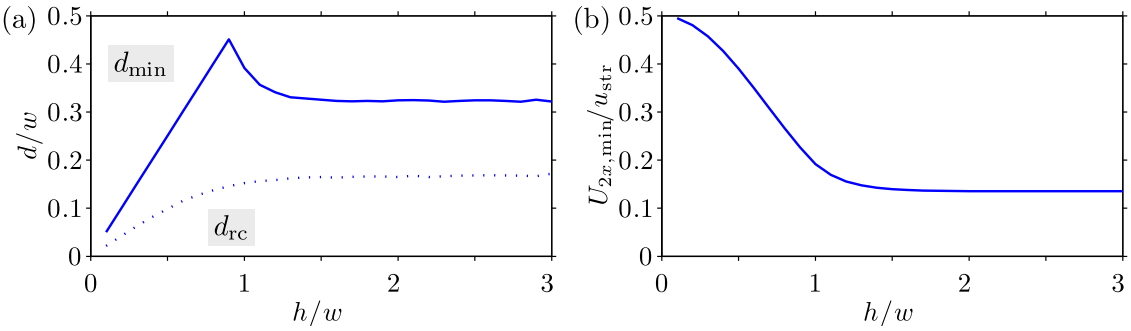

Figure 4.4: (a) Perpendicular distances from the wall to the local minima in $\langle U_{2x}\rangle$, $d_{\min}$, and to the rotation center, $d_{\rm rc}$, normalized to the domain width w. These two length scales can be seen on the graphs in Figure 4.3 (a) as the distance to the local minimum and the node, respectively. The linear regimes for low h/w corresponds to $d_{\min}$ and $d_{\rm rc}$ being proportional to h, as in the thin plates channel. For larger h/w, the structure of the rolls, and hence $d_{\min}$ and $d_{\rm rc}$, become independent of h, as the rolls on either sides do not "feel" one another. (b) Amplitude of $\langle U_{2x}\rangle$ at the local minima. In the limiting case of the thin plates channel, $h/w \to 0$, $U_{2x,\min} = \frac{1}{2}u_{\rm str}$. As h/w increases, $U_{2x,\min}$ decreases until the point where the rolls become independent of one another, and $U_{2x,\min}$ becomes independent of h/w.

Figure 4.4 (b) shows the magnitude of $\langle U_{2x}\rangle$ at the local minima, $U_{2x,\min}$, normalized to $u_{\rm str}$. For very low aspect ratios $U_{2x,\min} = \frac{1}{2}u_{\rm str}$, as described in the thin parallel-plates case Section 4.1. Already while the position of the local minima is still in the center, $U_{2x,\min}$ decrease for increasing h/w. This can be understood as the amplitude of each separate roll decaying towards the center, but the combination of the two rolls still result in a local minimum at the center. For larger h/w the amplitude $U_{2x,\min}$ becomes independent of both the height and the width of the domain. Changing w, i.e. changing the acoustic wavelength λ, while keeping the aspect ratio h/w constant, scales the size of the flow rolls, hence scaling $d_{\min}$ and $d_{\rm rc}$. However, the amplitudes of the velocity field, including $u_{\rm str}$ and $U_{2x,\min}$, are unchanged. This is true as long as the thickness of the viscous boundary layer is much smaller than both the height of the channel and the acoustic wavelength.

4.3 Rectangular channel

In this section the acoustic streaming velocity field is derived for a rectangular microchannel in the case of $\delta \ll h$ and $\delta \ll \lambda$. The challenge in this problem, compared to the high parallel-plates channel problem of Section 4.2, is that the velocity field have to fulfill the no-slip boundary condition at the sidewalls positioned at $kx = \pm\pi/2$. We will first derive a simple correction to the parallel-plates solution, before we propose an iterative Fourier approach, expanding the velocity field into an infinite series.

As a starting point the solution for the high parallel-plates is considered. The x-component of both the first and second-order velocity fields already fulfill the no-slip condition on the side walls due to their $\cos(kx)$ and $\sin(2kx)$ dependence. For the y-

component inside the boundary layer the effect of the side walls can be neglected due the small thickness of the boundary layer compared to the width of the channel. The last field component is the y-component of the second-order bulk field, $\langle U_{2y} \rangle$, which does not fulfill the no-slip condition on the side walls. This error cannot be neglected as it is present along the hole side boundary and its magnitude is not negligible.

The governing equations and boundary conditions are the same as for the parallel-plates channel, Eq. (4.2), along with the new no-slip condition at the side walls

$$\langle \boldsymbol{U}_2 \rangle \Big|_{kx=\pm\pi/2} = \boldsymbol{0}. \tag{4.17}$$

There is no elegant analytical solution to this system of equations, so instead we expand $\langle \boldsymbol{U}_2 \rangle$ in a sum of Fourier expansions. To illustrate the idea of this method we start out by making a simple correction to expression for the high parallel-plates channel Eq. (4.15), from now on denoted $\langle \boldsymbol{U}_2^{\text{plates}} \rangle$. Secondly we correct $\langle \boldsymbol{U}_2^{\text{plates}} \rangle$ by a single Fourier sum, and lastly we expand $\langle \boldsymbol{U}_2 \rangle$ in a sum of Fourier expansions.

4.3.1 Simple correction field

We start out by expanding $\langle \boldsymbol{U}_2 \rangle$ and $\langle Q_2 \rangle$

$$\langle \boldsymbol{U}_2 \rangle = \langle \boldsymbol{U}_2^{\text{plates}} \rangle + \langle \boldsymbol{U}_2^{\text{cor}} \rangle, \tag{4.18}$$

$$\langle Q_2 \rangle = \langle Q_2^{\text{plates}} \rangle + \langle Q_2^{\text{cor}} \rangle, \tag{4.19}$$

where $\langle \boldsymbol{U}_2^{\text{cor}} \rangle$ is a correction to the high parallel-plates field $\langle \boldsymbol{U}_2^{\text{plates}} \rangle$, making $\langle \boldsymbol{U}_2 \rangle$ fulfill the equations for the rectangular channel. The equations and boundary conditions governing $\langle \boldsymbol{U}_2^{\text{cor}} \rangle$ thus become

$$\eta \nabla^2 \langle \boldsymbol{U}_2^{\text{cor}} \rangle - \boldsymbol{\nabla} \langle Q_2^{\text{cor}} \rangle = \boldsymbol{0}, \tag{4.20a}$$

$$\boldsymbol{\nabla} \cdot \langle \boldsymbol{U}_2^{\text{cor}} \rangle = 0, \tag{4.20b}$$

$$\nabla^2 \langle Q_2^{\text{cor}} \rangle = 0, \tag{4.20c}$$

$$\langle U_{2x}^{\text{cor}} \rangle = 0 \quad , \text{ for } \boldsymbol{r} \in \partial\Omega, \tag{4.20d}$$

$$\left\langle U_{2y}^{\text{cor}} \right\rangle = -\langle U_{2y}^{\text{plates}} \rangle \quad , \text{ for } \boldsymbol{r} \in \partial\Omega. \tag{4.20e}$$

Considering the value of $\langle \boldsymbol{U}_2^{\text{plates}} \rangle$ on the boundaries, the boundary conditions for $\langle \boldsymbol{U}_2^{\text{cor}} \rangle$ become

$$\langle U_{2x}^{\text{cor}} \rangle = 0, \quad \text{for } ky = \pm\alpha/2, \tag{4.21a}$$

$$\left\langle U_{2y}^{\text{cor}} \right\rangle = 0, \quad \text{for } ky = \pm\alpha/2, \tag{4.21b}$$

$$\langle U_{2x}^{\text{cor}} \rangle = 0, \quad \text{for } kx = \pm\pi/2, \tag{4.21c}$$

$$\left\langle U_{2y}^{\text{cor}} \right\rangle = u_{\text{str}} \Gamma(\alpha) \left\{ 2ky \cosh(2ky) - \alpha \coth(\alpha) \sinh(2ky) \right\}, \quad \text{for } kx = \pm\pi/2. \tag{4.21d}$$

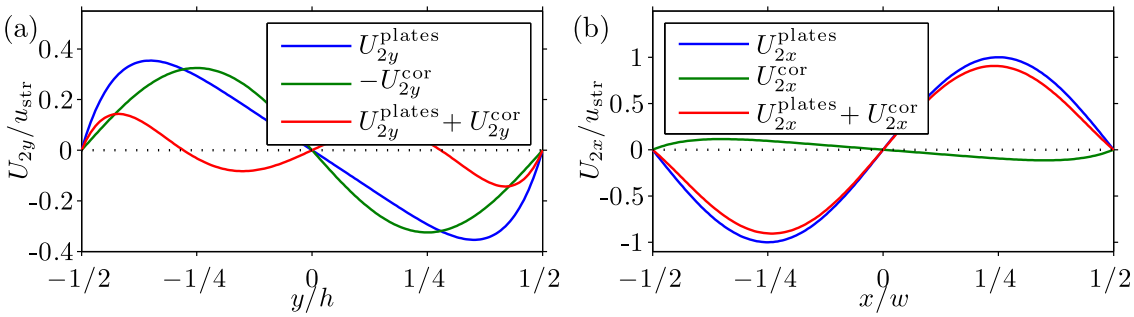

Figure 4.5: Time-average second-order bulk velocity fields on the boundaries of a rectangular channel with an aspect ratio of $h/w = 1$. (a) $\langle U_{2y}\rangle$ on the vertical boundaries. The y-component of the parallel-plates solution $\langle U_{2y}^{\text{plates}}\rangle$ on the vertical boundaries is approximated by a sine when making a simple correction field $\langle \boldsymbol{U}_2^{\text{cor}}\rangle$. On the graph $-\langle U_{2y}^{\text{cor}}\rangle$ is plotted in order to show how it only approximates $\langle U_{2y}^{\text{plates}}\rangle$. An error given by $\langle U_{2y}^{\text{plates}}\rangle + \langle U_{2y}^{\text{cor}}\rangle$ is still present, however, smaller than the original error given by $\langle U_{2y}^{\text{plates}}\rangle$. (b) $\langle U_{2x}\rangle$ on the horizontal boundaries. While $\langle \boldsymbol{U}_2^{\text{cor}}\rangle$ corrects the error on the vertical boundaries, it also introduces a small error on the horizontal boundaries given by $\langle U_{2x}^{\text{cor}}\rangle$.

The set of equations (4.20) and (4.21) governing $\langle \boldsymbol{U}_2^{\text{cor}}\rangle$ are just as difficult to solve as the initial problem of solving $\langle \boldsymbol{U}_2\rangle$ for the rectangular channel. However, we can find an approximate solution to $\langle \boldsymbol{U}_2^{\text{cor}}\rangle$, as if the channel was composed of two vertical parallel plates, ignoring the no-slip on the horizontal boundaries, Eqs. (4.21a) and (4.21b). The idea is that the solution $\langle \boldsymbol{U}_2^{\text{plates}}\rangle + \langle \boldsymbol{U}_2^{\text{cor}}\rangle$ is a better solution to the rectangular channel, than just using $\langle \boldsymbol{U}_2^{\text{plates}}\rangle$. To solve $\langle \boldsymbol{U}_2^{\text{cor}}\rangle$ we furthermore have to approximate the boundary condition Eq. (4.21d) by a sine, $b\sin(2\pi y/h)$, making sure that the argument to the sine is chosen so that the sine is zero for $y = \pm h/2$. The expression for $\langle \boldsymbol{U}_2^{\text{cor}}\rangle$ is calculated using the approach for the high parallel-plates channel, yielding

$$\langle U_{2x}^{\text{cor}}\rangle = b\cos(2\pi y/h)\left\{C_1 2\pi\frac{x}{h}\cosh(2\pi x/h) + C_2\sinh(2\pi x/h)\right\}, \tag{4.22a}$$

$$\left\langle U_{2y}^{\text{cor}}\right\rangle = b\sin(2\pi y/h)\left\{C_3\cosh(2\pi x/h) + C_4 2\pi\frac{x}{h}\sinh(2\pi x/h)\right\}, \tag{4.22b}$$

where the coefficients b and the C's depend on α. The amplitude of the resulting velocity field, $\langle \boldsymbol{U}_2\rangle = \langle \boldsymbol{U}_2^{\text{plates}}\rangle + \langle \boldsymbol{U}_2^{\text{cor}}\rangle$, on the boundaries is shown in Figure 4.5. $\langle U_{2y}\rangle$ still has a small error on the side boundaries, given by $\langle U_{2y}^{\text{plates}}\rangle + \left\langle U_{2y}^{\text{cor}}\right\rangle$ in Figure 4.5 (a). Moreover, an error in $\langle U_{2x}\rangle$ has been introduced on the horizontal boundaries, given by $\langle U_{2x}^{\text{cor}}\rangle$ in Figure 4.5 (b). However, the magnitude of these errors are smaller than the initial error when considering only $\langle \boldsymbol{U}_2^{\text{plates}}\rangle$, given by $\langle U_{2y}^{\text{plates}}\rangle$ in Figure 4.5 (a). This give rise to the idea that we can assume an iterative approach, making another correction field, which corrects the present errors, and results in new but smaller errors. This approach rely on the magnitude of the error to converge towards zero with increasing numbers of iterations, which is not sure, but seems possible on the behalf of this first iteration. However, in order to eliminate the error completely we have to ensure that the first correction $\langle \boldsymbol{U}_2^{\text{cor}}\rangle$

eliminates the error made by $\langle \boldsymbol{U}_2^{\text{plates}} \rangle$ completely. This will be the topic of the next section.

4.3.2 Fourier expanded correction field

For $\langle \boldsymbol{U}_2^{\text{cor}} \rangle$ to eliminate the error made by $\langle \boldsymbol{U}_2^{\text{plates}} \rangle$ completely, a Fourier expansion of the boundary condition Eq. (4.21d) is made, instead of just approximating it with a single sine. The boundary condition for $\left\langle U_{2y}^{\text{cor}} \right\rangle$on the sides thus become

$$\left\langle U_{2y}^{\text{cor}} \right\rangle = \textstyle\sum_{n=1}^{\infty} b_n \sin\left(n2\pi y/h\right), \quad \text{for } kx = \pm\pi/2. \tag{4.23}$$

The Fourier coefficients are determined by the overlap integral

$$\begin{aligned} b_n = \frac{2}{h} \int_{y=-h/2}^{y=h/2} \mathrm{d}y\, u_{\text{str}} \Gamma(\alpha) \Big[& 2ky \cosh(2ky) \\ & - \alpha \coth(\alpha) \sinh(2ky) \Big] \sin\left(n2\pi y/h\right). \end{aligned} \tag{4.24}$$

The solution for $\langle \boldsymbol{U}_2^{\text{cor}} \rangle$ also becomes a sum of expressions, each having the form of Eq. (4.22)

$$\begin{aligned} \langle U_{2x}^{\text{cor}} \rangle = \sum_{n=1}^{\infty} b_n \cos\left(n2\pi y/h\right) \Big\{ & C_{1n} n2\pi \frac{x}{h} \cosh\left(n2\pi x/h\right) \\ & + C_{2n} \sinh\left(n2\pi x/h\right) \Big\}, \end{aligned} \tag{4.25a}$$

$$\begin{aligned} \left\langle U_{2y}^{\text{cor}} \right\rangle = \sum_{n=1}^{\infty} b_n \sin\left(n2\pi y/h\right) \Big\{ & C_{3n} \cosh\left(n2\pi x/h\right) \\ & + C_{4n} n2\pi \frac{x}{h} \sinh\left(n2\pi x/h\right) \Big\}. \end{aligned} \tag{4.25b}$$

The total velocity field $\langle \boldsymbol{U}_2 \rangle = \langle \boldsymbol{U}_2^{\text{plates}} \rangle + \langle \boldsymbol{U}_2^{\text{cor}} \rangle$, using the Fourier expansion of $\langle \boldsymbol{U}_2^{\text{cor}} \rangle$ given Eq. (4.25), fulfills the no-slip on the vertical boundaries completely, while having small error on the horizontal boundaries. We can now proceed by introducing another correction $\left\langle \boldsymbol{U}_2^{\text{cor},2} \right\rangle$ which corrects the error made by $\langle \boldsymbol{U}_2^{\text{plates}} \rangle + \langle \boldsymbol{U}_2^{\text{cor}} \rangle$ on the horizontal boundaries. $\left\langle \boldsymbol{U}_2^{\text{cor},2} \right\rangle$ will then in turn introduce a new error on the vertical boundaries, which is hopefully smaller than the error made by $\langle \boldsymbol{U}_2^{\text{plates}} \rangle$ alone on the vertical boundaries. This is the cycle of the iterative approach of correcting the solution for the parallel-plates channel $\langle \boldsymbol{U}_2^{\text{plates}} \rangle$ into fulfilling the constraints of the rectangular channel. The complete iterative approach, including many of these cycles, will be carried out in the next section.

4.3.3 Iterative Fourier expansion of the second-order velocity field

In this section the treatment of the rectangular channel is completed by a full iterative Fourier expansion of the time-averaged second-order bulk velocity field. The general idea is that several correction fields are introduced, each correcting the error of the former and introducing a new but smaller error.

$$\langle \boldsymbol{U}_2 \rangle = \sum_{m=1}^{\infty} \langle \boldsymbol{U}_2^m \rangle, \tag{4.26}$$

where $\langle \boldsymbol{U}_2^{m=1} \rangle$ corresponds to $\langle \boldsymbol{U}_2^{\text{plates}} \rangle$ and so forth. For clarity we non-dimensionalize the variables

$$\tilde{x} = 2kx, \tag{4.27a}$$
$$\tilde{y} = 2ky, \tag{4.27b}$$
$$\left\langle \tilde{\boldsymbol{U}}_2 \right\rangle = \langle \boldsymbol{U}_2 \rangle / u_{\text{str}}, \tag{4.27c}$$
$$\left\langle \tilde{\Psi}_2 \right\rangle = \langle \Psi_2 \rangle \, 2k/u_{\text{str}}. \tag{4.27d}$$

The second-order bulk fields are still governed by the set of equations(4.2) and we now guess for a stream function of the form

$$\begin{aligned}
\left\langle \tilde{\Psi}_2 \right\rangle = & \left[C_1^1 \sinh(\tilde{y}) + C_2^1 \tilde{y} \cosh(\tilde{y}) \right] \sin(\tilde{x}) \\
& + \sum_{n=1}^{\infty} \left[C_{1n}^2 \sinh\left(n\frac{\pi}{\alpha}\tilde{x} \right) + C_{2n}^2 n\frac{\pi}{\alpha}\tilde{x} \cosh\left(n\frac{\pi}{\alpha}\tilde{x} \right) \right] b_n^2 \sin\left(n\frac{\pi}{\alpha}\tilde{y} \right) \\
& + \sum_{n=1}^{\infty} \left[C_{1n}^3 \sinh(n\tilde{y}) + C_{2n}^3 n\tilde{y} \cosh(n\tilde{y}) \right] b_n^3 \sin(n\tilde{x}) \\
& + \sum_{n=1}^{\infty} \left[C_{1n}^4 \sinh\left(n\frac{\pi}{\alpha}\tilde{x} \right) + C_{2n}^4 n\frac{\pi}{\alpha}\tilde{x} \cosh\left(n\frac{\pi}{\alpha}\tilde{x} \right) \right] b_n^4 \sin\left(n\frac{\pi}{\alpha}\tilde{y} \right) \\
& + \ldots,
\end{aligned} \tag{4.28}$$

which can be expressed in the compact form

$$\begin{aligned}
\left\langle \tilde{\Psi}_2 \right\rangle &= \sum_{m=1}^{\infty} \left\langle \tilde{\Psi}_2^m \right\rangle \\
&= \sum_{m=1,m\,\text{odd}}^{\infty} \sum_{n=1}^{\infty} \left[C_{1n}^m \sinh(n\tilde{y}) + C_{2n}^m n\tilde{y} \cosh(n\tilde{y}) \right] b_n^m \sin(n\tilde{x}) \\
&+ \sum_{m=2,m\,\text{even}}^{\infty} \sum_{n=1}^{\infty} \left[C_{1n}^m \sinh\left(n\frac{\pi}{\alpha}\tilde{x} \right) + C_{2n}^m n\frac{\pi}{\alpha}\tilde{x} \cosh\left(n\frac{\pi}{\alpha}\tilde{x} \right) \right] b_n^m \sin\left(n\frac{\pi}{\alpha}\tilde{y} \right).
\end{aligned} \tag{4.29}$$

Following the definition of the stream function Eq. (3.37) the velocity field become

$$\begin{aligned}
\left\langle \tilde{U}_{2x} \right\rangle &= \sum_{m=1}^{\infty} \left\langle \tilde{U}_{2x}^{m} \right\rangle \\
&= \sum_{m=1,m\,\text{odd}}^{\infty} \sum_{n=1}^{\infty} \left[\left(C_{1n}^{m} + C_{2n}^{m} \right) n \cosh\left(n\tilde{y}\right) + C_{2n}^{m} n^2 \tilde{y} \sinh\left(n\tilde{y}\right) \right] b_n^m \sin\left(n\tilde{x}\right) \\
&\quad + \sum_{m=2,m\,\text{even}}^{\infty} \sum_{n=1}^{\infty} \left[C_{1n}^{m} n \frac{\pi}{\alpha} \sinh\left(n \frac{\pi}{\alpha} \tilde{x} \right) \right. \\
&\qquad \left. + C_{2n}^{m} \left(n \frac{\pi}{\alpha} \right)^2 \tilde{x} \cosh\left(n \frac{\pi}{\alpha} \tilde{x} \right) \right] b_n^m \cos\left(n \frac{\pi}{\alpha} \tilde{y} \right), \qquad (4.30a)
\end{aligned}$$

$$\begin{aligned}
\left\langle \tilde{U}_{2y} \right\rangle &= \sum_{m=1}^{\infty} \left\langle \tilde{U}_{2y}^{m} \right\rangle \\
&= -\sum_{m=1,m\,\text{odd}}^{\infty} \sum_{n=1}^{\infty} \left[C_{1n}^{m} n \sinh\left(n\tilde{y}\right) + C_{2n}^{m} n^2 \tilde{y} \cosh\left(n\tilde{y}\right) \right] b_n^m \cos\left(n\tilde{x}\right) \\
&\quad - \sum_{m=2,m\,\text{even}}^{\infty} \sum_{n=1}^{\infty} \left[\left(C_{1n}^{m} + C_{2n}^{m} \right) n \frac{\pi}{\alpha} \cosh\left(n \frac{\pi}{\alpha} \tilde{x} \right) \right. \\
&\qquad \left. + C_{2n}^{m} \left(n \frac{\pi}{\alpha} \right)^2 \tilde{x} \sinh\left(n \frac{\pi}{\alpha} \tilde{x} \right) \right] b_n^m \sin\left(n \frac{\pi}{\alpha} \tilde{y} \right). \qquad (4.30b)
\end{aligned}$$

Each of the terms $\langle \boldsymbol{U}_2^m \rangle$ is a combination of terms $\langle \boldsymbol{U}_2^{m,n} \rangle$, which all have the structure of the solution to a parallel-plates channel. Dependent on the parity of m, $\langle \boldsymbol{U}_2^{m,n} \rangle$ has the structure relating to horizontal plates, odd m, or vertical plates, even m. The value of n determines the number of half wavelength in the first-order resonance related to the solution $\langle \boldsymbol{U}_2^{m,n} \rangle$. The coefficients C_{1n}^m and C_{2n}^m relate only to the structure and not the magnitude of the individual solution $\langle \boldsymbol{U}_2^{m,n} \rangle$ and thus only depends on the number of periods n and whether the iteration number m is odd or even. The b_n^m coefficients sets the magnitude of the individual solutions $\langle \boldsymbol{U}_2^{m,n} \rangle$ and is determined by the form-coefficients and the magnitude of the previous iteration, C_{1n}^{m-1}, C_{2n}^{m-1} and b_n^{m-1}, hence depending on the values of both n and m. The first iteration, $m = 1$, corresponding to $\langle \boldsymbol{U}_2^{\text{plates}} \rangle$ is special in the way that only parameters for $n = 1$ are non-zero, and $b_1^1 = 1$.

Form coefficients, C_{1n}^m and C_{2n}^m

The even solutions (m even) correct an error on the vertical boundaries made by the previous odd solution, and the boundary conditions thus become

$$\left\langle \tilde{U}_{2x}^{m} \right\rangle \Big|_{\tilde{x}=\pm\pi} = 0, \qquad m \text{ even}, \qquad (4.31)$$

$$\left\langle \tilde{U}_{2y}^{m} \right\rangle \Big|_{\tilde{x}=\pm\pi} = -\left\langle \tilde{U}_{2y}^{m-1} \right\rangle \Big|_{\tilde{x}=\pm\pi}, \qquad m \text{ even}. \qquad (4.32)$$

The condition on $\langle U_{2x}^m \rangle$, Eq. (4.31), result in

$$C_{1n}^m \sinh\left(n\frac{\pi^2}{\alpha}\right) + C_{2n}^m n\frac{\pi^2}{\alpha}\cosh\left(n\frac{\pi^2}{\alpha}\right) \quad = \quad 0, \tag{4.33}$$

because all the harmonic functions are orthogonal.

Considering the condition on $\left\langle U_{2y}^m \right\rangle$, Eq. (4.32), result in

$$(C_{1n}^m + C_{2n}^m)\, n\frac{\pi}{\alpha}\cosh\left(n\frac{\pi^2}{\alpha}\right) + C_{2n}^m \left(n\frac{\pi}{\alpha}\right)^2 \pi \sinh\left(n\frac{\pi}{\alpha}\tilde{x}\right) \quad = \quad -1, \tag{4.34}$$

where we have used that by construction

$$\sum_{n=1}^{\infty} b_n^m \sin\left(n\frac{\pi}{\alpha}\tilde{y}\right) \quad = \quad -\left\langle \tilde{U}_{2y}^{m-1} \right\rangle\Big|_{\tilde{x}=\pm\pi}, \tag{4.35}$$

and thus the rest of the left hand side of Eq. (4.32) should be 1 for all n. Combining Eqs (4.33) and (4.34) yields the matrix equation

$$\begin{bmatrix} C_{1n} \\ C_{2n} \end{bmatrix} = \begin{bmatrix} \sinh\left(n\frac{\pi^2}{\alpha}\right) & n\frac{\pi^2}{\alpha}\cosh\left(n\frac{\pi^2}{\alpha}\right) \\ \cosh\left(n\frac{\pi^2}{\alpha}\right) & \cosh\left(n\frac{\pi^2}{\alpha}\right) + n\frac{\pi^2}{\alpha}\sinh\left(n\frac{\pi^2}{\alpha}\right) \end{bmatrix}^{-1} \begin{bmatrix} 0 \\ -\frac{\alpha}{n\pi} \end{bmatrix}, \qquad m \text{ even}. \tag{4.36}$$

Similarly the odd solutions correct an error on the horizontal walls made by the previous solution, and the boundary conditions thus become

$$\left\langle \tilde{U}_{2x}^m \right\rangle\Big|_{\tilde{y}=\pm\alpha} = -\left\langle \tilde{U}_{2x}^{m-1} \right\rangle\Big|_{\tilde{y}=\pm\alpha}, \qquad m \text{ odd}, \tag{4.37}$$

$$\left\langle \tilde{U}_{2y}^m \right\rangle\Big|_{\tilde{y}=\pm\alpha} = 0, \qquad m \text{ odd}, \tag{4.38}$$

leading to the matrix equation

$$\begin{bmatrix} C_{1n}^m \\ C_{2n}^m \end{bmatrix} = \begin{bmatrix} \sinh(n\alpha) & n\alpha\cosh(n\alpha) \\ \cosh(n\alpha) & \cosh(n\alpha) + n\alpha\sinh(n\alpha) \end{bmatrix}^{-1} \begin{bmatrix} 0 \\ \frac{1}{n} \end{bmatrix}, \qquad m \text{ odd}. \tag{4.39}$$

Through Eqs. (4.36) and (4.39) all form coefficients, C_{1n}^m and C_{2n}^m, can be determined.

Amplitude coefficients, b_n^m

The even solutions correct an error on the side boundaries and thus we have

$$\begin{aligned} \sum_{n=1}^{\infty} b_n^m \sin\left(n\frac{\pi}{\alpha}\tilde{y}\right) &= -\left\langle \tilde{U}_{2y}^{m-1} \right\rangle\Big|_{\tilde{x}=\pm\pi}, \qquad m \text{ even} \\ &= \sum_{q=1}^{\infty} \left[C_{1q}^{m-1} q \sinh(q\tilde{y}) + C_{2q}^{m-1} q^2 \tilde{y}\cosh(q\tilde{y}) \right] b_q^{m-1} \cos(q\tilde{x}) \Big|_{\tilde{x}=\pm\pi} \\ &= \sum_{q=1}^{\infty} \left[C_{1q}^{m-1} q \sinh(q\tilde{y}) + C_{2q}^{m-1} q^2 \tilde{y}\cosh(q\tilde{y}) \right] b_q^{m-1} (-1)^q, \end{aligned} \tag{4.40}$$

where the right hand side summation index has been substituted, $n \to q$, to distinguish the left and right summation indices. The Fourier coefficients are thus determined by

$$b_n^m = \frac{1}{\alpha}\int_{\tilde{y}=-\alpha}^{\tilde{y}=\alpha} \mathrm{d}\tilde{y}\Big\{ \sum_{q=1}^{\infty} \Big[C_{1q}^{m-1} q \sinh(q\tilde{y}) + C_{2q}^{m-1} q^2 \tilde{y} \cosh(q\tilde{y}) \Big] b_q^{m-1} (-1)^q \Big\} \sin\left(n\frac{\pi}{\alpha}\tilde{y}\right), m \text{ even}. \tag{4.41}$$

To proceed with this expression we need to calculate the Fourier expansion of $\sinh(q\tilde{y})$ and $\tilde{y}\cosh(q\tilde{y})$. We consider the general Fourier expansion

$$\sum_{l=1}^{\infty} a_l \sin(l\xi) = D_1 \sinh(s\xi) + D_2 sz \cosh(s\xi), \tag{4.42}$$

where l is the summation index, a_l are the Fourier expansion coefficients, ξ is a variable running from $-\pi$ to π in the region of interest, and D_1, D_2, and s are constants. From tables of Fourier series this expansion has the coefficients

$$\begin{aligned} a_l = {} & D_1 \frac{2\sinh(s\pi)}{\pi}(-1)^{(l-1)} \frac{l}{l^2+s^2} \\ & + D_2 (-1)^l \frac{2s}{\pi(s^2+l^2)^2} \Big\{ \Big[\Big(s^2 - l^2\Big) l\pi - 2\pi l s^2 \Big] \cosh(\pi s) + 2ls \sinh(\pi s) \Big\}. \end{aligned} \tag{4.43}$$

Comparing the right hand sides of Eq. (4.40) and Eq. (4.42) the following translation can be made

$$\xi = \frac{\pi}{\alpha}\tilde{y}, \qquad m \text{ even}, \tag{4.44a}$$

$$s = \frac{q\alpha}{\pi}, \qquad m \text{ even}, \tag{4.44b}$$

$$D_1 = b_q^{m-1}(-1)^q C_{1q}^{m-1} q, \qquad m \text{ even}, \tag{4.44c}$$

$$D_2 = b_q^{m-1}(-1)^q C_{2q}^{m-1} q. \qquad m \text{ even}. \tag{4.44d}$$

Inserting the expansion Eq. (4.42) into the expression for the even amplitude coefficients Eq. (4.41) yields

$$b_n^m = \frac{1}{\alpha}\int_{\tilde{y}=-\alpha}^{\tilde{y}=\alpha} \mathrm{d}\tilde{y}\Big\{ \sum_{q=1}^{\infty}\sum_{l=1}^{\infty} a_l \sin(l\frac{\pi}{\alpha}\tilde{y}) \Big\} \sin\left(n\frac{\pi}{\alpha}\tilde{y}\right), \quad m \text{ even}, \tag{4.45}$$

where we have substituted the variable ξ using Eq. (4.44a). Because the sines are orthogonal for $l \neq n$, the integration of the sines are non-zero only for $l = n$ and the expression Eq. (4.45) reduces to

$$b_n^m = \sum_{q=1}^{\infty} a_n, \tag{4.46}$$

recalling that a_n indeed depends on both q and m expressed through Eqs. (4.43) and (4.44). Inserting Eq. (4.43) into Eq. (4.46) we arrive at the final expressions for the amplitude coefficients to the even solution

$$\begin{aligned} b_n^m &= \sum_{q=1}^{\infty} D_1 \frac{2\sinh(s\pi)}{\pi}(-1)^{(n-1)}\frac{n}{n^2+s^2} \\ &\quad + D_2(-1)^n \frac{2s}{\pi(s^2+n^2)^2}\Big\{\Big[\left(s^2-n^2\right)n\pi - 2\pi n s^2\Big]\cosh(\pi s) \\ &\qquad + 2ns\sinh(\pi s)\Big\}, \end{aligned} \tag{4.47}$$

where D_1, D_2 and s are given by Eq. (4.44).

For the odd solutions we have

$$\begin{aligned} \sum_{n=1}^{\infty} b_n^m \sin(n\tilde{x}) &= -\left\langle \tilde{U}_{2x}^{m-1}\right\rangle\Big|_{\tilde{y}=\pm\alpha}, \qquad m\,\text{odd}, \\ &= -\sum_{q=1}^{\infty}\Big[C_{1q}^{m-1} q\frac{\pi}{\alpha}\sinh\left(q\frac{\pi}{\alpha}\tilde{x}\right) \\ &\qquad + C_{2q}^{m-1}\left(q\frac{\pi}{\alpha}\right)^2\tilde{x}\cosh\left(q\frac{\pi}{\alpha}\tilde{x}\right)\Big] b_q^{m-1}\cos\left(q\frac{\pi}{\alpha}\tilde{y}\right)\Big|_{\tilde{y}=\pm\alpha} \\ &= \sum_{q=1}^{\infty}\Big[C_{1q}^{m-1} q\frac{\pi}{\alpha}\sinh\left(q\frac{\pi}{\alpha}\tilde{x}\right) \\ &\qquad + C_{2q}^{m-1}\left(q\frac{\pi}{\alpha}\right)^2\tilde{x}\cosh\left(q\frac{\pi}{\alpha}\tilde{x}\right)\Big] b_q^{m-1}(-1)^{q-1}, \end{aligned} \tag{4.48}$$

and following the same procedure as for the even solutions we end up with the same expression for b_n^m Eq. (4.47), but with D_1, D_2 and s given by

$$s = \frac{q\pi}{\alpha}, \qquad m\,\text{odd}, \tag{4.49a}$$

$$D_1 = b_q^{m-1}(-1)^{q-1} C_{1q}^{m-1} q\frac{\pi}{\alpha}, \qquad m\,\text{odd}, \tag{4.49b}$$

$$D_2 = b_q^{m-1}(-1)^{q-1} C_{2q}^{m-1} q\frac{\pi}{\alpha}, \qquad m\,\text{odd}. \tag{4.49c}$$

This completes the treatment of the coefficients of the iterative expansion of the second-order velocity field $\langle \boldsymbol{U}_2\rangle$ Eq. (4.30).

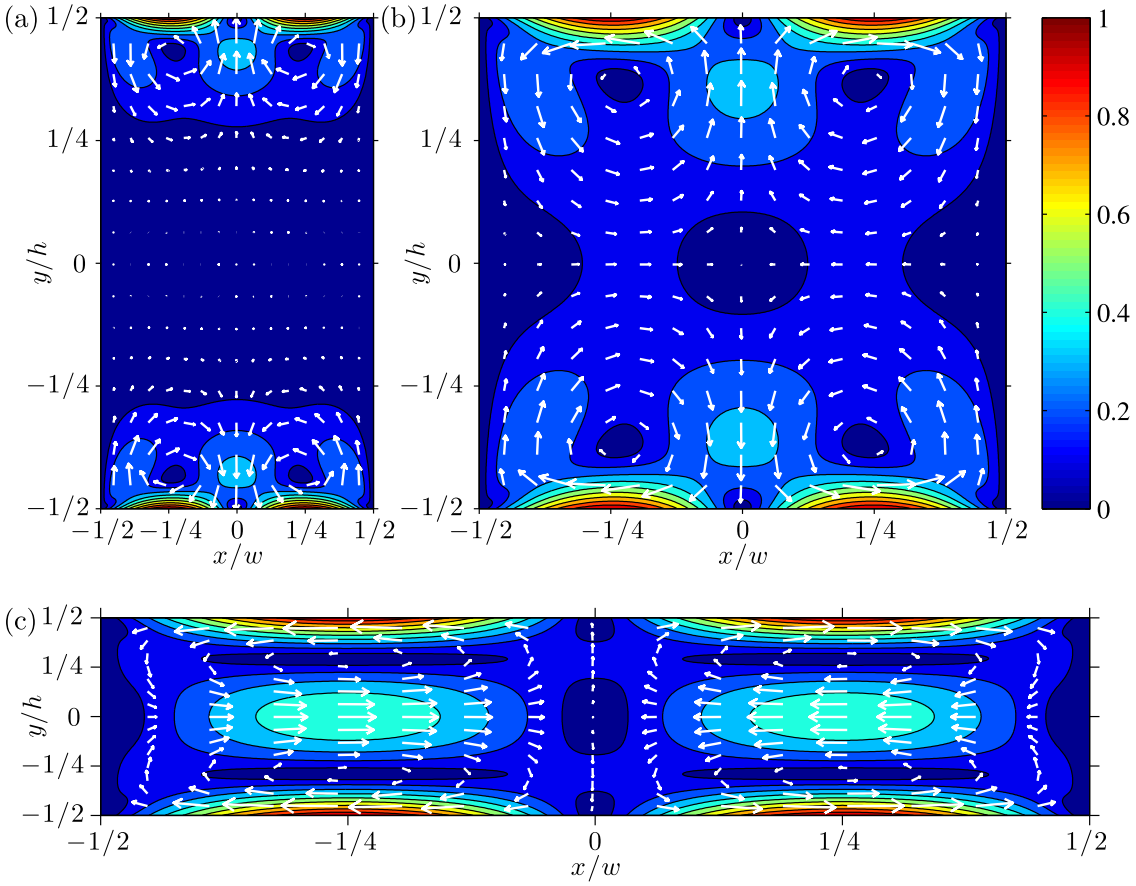

Figure 4.6: Color and vector plot of the time-average second-order velocity field, $\langle \boldsymbol{U}_2 \rangle$, of a rectangular channel using an iterative Fourier expansion. The velocity field is normalized to u_{str} and shown for aspect ratios of (a) $h/w = 2$, (b) $h/w = 1$, and (c) $h/w = 1/5$. The calculations include $M = 20$ iterations, each with $N = 40$ Fourier components. The velocity is now zero at the vertical boundaries, and further from the sides it is altered slightly compared to the solutions for the high parallel-plates channel in Figure 4.2. Due to this alteration, the velocity field is no longer symmetric about the vertical lines at $x/w = \pm 1/4$. The inclusion of the no-slip condition on the side walls has a less pronounced effect on the structure of the velocity field for the low aspect ratio, (c).

4.3.4 Result of the iterative Fourier expansion

As we have now determined all the coefficients of the iterative Fourier expansion of $\langle \boldsymbol{U}_2 \rangle$ Eq. (4.30), the time-averaged second-order bulk velocity field of the rectangular channel can now be visualized. This is done in Figure 4.6 for $\alpha = \pi/2$. When plotting $\langle \boldsymbol{U}_2 \rangle$ we have to choose a limit for the infinite sums of the expansion Eq. (4.30), and the field shown in Figure 4.6 is based on $M = 20$ iterations and $N = 40$ Fourier components in each iteration. Moreover, we generally set the number of Fourier components in the sum over q in Eq. (4.47) equal to N as well. The magnitude of the error made by $\langle \boldsymbol{U}_2 \rangle$ on the boundaries are of order $u_{\text{str}} 10^{-3}$. Figure 4.6 shows how the velocity now decay to zero on

the vertical boundaries. The velocity field further from the boundaries has been distorted slightly compared to the velocity field of the high parallel-plates channels in Figure 4.2. The overall structure of the streaming velocity field remains the same.

In the calculations of the velocity field shown in Figure 4.6 a large number of iterations and Fourier components have been included, $M = 20$ and $N = 40$. In some situations it is desirable to include fewer iterations and component to reduce the complexity of the expression. To quantify the error made by such expressions the root mean square deviation, σ_{rms}, is defined as

$$\sigma_{\text{rms}} \equiv \frac{\left|\left|\langle \boldsymbol{U}_2 \rangle - \left\langle \boldsymbol{U}_2^{\text{ref}} \right\rangle\right|\right|}{\left|\left|\left\langle \boldsymbol{U}_2^{\text{ref}} \right\rangle\right|\right|} = \sqrt{\frac{\int_\Omega \mathrm{d}A \left(\langle \boldsymbol{U}_2 \rangle - \left\langle \boldsymbol{U}_2^{\text{ref}} \right\rangle\right)^2}{\int_\Omega \mathrm{d}A \left\langle \boldsymbol{U}_2^{\text{ref}} \right\rangle^2}}, \tag{4.50}$$

where the integration area Ω is the channel cross section and $\left\langle \boldsymbol{U}_2^{\text{ref}} \right\rangle$ is a reference field. In this thesis the reference field is calculated using $M = 20$ and $N = 40$. Figure 4.7 shows σ_{rms} as a function of M with curves for different values of N. To understand these curves we elaborate a bit on the way this iterative approach works. Each iterations corrects an error on one set of boundaries, denoted its *correction boundaries*, made by the previous iteration. Moreover, it introduces an error on the other set of boundaries, denoted its *error boundaries*. The value of N is determining for how well each iteration corrects the error on its correction boundaries. Over several iterations small errors are accumulated, made by each iteration on its correction boundaries due to the finite value of N. Each iteration only corrects the error made by the previous iteration, it does not correct the accumulated error of all the previous iterations. Consequently, at some point the error made by a single iteration becomes negligible compared to the accumulated error, and further iterations does not increase the accuracy of the solution. This is seen in Figure 4.7 as the flattening of the curves. As the number of Fourier components N is increased it becomes reasonable to include more iterations. When not limited by the number of Fourier components, the error σ_{rms} decay exponentially with increasing iterations, shown by the straight line in the semi-log graph. This confirms that the iterative Fourier approach converges well for both square and rectangular channels.

The initial error is low in Figure 4.7 (b), due to the low aspect ratio. The first corrective iteration, $M = 2$, decrease the error significantly, even with a single Fourier component. This is because the error in $\langle U_{2y} \rangle$ on the vertical boundaries is well approximated by a sine, as seen in Figure 4.3 (b). The second corrective iteration, $M = 3$, needs to correct an exponentially decaying error, similar to the graph for $h/w = 2$ in Figure 4.3 (b). This requires several Fourier components in order to resolve the error sufficiently, and as seen in the Figure 4.7 (b), as only for $N = 5$ or higher does the iteration $M = 3$ decrease σ_{rms}. For the square channel, Figure 4.7 (a) the effective aspect ratio is the same for each corrective iteration, and thus the errors are more efficiently corrected with fewer Fourier components. Consequently, we conclude that the iterative Fourier expansion approach corrects the error most efficiently when the aspect ratio is close to unity. However, in general the error can be decreases to an arbitrary value, no matter the aspect ratio, if the number of iterations and Fourier components are not limited.

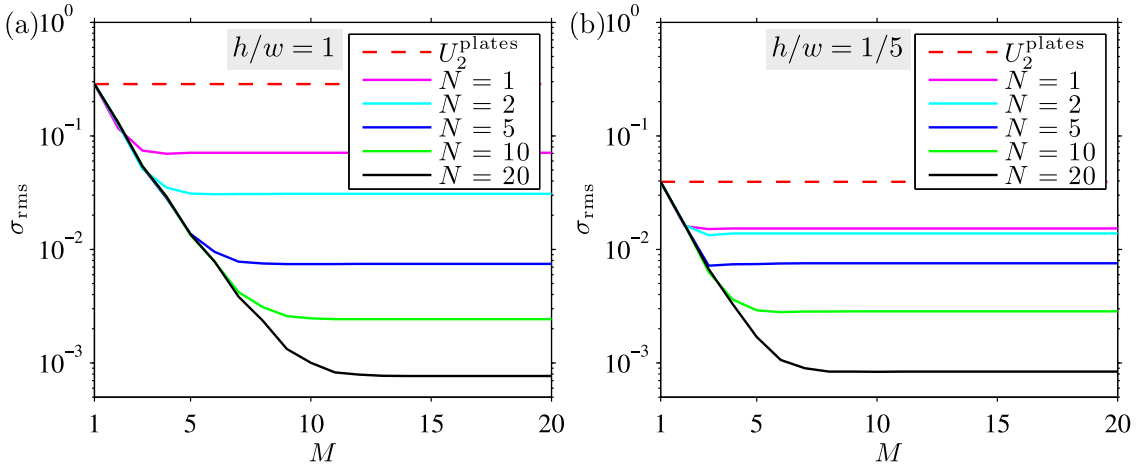

Figure 4.7: Semi-log plot of the global error, defined by the root mean square deviation σ_{rms}, Eq. (4.50), for the iterative Fourier expansion solution Eq. (4.30), versus the number of iterations M, with curves for different numbers of Fourier components N. The aspect ratio of the channel is (a) $h/w = 1$ and (b) $h/w = 1/5$.When increasing the number of iterations, for a fixed value of N, a point is reached where the accumulated error is greater than the error made by the last iteration. Consequently, σ_{rms} does not decrease with further iterations as each iteration only corrects the error made by the previous iteration and not the accumulated error. This is seen as the flattening of the curves. Increasing the number of Fourier components enables a further decrease of σ_{rms} with more iterations. When not limited by the number of Fourier components the error σ_{rms} decay exponentially with increasing iterations. This confirms, that the iterative Fourier approach converges well for both square and rectangular channels.

We now turn to consider the effect of the rectangular solution on the structure of the rotational flow, expressed through the parameters d_{min}, d_{rc}, and $U_{2x,\text{min}}$. Figure 4.8 shows the values of d_{min}, d_{rc}, and $U_{2x,\text{min}}$ versus the aspect ratio h/w, with blue lines for the result of the parallel-plates solution and red lines for the rectangular channel solution. From d_{min} in Figure 4.8 (a) it is seen that the local minima in $\langle U_{2x} \rangle$ starts to move away from the center for a lower value of h/w compared to the plates solution. Moreover, both d_{min} and d_{rc} level at a lower value compared to the plates solution. These effects are a result of the flow roll being retarded by the no-slip of the side walls. This result in a faster decay of the velocity of each roll towards the center. The development of the $U_{2x,\text{min}}$ shown in Figure 4.8 (b) is very similar to that of the plates solution. The earlier decay corresponds to the earlier kink of d_{min}, while the leveling at a slightly larger value is ascribed to the detailed structure of the flow roll.

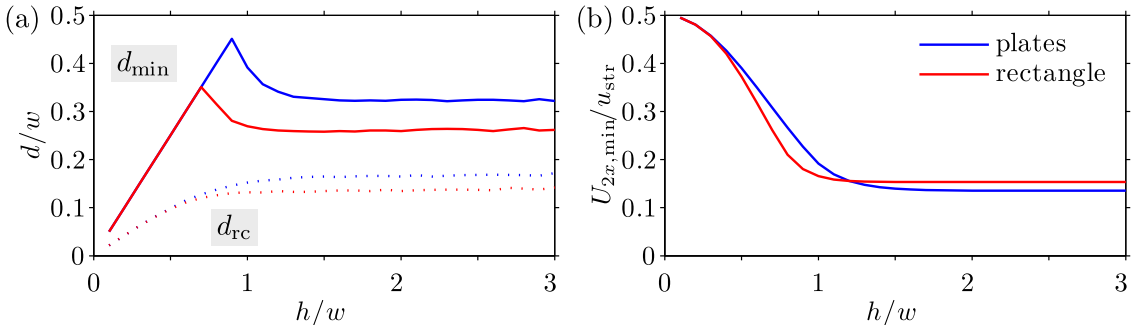

Figure 4.8: Graphs of the structural parameters $d_{\min}$, $d_{\rm rc}$, and $U_{2x,\min}$ versus the aspect ratio h/w. The blue lines show the values of the parallel-plates solution, while the red lines show the values of the rectangular channel solution. The kink in $d_{\min}$, indicating that the minimum in $\langle U_{2x}\rangle$ moves away from the center, happens at a lower value for the rectangular solution. Moreover, $d_{\min}$ and $d_{\rm rc}$ both level at a lower value for high h/w compared to the plates solution. $U_{2x,\min}$ decay faster in agreement with the earlier kink of $d_{\min}$, while leveling at a slightly larger value. These effects are ascribed to the retardation of the flow rolls by the side walls.

4.3.5 Approximate velocity field

In this section an approximate solution to acoustic streaming in the rectangular channel is proposed. The motivation is to achieve a less complicated expression compared to the iterative Fourier approach. The solution to the parallel-plates channel in once again used as a starting point. Since the parallel-plates solution does not fulfill the no-slip condition on the side wall, it is multiplied by and envelope function, making to solution go to zero on the vertical boundaries. This envelope $g(x)$ can be designed in many ways, where in this case a cosine hyperbolic envelope is chosen,

$$g(x) = 1 - \left[\frac{\cosh\left(\frac{x}{\Delta}\right)}{\cosh\left(\frac{w}{2\Delta}\right)}\right]. \tag{4.51}$$

This envelope ensures that $g(\pm w/2) = 0$, as well as $g(0) \approx 1$ for practical values of Δ. The envelope $g(x)$ is shown in Figure 4.9 for different values of Δ. As shown by the curves in Figure 4.9, Δ sets the decay length of the envelope.

This approximate velocity field, using the envelope function $g(x)$, is denoted $\left\langle \boldsymbol{U}_2^{\Delta}\right\rangle$, and is given by

$$\left\langle \boldsymbol{U}_2^{\Delta}\right\rangle = \langle \boldsymbol{U}_2^{\rm plates}\rangle \left\{1 - \left[\frac{\cosh\left(\frac{x}{\Delta}\right)}{\cosh\left(\frac{w}{2\Delta}\right)}\right]\right\}, \tag{4.52}$$

where $\langle \boldsymbol{U}_2^{\rm plates}\rangle$ is given by Eq. (4.15). For $\left\langle \boldsymbol{U}_2^{\Delta}\right\rangle$ to be accurate, the value of Δ should be optimized for each value of h/w. This is done by considering the deviation $\sigma_{\rm rms}$ Eq. (4.50) of $\left\langle \boldsymbol{U}_2^{\Delta}\right\rangle$ with respect to the reference field from the iterative Fourier solution. Figure 4.10 (a) shows $\sigma_{\rm rms}$ for $\left\langle \boldsymbol{U}_2^{\Delta}\right\rangle$ as function of Δ. The error for the parallel-plates

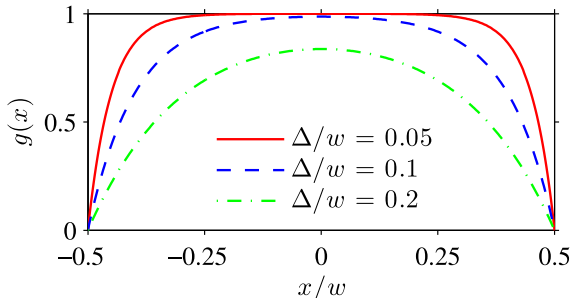

Figure 4.9: Graph of the envelope function $g(x)$ given by Eq. (4.51), used in the approximate solution $\langle \boldsymbol{U}_2^{\Delta} \rangle$ to the rectangular channel. The different curves correspond to different values of the parameter Δ, which determines the shape of the envelope. It is seen how the value of Δ sets the decay length of the envelope. In order for $\langle \boldsymbol{U}_2^{\Delta} \rangle$ to be a good approximation, the value of Δ needs to be optimized for each aspect ratio.

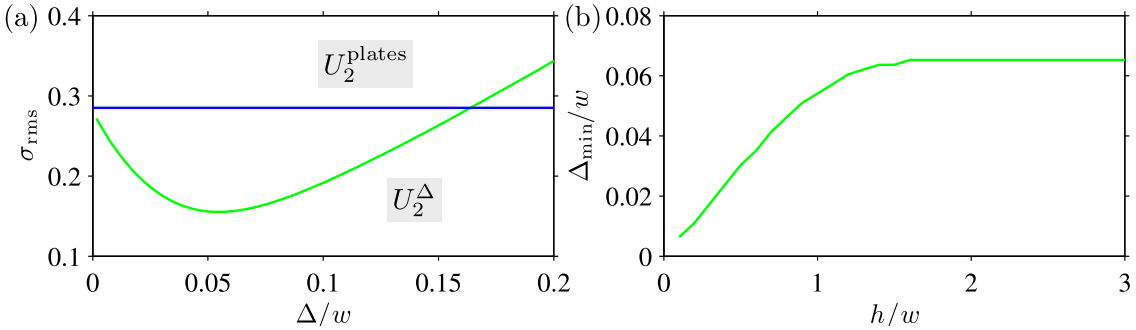

Figure 4.10: (a) The root mean square deviation, σ_{rms}, of the approximate envelope solution, $\langle \boldsymbol{U}_2^{\Delta} \rangle$, with respect to the iterative Fourier solution. The error is plotted versus the envelope parameter Δ, and calculated for a square channel, $h/w = 1$. The expression for $\langle \boldsymbol{U}_2^{\Delta} \rangle$ is given by Eq. (4.52), and the error for the parallel-plates solution $\langle \boldsymbol{U}_2^{\mathrm{plates}} \rangle$ is shown as a reference. For low values of Δ the error of $\langle \boldsymbol{U}_2^{\Delta} \rangle$ becomes the same as for $\langle \boldsymbol{U}_2^{\mathrm{plates}} \rangle$, because the envelope becomes very steep. For high values of Δ the error for $\langle \boldsymbol{U}_2^{\Delta} \rangle$ becomes even larger than for $\langle \boldsymbol{U}_2^{\mathrm{plates}} \rangle$, as the envelope alters the field in the center of the channel too much. A local minimum is found at $\Delta = \Delta_{\mathrm{min}}$, where the envelope solution best approximates the iterative Fourier solution. (b) Graph showing the dependence of Δ_{min} on the aspect ratio h/w of the channel. For low aspect ratios Δ_{min} scales linearly with the height. Since the vertical velocities also scales linearly with the height, for low h/w, it is concluded that Δ_{min} scales linearly with the vertical velocity. For large aspect ratios Δ_{min} level, as the structure of the flow becomes independent of the height.

solution $\langle \boldsymbol{U}_2^{\mathrm{plates}} \rangle$ is shown as a reference. For very small values of Δ, the envelope $g(x)$ becomes so steep that the error of $\left\langle \boldsymbol{U}_2^{\Delta} \right\rangle$ becomes the same as that of $\langle \boldsymbol{U}_2^{\mathrm{plates}} \rangle$. For large values of Δ, the envelope becomes too flat and alters the solution far from the sides so that the error of $\left\langle \boldsymbol{U}_2^{\Delta} \right\rangle$ becomes larger than that of $\langle \boldsymbol{U}_2^{\mathrm{plates}} \rangle$. Consequently, a minimum is found in between these too extremes, which determines the beta value resulting in the lowest error, denoted Δ_{min}. The dependence of Δ_{min} on the aspect ratio h/w is shown in Figure (4.10) (b). Δ_{min} is a measure of the viscous decay length of the flow at the

side walls. The vertical flow velocities scales linearly with h/w for low aspect ratios, according to the thin parallel-plates solution Eq. (4.7). The linear regime for low values of h/w in Figure (4.10) (b) thus indicates that $\Delta_{\min}$ scales linearly with the vertical flow velocity. This conclusion is used in the later analysis of the deviation of envelope solution. For large aspect ratios the structure of the flow becomes independent of the height, and consequently $\Delta_{\min}$ does as well.

The error of the approximate envelope solution $\left\langle \boldsymbol{U}_2^{\Delta} \right\rangle$ is shown in Figure 4.11 (a) versus the aspect ratio of the channel, where Δ has been optimized for each value of h/w. The error of the parallel-plates solution $\langle \boldsymbol{U}_2^{\text{plates}} \rangle$ is shown as a reference. For low aspect ratios the error scales linearly with h/w, simply because the relative size of the domain, influenced by the no-slip boundary condition at the side walls, scales linearly with h/w. For larger aspect ratios, the point is reached where the structure of the flow rolls no longer depends on the height of the channel, and consequently the error of both $\left\langle \boldsymbol{U}_2^{\Delta} \right\rangle$ and $\langle \boldsymbol{U}_2^{\text{plates}} \rangle$ level out.

Figure 4.11 (b) shows the ratio of the errors made by the approximate envelope solution and the parallel-plates solution. The error made by the parallel-plates solution is most effectively corrected, by the multiplication of the envelope, when the aspect ratio is low. When the aspect ratio increases, the inhomogeneity of the velocity field increases as well, due to the decay of the flow rolls towards the center. As the amplitude of the vertical velocity, in the vicinity of the side walls, changes significantly from the bottom to the center, it becomes difficult to correct the parallel-plates solution with an envelope, which is invariant in the y-direction. In order to obtain a better approximate solution for larger

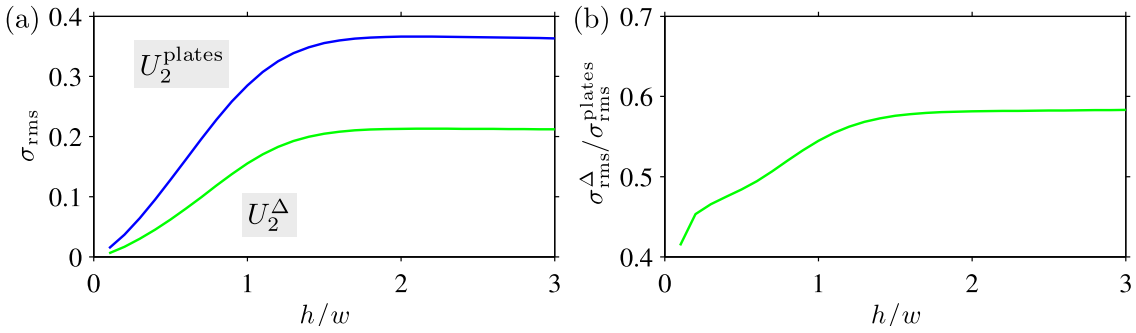

Figure 4.11: (a) The error made by the approximate envelope solution and the parallel-plates solution versus the aspect ratio of the rectangular channel. The value of Δ has been optimized for each value of h/w. The error decreases for decreasing h/w, as a consequence of the decreasing relative size of the area affected by the side wall. For larger aspect ratios the structure of the flow becomes independent of h/w, and thus the error level. (b) The error made by the approximate envelope solution relative to the error made by the parallel-plates solution versus h/w. The error made by the parallel-plates solution is most effectively corrected by the envelope in the case of low aspect ratios. For large aspect ratios the amplitude of the velocity field becomes more inhomogeneous in the y-direction, and the correction using the y-independent envelope becomes less efficient. The approximate envelope solution could be further improved by making Δ y-dependent.

aspect ratios, a two-dimensional envelope function could be used,

$$g(x,y) = 1 - \left[\frac{\cosh\left(\frac{x}{\Delta(y)}\right)}{\cosh\left(\frac{w}{2\Delta(y)}\right)} \right], \tag{4.53}$$

whereΔ is now a function of y. According to the analysis of Figure 4.10 (b), $\Delta_{\min}$ scales linearly with the amplitude of the vertical velocities, and thus $\Delta(y)$ should have the y-dependence of $\langle U_{2y}^{\text{plates}} \rangle$. This expansion of the approximate envelope solution for the rectangular channel is not pursued further in this thesis.

4.4 Concluding remarks

We have derived solutions for the acoustic streaming in parallel-plates channels in agreement with the results of Rayleigh [1]. We have performed thorough study of the solution for the high parallel-plates channel, for which the distance between the plates is comparable to the acoustic wavelength. We have defined three structural parameters, by which the acoustic streaming velocity field can be characterized; (i) the distance from the wall to the rotation center of the bulk streaming rolls, d_{rc}, (ii) the distance from the wall to the local minima of the horizontal streaming velocity, $d_{\min}$, and (iii) the value of the horizontal streaming velocity at this minimum, $U_{2x}^{\min}$. We have also treated the acoustic streaming in rectangular microchannels, which are commonly used in acoustofluidics. We have proposed an iterative Fourier approach, in which the velocity field is expanded into an infinite series, in order to fulfill the no-slip boundary condition on the side walls. The iterative solution converges well and solves the acoustic streaming in a rectangular channel to arbitrary high precision, by including sufficient iterations and Fourier components. This allows for prediction of the acoustic streaming in experimental acoustofluidic devices, and can thus be used in future comparison of theory and experiments.

In order to obtain a simpler expression for the acoustic streaming velocity field in the rectangular channel, we have proposed an approximate analytical solution composed of the high parallel-plates solution multiplied by an envelope function, ensuring the fulfillment of the no-slip condition on the side walls. The root mean square deviation of the envelope solution, with respect to the iterative Fourier solution, was approximately half that of the parallel-plates solution.

This concludes the analytical treatment of the acoustic streaming in microfluidic channels. In the following chapters we touch upon numerical simulations and experimental measurements of the acoustic streaming. By comparing both analytical, numerical and experimental results, we are able to verify and assess the embedded assumption and approximation in all of the three methods.

Chapter 5

Numerical simulations

In order to validate the analytical results and to describe acoustic streaming in more complicated structures we employ numerical simulations of acoustic streaming. This is done using the commercial software Comsol Multiphysics Version 4.2a (Comsol), which solves partial differential equations (PDEs) using the finite element method [64]. Comsol uses a graphical user interface (GUI) in which the user can choose predefined physical problems or write the PDEs from scratch. In this work the predefined physical problems have been used as a starting point for our numerical models, from which we have manually edited the equations to match those of the basic acoustofluidic theory presented in Chapter 2. As an alternative to using the GUI, Comsol also supports scripting in Matlab. For the present work scripting in Matlab has only been used for postprocessing of the numerical results, while a thorough description of scripting the numerical model in Matlab can be found in Skafte-Pedersen [59] and Barnkob [61].

In this chapter we will first describe the representation of the governing equations in Comsol and afterwards discuss the different ways to model acoustic streaming in microfluidic channels. The first-order problem is solved in the frequency domain, utilizing the harmonic time dependence of the first-order fields, while the second-order problem is solved using a time-independent solver. The tendencies of the numerical solution for the acoustic streaming is in agreement with the analytical solution, though with deviations close to the boundaries. We identify a possible error in the first-order frequency domain simulations and suggest a time-dependent simulation of the first-order fields in order to allow for comparison. Finally, we validate the iterative Fourier approach for acoustic streaming in a rectangular channel, using a numerical model based on the analytical acoustic streaming boundary condition for the second-order bulk velocity field.

In Section 5.4 we comment on how the first-order frequency domain simulations should be improved in the future work, as a consequence of the revised analytical first-order theory described in Section 3.6.1. Preliminary results of this revised first-order frequency domain model is presented.

5.1 Equation representation

In Comsol the governing PDEs can be represented in three ways; on coefficient form, general form, or weak form. Here we use the general form, as we find this to be the most intuitive. The PDE for the m-variable in the general form writes

$$d_{a_m}\frac{\partial u_m}{\partial t} + \boldsymbol{\nabla}\cdot\boldsymbol{\Gamma}_m = f_m, \quad \text{for } (x,y,x)\in\Omega, \tag{5.1}$$

where u_m is the dependent variable, $\boldsymbol{\Gamma}_m$ is the flux vector, f_m is the source density, and d_{a_m} is a coefficient [64]. Ω represents the domain in which the PDE is defined. The bulk equation (5.1) is constrained on the boundaries of the domain by the two conditions

$$R_m = 0, \qquad \text{for } (x,y,x)\in\partial\Omega, \tag{5.2a}$$

$$-\boldsymbol{n}\cdot\boldsymbol{\Gamma}_m = G_m + \mu_m\frac{\partial R_m}{\partial u_m}, \qquad \text{for } (x,y,x)\in\partial\Omega, \tag{5.2b}$$

where $\boldsymbol{n}$ is an outward pointing normal vector on the boundary $\partial\Omega$, and μ_m is a Lagrange element for the n'th boundary element. Eq. (5.2a) is a Dirichlet boundary condition, while Eq. (5.2b) is a Neumann boundary condition.

5.1.1 The first-order Navier–Stokes equation on general form

As an example we show the general form of the 2D first-order Navier–Stokes equation for the incompressible boundary field $\boldsymbol{u}_1$, given by Eq. (2.42a). There are two dependent variables u_{1x} and u_{1y}, and the flux vectors and source densities become

$$\boldsymbol{\Gamma}_{u_{1x}} \equiv \begin{bmatrix}\partial_x u_{1x}\\ \partial_y u_{1x}\end{bmatrix}, \quad f_{u_{1x}} \equiv \kappa^2 u_{1x}, \tag{5.3a}$$

$$\boldsymbol{\Gamma}_{u_{1y}} \equiv \begin{bmatrix}\partial_x u_{1y}\\ \partial_y u_{1y}\end{bmatrix}, \quad f_{u_{1y}} \equiv \kappa^2 u_{1y}. \tag{5.3b}$$

5.2 Numerical modeling of the acoustic streaming

Ideally, the numerical models should resemble the physical experiment as much as possible and be independent of the assumptions made in the analytical derivation. However, we are challenged by the huge difference in timescales between the dominant time-dependent component of the velocity field and the small steady component. The time-dependent component vary on a timescale of sub microseconds, corresponding to the MHz frequencies. The steady component is generated in the boundary layer, and the full acoustic streaming velocity field is established by convection and diffusion of momentum into the bulk, which happens on a time scale of seconds. A full time-dependent solution would

thus require millions of time steps. In order to work around this problem we employ the perturbation scheme in the numerical simulation as well. Consequently, we need to make sure that the amplitude of the velocity field is small enough for the perturbation assumption to be valid.

In order to calculate the time-averaged second-order velocity field we need the amplitudes and the phases of the first-order fields, as described by the time-averaged second-order Navier–Stokes equation (2.38). In Section 5.3 we solve the first-order equations in the frequency domain, assuming harmonic time dependence of all first-order fields. From this frequency domain model we obtain the spatial dependent complex amplitudes of the first-order fields, which are then used in a time-independent model for the time-averaged second-order fields in Section 5.5. An important issue of the numerical simulations is the number of elements needed to resolve the physical fields inside the boundary layer. This will be thoroughly considered through convergence analysis of the numerical solution in Section 5.3.1. The order of the basis functions is second-order for the velocity fields and first order for the pressure fields.

5.3 First-order problem

The first-order field is solved in the frequency domain, assuming harmonic time dependence of all fields. The simulation assumes an ideal horizontal half-wave resonance as shown in Figure 5.1. The domain of the numerical model is based on a quadratic channel cross section, in which the symmetry around the horizontal center line has been exploited. The physical dimensions of the channel is $h = w = 750\,\mu\text{m}$, corresponding to a frequency of 1 MHz. In the analysis of the numerical solution of the first-order problem presented here, the boundary layer thickness is increased by a factor of 25, in order to reduce computational time, by setting the dynamic viscosity η_{num} in the simulation to $\eta_{\text{num}} = 25^2\eta_{\text{water}}$. We use a first-order solution obtained for the physical value of the boundary layer thickness when considering the second-order problem in Section 5.5. The boundary layer thickness in the first-order model is thus $\delta \approx 0.02h$. The calculated first-order velocity field is shown in Figure 5.2.

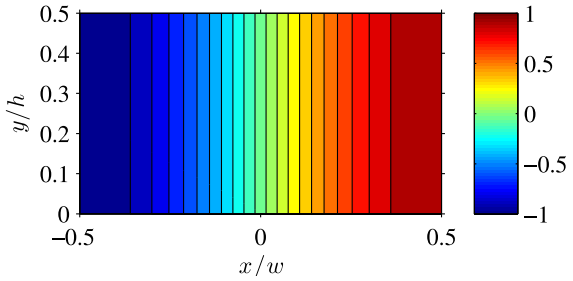

Figure 5.1: Color plot of the first-order density variation, ρ_1, normalized to its amplitude $\rho_0 \frac{u_0}{c}$. The numerical domain in based on a quadratic channel, in which symmetry about the horizontal center line has been exploited. The numerical simulations assume an ideal pressure resonance.

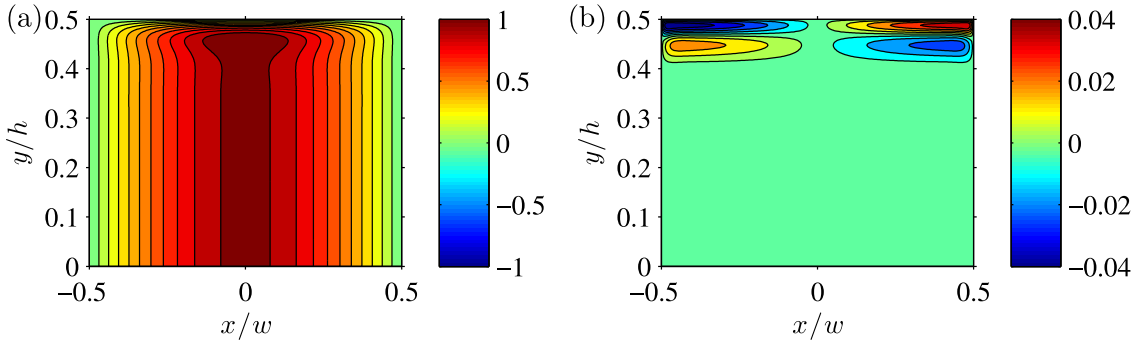

Figure 5.2: Color plot of the numerical solution for the first-order velocity field. (a) v_{1x} normalized to u_0. Far from the wall v_{1x} is independent of y, while close to the wall at $y/h = 0.5$ it decays on a length scale of $\delta = 0.02h$. (b) v_{1y} normalized to $u_0 k\delta$. The magnitude of v_{1y} is significant only close to the wall at $y/h = 0.5$.

5.3.1 Mesh convergence

In order to determine whether the boundary layer has been resolved with a sufficient number of mesh elements we perform a convergence analysis, in which we solve the problem with increasingly smaller mesh elements and see when the solution does no longer change. The parameter d_{mesh} is the maximum side length of a mesh element, and the convergence analysis is performed for both a triangular mesh and a square mesh. In order to evaluate when the solution converges, we define a relative convergence parameter of the solution $\boldsymbol{v}_1$ with respect to the solution for the smallest mesh size $\boldsymbol{v}_1^{\text{end}}$

$$\text{"}\boldsymbol{v}_1 \text{ convergence"} = \frac{\int_\Omega \mathrm{d}A \left(|\boldsymbol{v}_1|^2 - \left|\boldsymbol{v}_1^{\text{end}}\right|^2 \right)}{\int_\Omega \mathrm{d}A \, \left|\boldsymbol{v}_1^{\text{end}}\right|^2}. \tag{5.4}$$

The relative convergence of $\boldsymbol{v}_1$ can be seen in Figure 5.3 (a), where the red line shows the results for the triangular mesh and the blue line the results for the quadratic mesh. The two curves are very similar, indicating that the two types of mesh should be equally suited for the simulation. For the relative convergence to get below 0.001, the boundary layer thickness needs to be resolved by approximately two elements, $\delta/d_{\text{mesh}} = 2$. However, since v_{1y} in general is smaller than v_{1x} by a factor of $k\delta$, Figure 5.3 (a) only shows the convergence of v_{1x}. As a further investigation we consider the relative convergence of v_{1y}, defined similarly to Eq. (5.4), which is shown in Figure 5.3 (b). The relative convergence parameter for v_{1y} is larger by an order of magnitude compared to v_{1x}, indicating that the error due to insufficient resolution of the boundary layer is more significant for v_{1y} than for v_{1x}. Furthermore, Figure 5.3 (b) shows that the quadratic mesh gives better convergence than the triangular mesh, which is unexpected. To investigate this further we plot v_{1y} along a vertical line at $x = w/4$, shown in Figure 5.3 (c) for the triangular mesh and in Figure 5.3 (d) for the quadratic mesh. This also indicates that the solution to v_{1y} is much more stable for the quadratic mesh. In order to investigate any dependence on the position of the cut line at $x = w/4$, v_{1y} was also plotted along inclined cut lines, which

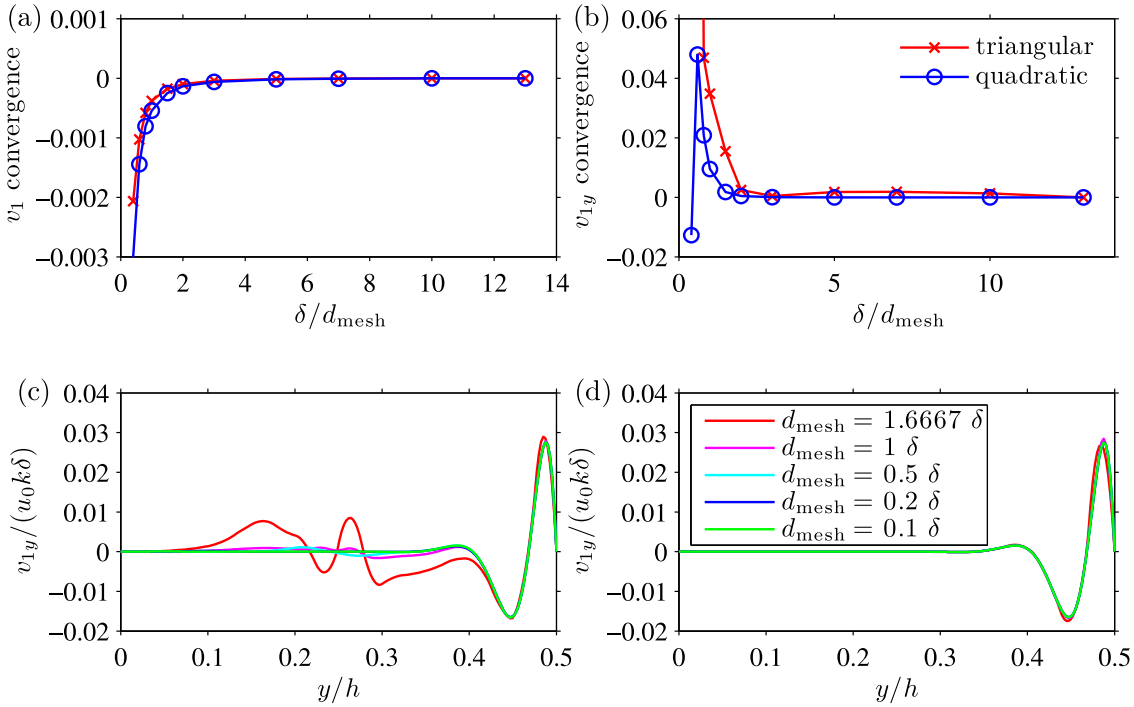

Figure 5.3: (a) Relative convergence of the first-order velocity field, $|\boldsymbol{v}_1|$, for increasing quality of the computational mesh. d_{mesh} is the side length of the mesh elements, and δ/d_{mesh} defines the resolution of the boundary layer. (b) Relative convergence of the y-component of the first-order velocity field, v_{1y}. (c) v_{1y} plotted along the vertical line at $x = w/4$ for a triangular mesh with curves for different mesh qualities. (d) v_{1y} plotted along the vertical line at $x = w/4$ for a quadratic mesh. The numerical solution seems to converge better for a quadratic mesh compared to a triangular mesh, which is unexpected.

gave the same result. It is unclear what causes this dependence on the geometry of the mesh elements. One would in general expect the triangular mesh to be slightly better as it contains approximately twice as many elements as the quadratic mesh, because we define the mesh by the side length of the mesh elements. In the further analysis a quadratic mesh is used, and we conclude that the boundary layer thickness should be resolved by approximately four mesh elements.

A further investigation of the numerical solution to the first-order problem showed that the solution did not seem to fulfill the continuity equation inside the boundary layer. A normalized expression for the continuity equation,

$$\mathrm{Re}\left(-\mathrm{i}\omega\rho_1 + \rho_0 \boldsymbol{\nabla}\cdot\boldsymbol{v}_1\right)\frac{c}{\omega\rho_0 u_0}, \tag{5.5}$$

is plotted in Figure 5.4. This should in principle be close to zero everywhere, but as the equations are expanded on a discrete mesh, and the expression Eq. (5.5) contains derivatives of the primary fields, we would in general accept errors in the order of one percent. However, as seen in Figure 5.4 the error is close to 100 percent inside the

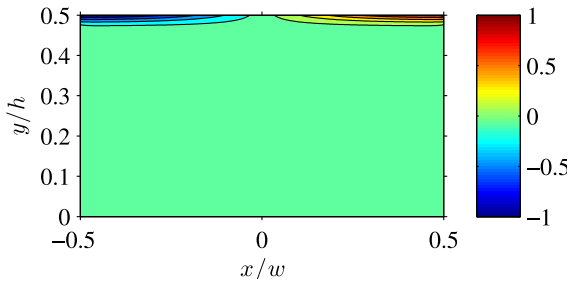

Figure 5.4: Color plot of the normalized continuity equation (5.5). The numerical solution does not fulfill the continuity equation inside the acoustic boundary layer, which indicates a possible error in the numerical model.

boundary layer. This indicates a possible error in the numerical solver or the numerical model in general. The continuity expression Eq. (5.5) was also integrated over a small area inside the boundary layer, to get an average over several mesh elements, resulting in the same magnitude of the error. In order to verify the obtained solution we suggest that the first-order problem should be solved in the time-domain as well, in order to allow for a comparison. This was not done in this work, and we continue using the Fourier domain solution, keeping in mind that it might not be correct. Furthermore, we encountered some problems with numerical oscillations along the horizontal direction. To decrease the amplitude of these we had to resolve the acoustic wavelength by several hundreds of elements.

5.3.2 Comparison to the analytical solution

The numerical and analytical solutions to the first-order velocity field are compared in Figure 5.5. v_{1x} and v_{1y} each have a real and an imaginary component due to the complex representation of the time dependence. For v_{1x} the numerical and analytical solutions are in exact agreement as shown in Figure 5.5 (a), while for v_{1y} they differ in both magnitude and form as shown in Figure 5.5 (b). However, we did not expect the numerical solution for v_{1y} to have the form of the analytical solution, since we are well aware that the analytical solution for v_{1y} does not decay away from the wall, as it theoretically should. This emphasizes the need for a better analytical solution for the first-order velocity field, in order to allow for comparison with numerical simulations.

This ends the treatment of the first-order problem. The obtained first-order fields will be used as source terms in the numerical simulations of the second-order velocity field presented in the next section.

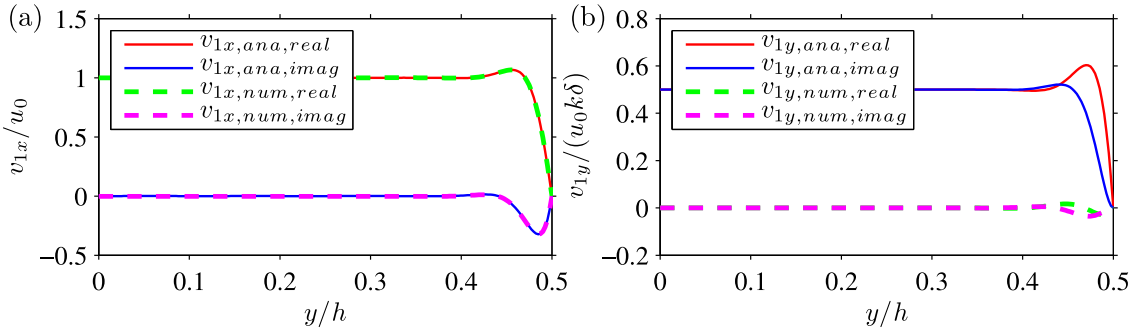

Figure 5.5: Comparison of the analytical and numerical solutions for the first-order velocity field. (a) v_{1x} plotted along vertical line at $x = 0$. The numerical solution is in exact agreement with the analytical solution. (b) v_{1y} plotted along the vertical line at $x = w/4$. The numerical solution differs from the analytical solution in both magnitude and form, which is partly expected due to the limitations of the analytical solution.

5.4 Preliminary results from a revised first-order model

In this section we briefly treat a revised first-order frequency domain model. These results have been obtained in the very end of this project, and should be considered as an outlook on how the numerical model presented in Section 5.3 should be improved in the future work. This revised numerical model is related to the discussion of the analytical first-order theory presented in the analytical outlook, Section 3.6.1.

The new assumption is that the first-order density is only independent of the wall to order $\mathcal{O}(k\delta)$, and not $\mathcal{O}(\epsilon)$ as assumed previously. To test this we propose a new first-order model in which we do not assume the ideal pressure resonance shown in Figure 5.1. Instead, we drive the model with an oscillating pressure boundary condition on the two end points of the horizontal center axis of the channel. The model is solved in the frequency domain with the physical value of the boundary layer thickness. In this model we have $w = 380\,\mu m$, $h = 160\,\mu m$, and $\delta \approx 0.003h$.

Figure 5.6 (a) shows the first-order density along the vertical line at $x = -w/4$ and normalized to its value at the horizontal center line. The first-order density increases slightly when moving towards the wall. The relative change in ρ_1 is in the order of 10^{-3}, and for this simulation we have $k\delta \approx 0.003$. This confirms the assumption that ρ_1 should be independent of y to order $\mathcal{O}(k\delta)$. The small y-dependent component of ρ_1 result in a linear component of v_{1y}, spreading into the bulk, as shown in Figure 5.6 (b).

These results are in agreement with the revision of the analytical theory, presented in Section 3.6.1. We conclude, that the numerical first-order model presented in Section 5.3 is only correct to order $\mathcal{O}(k\delta)$. To improve the model in the future work, we will have to solve the detailed dependence of ρ_1, as briefly presented in this section. The results of this section are not used in the second-order model in Section 5.5.

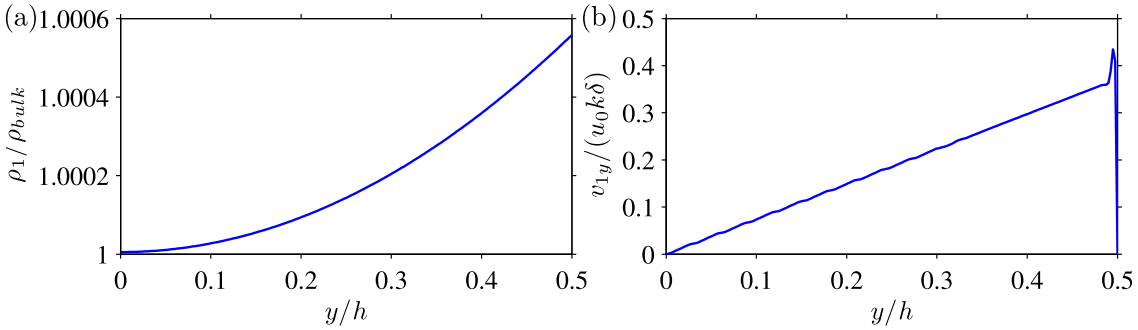

Figure 5.6: Preliminary results of the revised first-order frequency domain model. In this model the density oscillations are driven by an oscillating boundary condition, instead of assuming an ideal resonance. (a) First-order density along the vertical line at $x = -w/4$, normalized to its value at the horizontal center axis, $y/h = 0$. The density increases towards to wall at $y/h = 0.5$ following a parabola. The relative change is in the order of 10^{-3}. (b) y-component of the first-order velocity along the vertical line at $x = -w/4$, normalized to $u_0 k\delta$. v_{1y} has a linear component spreading into the bulk. These results are not used in the second-order model.

5.5 Second-order problem

In the numerical simulations of the second-order problem we use the real value of the boundary layer thickness, resulting in $\delta \approx 0.001h$ for the square channel. In order to resolve this very thin boundary layer we use an inhomogeneous mesh in which the mesh elements in the bulk is larger than those close to the wall. Close to the wall we set $\delta/d_{\text{mesh}} = 8$ to ensure that the solution has converged. The first-order problem, Section 5.3, is also solved on this mesh and afterwards used in the source terms of the time-averaged second-order equations (2.38) and (2.39). The resulting second-order velocity field is shown in Figure 5.7 for aspect ratios of 1/5, 1, and 2. The whole channel cross section is showed here, though in the simulations the symmetry in both the vertical and horizontal center line has been exploited, decreasing the computational domain by a factor of 4. The structure of the numerical solution agrees very well with the analytical iterative Fourier solution presented in Figure 4.6. The numerical velocity field in Figure 5.7 has been normalized to the theoretical acoustic streaming velocity $u_{\text{str}} = \frac{3}{8}\frac{u_0^2}{c}$, and the magnitude of numerical solution is seen to be approximately one third of the analytical solution. Figure 5.8 (a) shows a zoom in close to the top wall with a color plot of $\langle v_{2x} \rangle$. From this we can see that the numerical simulations also describe the inner streaming rolls, however, the magnitude of the inner streaming rolls in the numerical solution is comparable to that of the outer streaming rolls, which is different from the analytical solution. Figure 5.8 (b) shows the maximum and minimum of $\langle v_{2x} \rangle$, each representing the magnitude of the inner and outer streaming roll, respectively, versus the aspect ratio of the channel. From the analytical derivation we expect the solution inside the boundary layer to be independent of the channel aspect ratio, which leads to the definition of the acoustic streaming boundary condition for the bulk velocity field. For the numerical solution we see that the magnitude of the acoustic streaming depends on the aspect ratio when below unity. This is unexpected and might be a consequence of the problems pointed out in Section 5.3.1 in relation to the numerical solution of the first-order problem.

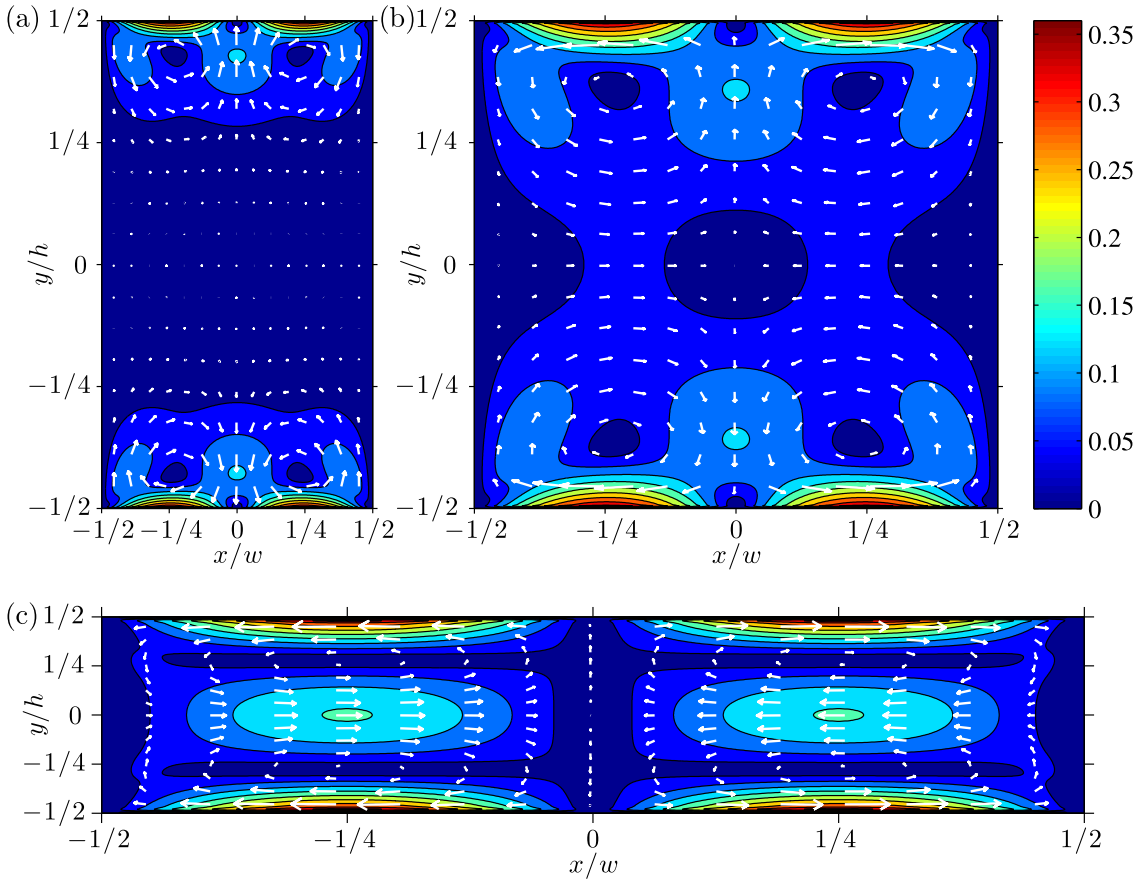

Figure 5.7: Color and vector plot of the numerical solution for the time-averaged second-order velocity $\langle \boldsymbol{v}_2 \rangle$, normalized to the analytical acoustic streaming velocity u_{str}. The velocity field is shown for three aspect ratios; (a) $h/w = 2$, (b) $h/w = 1$, and (c) $h/w = 1/5$. The structure of the field inside the boundary layer is not resolved as $\delta \approx 0.001w$. The structure of the numerical velocity field is in good agreement with the analytical iterative Fourier solution shown in Figure 4.6. However, the magnitude of the numerical velocity field is approximately three times smaller.

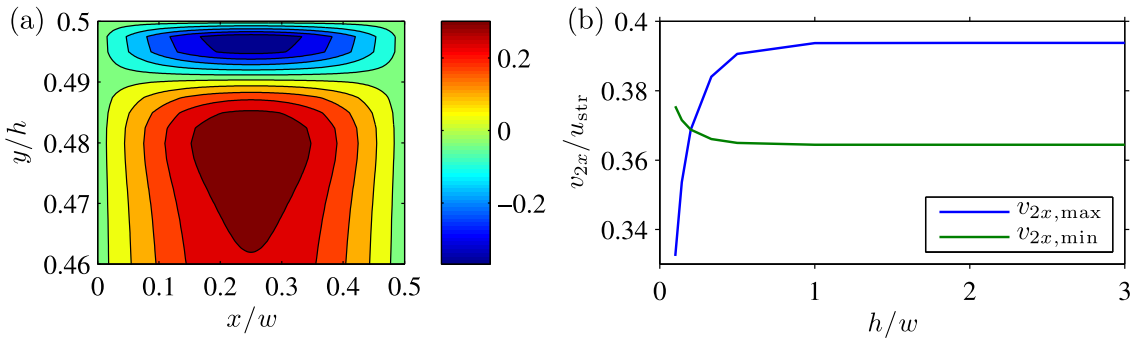

Figure 5.8: (a) Color plot of the numerical solution for $\langle v_{2x} \rangle$ close to the top wall for a channel aspect ratio of $h/w = 1/5$. The boundary layer thickness is $\delta = 0.005h$. The magnitude of the inner streaming roll is the same as the magnitude of the outer streaming roll. (b) Plot of the minimum and maximum values of $\langle v_{2x} \rangle$, which sets the magnitude of the inner and outer streaming rolls, respectively. The solution inside the boundary layer depends on the aspect ratio, for aspect ratios below unity, which contradicts the analytical prediction of an independent boundary solution.

5.6 Validation of the analytical iterative Fourier approach

In order to validate the iterative Fourier expansion approach for acoustic streaming in rectangular channels we make a numerical simulation of the time-averaged second-order bulk velocity field, using the analytical acoustic streaming boundary condition Eqs. (4.2d) and (4.2e). In these simulations, the acoustic boundary layer is not resolved, and only the analytical derivation of Section 4.3.3 is validated. The result of this simplified numerical model is shown in Figure 5.9, while the absolute difference between this numerical solution and the analytical iterative Fourier solution is shown in Figure 5.10. The largest absolute difference is $0.02u_{\mathrm{str}}$, and these small differences generally seem to be caused by the discretization of the fields. It can thus be concluded that the analytical solution is in exact agreement with the numerical solution based on the acoustic streaming boundary condition for the bulk velocity field.

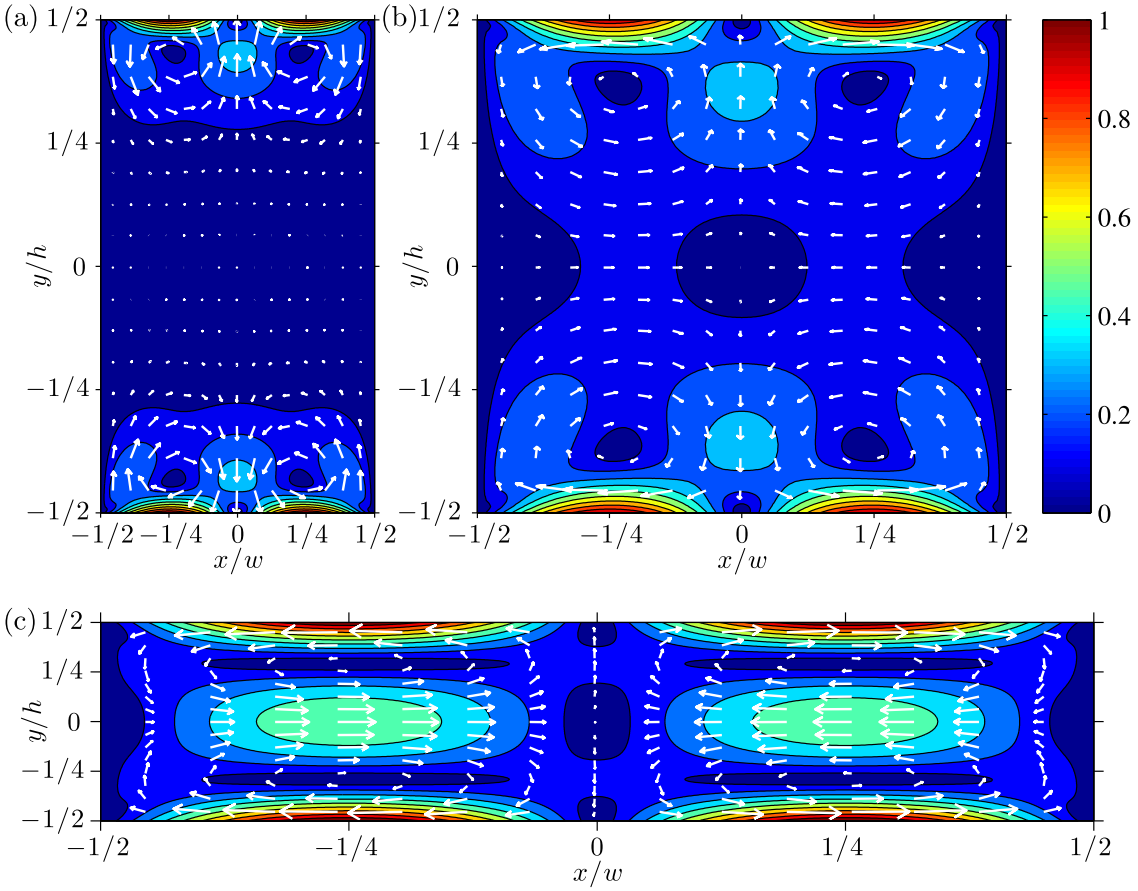

Figure 5.9: Color and vector plot of the time-averaged second-order bulk velocity field $\langle \boldsymbol{U}_2 \rangle$ calculated using a simplified numerical model based on the analytical acoustic streaming boundary condition Eqs. (4.2d) and (4.2e). The numerical results are in exact agreement with the analytical iterative Fourier expansion solution shown in Figure 4.6.

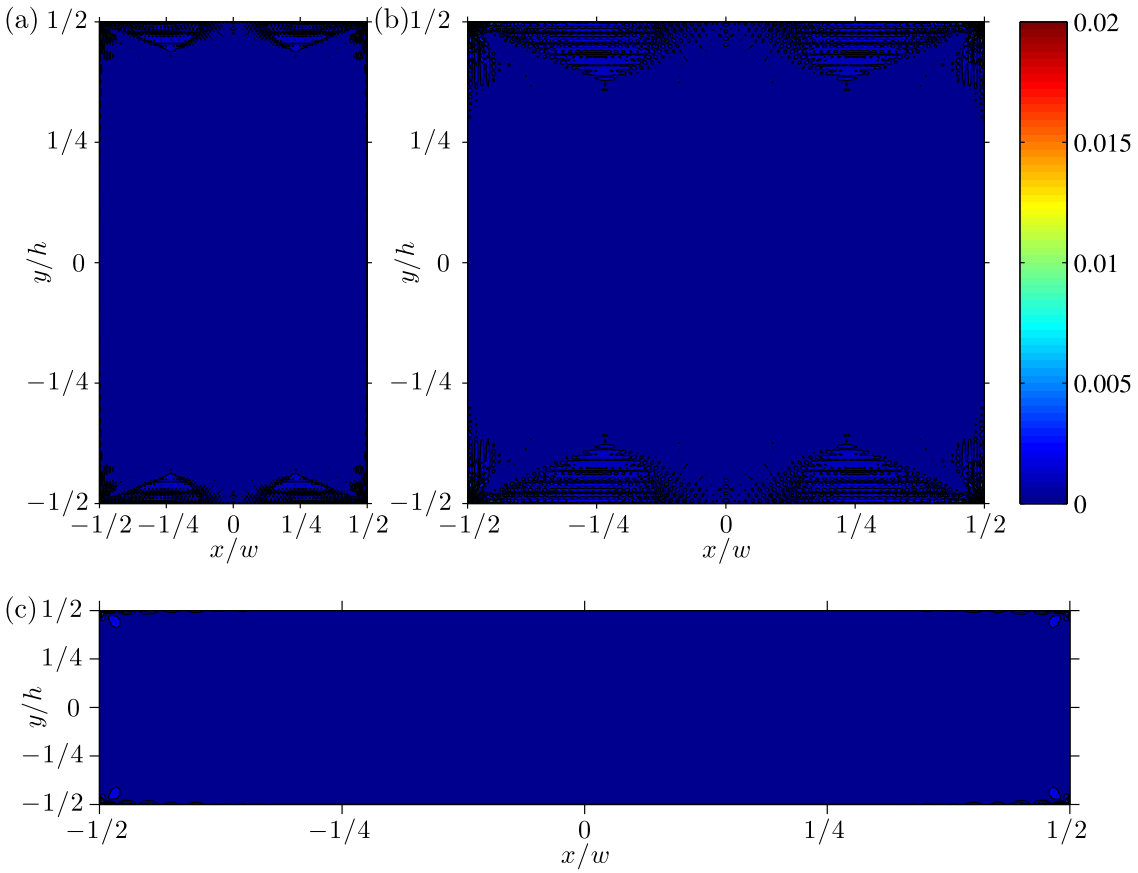

Figure 5.10: Color plot of the absolute difference in $\langle \boldsymbol{U}_2 \rangle$ between the analytical iterative Fourier solution, shown in Figure 4.6, and the simplified numerical solution, show in Figure 5.9. The largest difference is approximately $0.02 u_{\text{str}}$, and generally the differences seem to be caused by the discretization of the fields.

5.7 Concluding remarks

We have proposed a numerical scheme based an a perturbation approach to second order. The first-order problem is solved in the frequency domain, and the time-averaged second-order problem is solved time-independently. The convergence analysis of the first-order velocity field, for increasing mesh quality, showed that a quadratic mesh resulted in better convergence compared to a rectangular mesh. Comparing the numerical and analytical first-order solutions, the x-component of the first-order velocity field was in exact agreement, while the y-component differed in both magnitude and form. Moreover, it seemed that the numerical solution to the first-order problem did not fulfill the continuity equation inside the boundary layer. This indicates a possible error in the numerical model, and we have suggested a comparison to a numerical time domain solution.

The numerical solution to the time-averaged second-order problem showed the same tendencies as the analytical solution, while the magnitude was lower by a factor of 3, approximately. Furthermore, in the numerical solution the magnitude of the velocity field inside the boundary layer was dependent on the aspect ratio of the channel. This contradicts the analytical prediction of an independent boundary layer solution, and could be due to the error of the first-order solution inside the boundary layer.

We have proposed a simplified numerical model, based on the analytical acoustic streaming boundary condition for the bulk velocity field, and the results of this model were in exact agreement with the analytical solution of the iterative Fourier expansion approach.

5.7.1 Numerical outlook

As pointed out in Section 5.4, the assumption of the ideal resonance of the first-order density is only correct to order $\mathcal{O}(k\delta)$. In order to improve the numerical results we should instead drive the density oscillations by applying an oscillating boundary condition or an oscillating bulk force. This will also make the numerical simulations more independent of the analytical assumptions.

Chapter 6

Experimental outlook

This chapter is an experimental outlook, in which we discuss the challenges of measuring acoustic streaming in microfluidic channels. The acoustic streaming, resulting from a transverse pressure resonance, is in the vertical cross-sectional plane of the microchannel, as previously illustrated in Figure 1.1. This is difficult to measure because we only have visual access from the top through the transparent glass lid. With conventional microscopy, using a spherical lens, we can achieve pictures such as the one shown in Figure 6.1 (b). A spherical lens has one focal plane, at which the object is focused in both horizontal directions, denoted x and z in Figure 6.1 (a). Particles above and below the focal plane are defocused in the same way, and thus cannot be told apart. A cylindrical lens has two focal planes, one in which the object is focused in the x-direction and one in which the object is focused in the z-direction, as sketched in Figure 6.1 (c). Consequently, the shape of the particles relate to their y-position in the channel. From an image, as the one shown in Figure 6.1 (d), all three coordinates of the particle positions can be obtained, using proper calibration [53, 54]. By comparison of successive images, all three components of the particle velocities can be obtained, referred to as astigmatism particle tracking velocimetry. This provides a promising technique for measuring the acoustic streaming velocity field in the vertical cross-sectional plane of the microchannel.

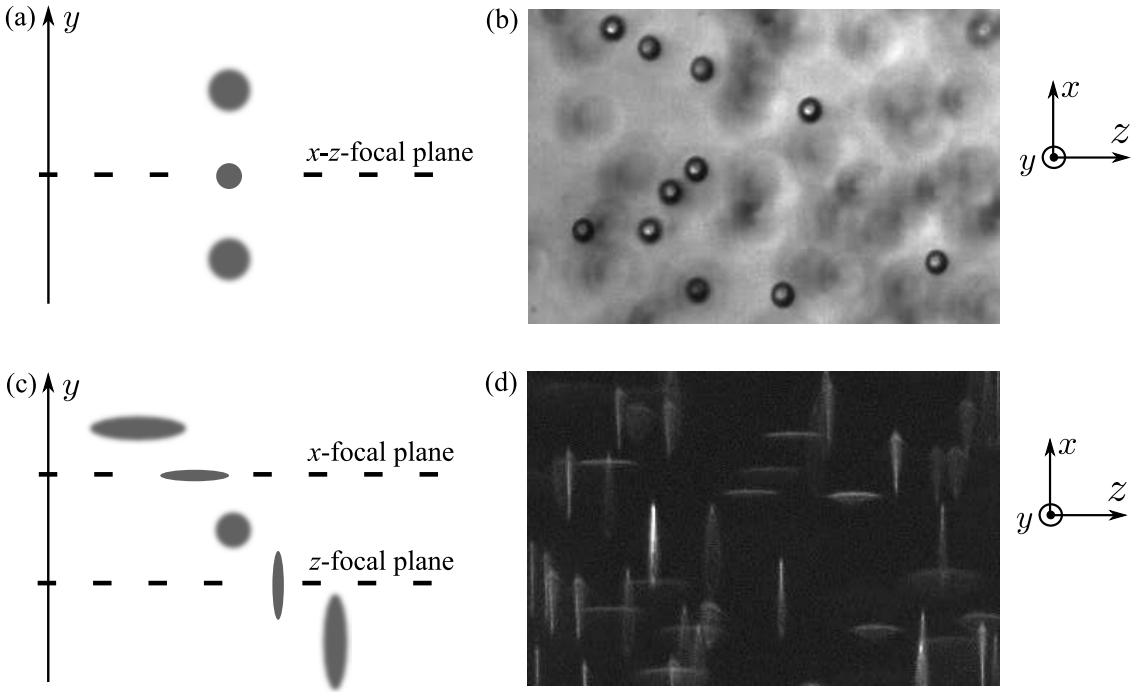

Figure 6.1: Comparison of microscopy using spherical and cylindrical lenses. (a) Sketch of how a particle is defocused in conventional microscopy using a spherical lens, which only has one focal plane. The particles above and below the focal plane cannot be told apart. (b) Image of 10 µm particles in a microfluidic channel acquired using a spherical lens. (c) Sketch of how a particle is defocused when using a cylindrical lens, which has two focal planes. The shape of the particles relates to its y-position in the channel. (d) Image of 1 µm particles in a microfluidic channel acquired using a cylindrical lens. The particles are spherical but their shapes have been distorted when viewing through the cylindrical lens. This technique can be used to measure all three components of the particle velocity by comparing successive images, denoted astigmatism particle tracking velocimetry [53, 54]. The images are accredited to (b) Per Augustsson and Rune Barnkob, and (d) Massimiliano Rossi and Álvaro Gómez Marín.

Chapter 7

Conclusion

In this thesis we have presented analytical and numerical studies of the acoustic streaming in microfluidic channels. The general approach is based on a perturbation expansion of the physical fields to second order, while only isothermal systems have been considered.

Based on a literature study, we have pointed out an inconsistency in the common approach to the problem of acoustic streaming, regarding the assumption of incompressibility of the fluid close to the boundaries. We have proposed a novel approach to the problem of acoustic streaming, in which the fluid is considered compressibility everywhere, and the first-order velocity field is decomposed into a compressible inviscid term and an incompressible viscous term. This approach leads to an acoustic streaming boundary condition for the second-order bulk velocity field in agreement with the results of Rayleigh [1]. We have emphasized that the accuracy of the analytical solution is limited by the solution to the first-order velocity field, and stressed the need for further improvement.

We have derived the analytical solution for the acoustic streaming in parallel-plates channels, for which the channel height is comparable to the acoustic wavelength. Furthermore, we have treated the acoustic streaming in rectangular channels, taken into account the effects of the no-slip boundary condition on the side walls. This is relevant for channels used in acoustofluidic devices, which often have a width to height ratio close to unity. We have proposed an iterative Fourier expansion of the second-order velocity field, and showed that the solution converges well. Using this approach the acoustic streaming velocity field for the rectangular channel has been determined to arbitrary high precision, by including sufficient iterations and Fourier components. This allows for prediction of the acoustic streaming in acoustofluidic devices, and can be used in future comparison of theory and experiments, presenting an important contribution to the theory of acoustic streaming and the research field of acoustofluidics, as indicated in Figure 7.1. We have also proposed a simpler approximate solution to the acoustic streaming in a rectangular channel, given by the solution to the parallel-plates channel multiplied by an envelope function. The root mean square deviation of the envelope solution, with respect to the

$\delta \ll h \ll \lambda$ (parallel-plates channel) Rayleigh [Kundt's tube]	$\delta \ll h \sim \lambda$ (rectangular channel) Muller [microfluidic acoustophoresis]
$\delta \sim h \ll \lambda$ (parallel-plates channel) Hamilton [thermoacoustic engine]	$\delta \sim h \sim \lambda$

Figure 7.1: Overview of the different cases of acoustic streaming as shown previously in Figure 1.4. The iterative Fourier expansion approach, proposed in this work, allows for theoretical determination of the acoustic streaming in rectangular channels in the case of $\delta \ll h \sim \lambda$. This enables prediction of the acoustic streaming in experimental acoustophoresis devices, and thus presents an important contribution to the theory of acoustic streaming and the acoustofluidic research field.

iterative Fourier solution, was approximately half that of the parallel-plates solution.

In addition to the analytical work, we have presented numerical models of acoustic streaming in rectangular channels. Due to the different time scales governing the oscillating first-order fields and the steady second-order fields, the perturbation approach has also been employed in the numerical models. We have solved the first-order problem in the frequency domain and the second-order problem time-independently. The numerical results showed tendencies in agreement with the analytical solution, however, deviations close to the boundaries indicated a possible error in the numerical model. Consequently, we have suggested a comparison with a time-dependent numerical solution of the first-order problem. We have also proposed a simplified numerical model, assuming the analytical acoustic streaming boundary condition for the bulk flow, by which we achieved results in exact agreement with the analytical iterative Fourier solution.

Finally, we have emphasized the need for both analytical, numerical, and experimental results for acoustic streaming, and discussed the design of experimental measurements in order to allow for quantitative comparison. The technique of astigmatism particle tracking velocimetry has been proposed as a promising method for quantitative measurements of the acoustic streaming velocity field in microfluidics channels.

7.1 Outlook

In the present work we have improved the understanding of acoustic streaming in relation to acoustofluidic devices. Nevertheless, many challenges remain in achieving good analytical, numerical, and experimental results of acoustic streaming. The present work will be continued by the author of this thesis in the PhD-project "Theory and design of microsystems for clinical acousto-activated cell sorting" in the group of Henrik Bruus.

As stressed in Sections 3.6.1 and 5.4 the accuracy of both the analytical and numerical treatment is limited by the assumption of an ideal resonance for the first-order density perturbation. The first-order problem should be reconsidered without this assumption. According to the preliminary analytical considerations, this will remove the need for the artificial bounding of the first-order velocity field in the analytical treatment. The preliminary numerical results indicate a parabolically y-dependent component of the first-order density and a linear y-component of the first-order velocity.

As this work only considers isothermal systems, it would be relevant to investigate the influence of temperature variations. Besides the thermodynamic temperature oscillations, temperature variations induced by the acoustic actuation and microscope illumination could also be considered. The temperature dependence of the viscosity is suggested as the primary point of influence of the temperature variations.

Another point of interest would be to consider cases in which the second viscosity becomes important, in our formulation expressed through $\beta\eta$. In our approach, β is assumed to be $\frac{1}{3}$, though it can be significantly larger in some special cases at high frequencies [57].

In order to check the numerical solution it would be relevant solve the first-order problem using different models, such as solving the problem in the time domain and with the oscillating force applied in different ways. When satisfying results for the acoustic streaming in a rectangular channel are achieved, the numerical scheme should be generalized for application on other more complex geometries, resembling the channel geometries of experimental acoustofluidic devices.

So far we have only considered the microfluidic channel itself, neglecting the influence of the surrounding chip material. However, previous work in the group of Bruus by Barnkob [61] shows that the surrounding chip material greatly influences the acoustic resonance in the microchannel. The numerical scheme for calculation of the acoustic streaming should be combined with the numerical scheme for calculation of pressure resonance presented by Barnkob, together presenting a powerful tool for prediction of the acoustic streaming in experimental acoustofluidic devices.

Comparison to experimental measurements is important for the usefulness of the analytical and numerical work. At this stage this requires experiments designed to be as simple as possible. Measurements obtained by astigmatism particle tracking velocimetry should be used for benchmarking of the analytical and numerical results.

The increased understanding of acoustic streaming should be used to optimize current acoustofluidic applications and develop new ones. This concerns both application utilizing the acoustic streaming, but also application utilizing the acoustic radiation force, in which the acoustic streaming can be an unwanted side effect. One example could be separation by the acoustic radiation force of small particle usually dominated by acoustic streaming. This might be achieved by using a horizontal resonance in a channel with a large height to width ratio, as the acoustic streaming is significant only close the top and bottom wall, as was seen in Figure 4.6 (a).

Appendix A

Calculation of the vorticity source density

In this appendix we derive the expression Eq. (3.12) for the time-averaged second-order vorticity source density, $\langle S(x,y)\rangle$.

Introducing the complex function

$$C(y) = \frac{1}{\kappa}\left(1-\mathrm{e}^{-\kappa y}\right), \tag{A.1}$$

the first-order fields, Eqs. (3.1) and (3.4), can be written as

$$U_{1x} = u_0\cos(kx)\,\mathrm{e}^{-\mathrm{i}\omega t}, \tag{A.2a}$$
$$u_{1x} = -u_0\cos(kx)\,C'(y)\,\mathrm{e}^{-\mathrm{i}\omega t}, \tag{A.2b}$$
$$u_{1y} = -u_0 k\sin(kx)\,C(y)\,\mathrm{e}^{-\mathrm{i}\omega t}. \tag{A.2c}$$

For clarity we restating the expression for the time-average second-order vorticity source density Eq. (3.12)

$$\langle S(x,y)\rangle = -3\langle U_{1x}\partial_y\partial_x u_{1x}\rangle - \langle u_{1x}\partial_y\partial_x u_{1x}\rangle - \left\langle u_{1y}\partial_y^2 u_{1x}\right\rangle. \tag{A.3}$$

The time average of two variables

$$A(r,t) = a(r)\,\mathrm{e}^{-\mathrm{i}\omega t}, \tag{A.4a}$$
$$B(r,t) = b(r)\,\mathrm{e}^{-\mathrm{i}\omega t}, \tag{A.4b}$$

can be expressed as

$$\langle A(r,t)\,B(r,t)\rangle = \frac{1}{2}\mathrm{Re}\left\{a(r)^*\,b(r)\right\}, \tag{A.5}$$

where the asterisk denotes the complex conjugate. Using the rule Eq. (A.5) and the first-order fields Eq. (A.2), each term of Eq. (A.3) become

$$-3\left\langle U_{1x}\partial_y\partial_x u_{1x}\right\rangle = -\frac{3}{4}u_0^2 k\sin\left(2kx\right)\mathrm{Re}\left\{C''\left(y\right)\right\}, \tag{A.6a}$$

$$-\left\langle u_{1x}\partial_y\partial_x u_{1x}\right\rangle = \frac{1}{4}u_0^2 k\sin\left(2kx\right)\mathrm{Re}\left\{C''\left(y\right)C'^{*}\left(y\right)\right\}, \tag{A.6b}$$

$$-\left\langle u_{1y}\partial_y^2 u_{1x}\right\rangle = -\frac{1}{4}u_0^2 k\sin\left(2kx\right)\mathrm{Re}\left\{C^{*}\left(y\right)C'''\left(y\right)\right\}. \tag{A.6c}$$

Inserting in Eq. (A.3) the source density becomes

$$\begin{aligned}\left\langle S\left(x,y\right)\right\rangle = \frac{1}{4}u_0^2 k\sin\left(2kx\right)\Big[&-3\mathrm{Re}\left\{C''\left(y\right)\right\}+\mathrm{Re}\left\{C''\left(y\right)C'^{*}\left(y\right)\right\}\\ &-\mathrm{Re}\left\{C^{*}\left(y\right)C'''\left(y\right)\right\}\Big].\end{aligned} \tag{A.7}$$

The right hand terms become

$$-3\mathrm{Re}\left\{C''\left(y\right)\right\} = 3\frac{1}{\delta}e^{-y/\delta}\left\{\cos\left(y/\delta\right)+\sin\left(y/\delta\right)\right\}, \tag{A.8a}$$

$$\mathrm{Re}\left\{C''\left(y\right)C'^{*}\left(y\right)\right\} = -\frac{1}{\delta}\mathrm{e}^{-2y/\delta}, \tag{A.8b}$$

$$-\mathrm{Re}\left\{C^{*}\left(y\right)C'''\left(y\right)\right\} = \frac{1}{\delta}e^{-y/\delta}\left\{\cos\left(y/\delta\right)-\sin\left(y/\delta\right)\right\}-\frac{1}{\delta}\mathrm{e}^{-2y/\delta}. \tag{A.8c}$$

Inserting in Eq. (A.7) yields

$$\left\langle S\left(x,y\right)\right\rangle = \frac{1}{2}u_0^2 k\frac{1}{\delta}\sin\left(2kx\right)e^{-y/\delta}\left[2\cos\left(y/\delta\right)+\sin\left(y/\delta\right)-\mathrm{e}^{-y/\delta}\right]. \tag{A.9}$$

Bibliography

[1] L. Rayleigh, "On the Circulation of Air Observed in Kundt's Tubes, and on Some Allied Acoustical Problems," *Philosophical Transactions Series I*, vol. 175, pp. 1–21, 1884.

[2] G. Karniadakis and A. Beskok, *Micro flows: fundamentals and simulation*. Springer-Verlag, New York, 2002.

[3] O. Geschke, H. Klank, and P. Telleman, *Microsystem engineering of lab-on-a-chip devices*. Wiley-VCH Verlag, Weinheim, 2004.

[4] P. Tabeling, *Introduction to Microfluidics*. Oxford: Oxford University Press, 2005.

[5] H. Bruus, *Theoretical Microfluidics*. Oxford: Oxford University Press, 2008.

[6] J. Berthier and P. Silberzan, *Microfluidics for Biotechnology*. Norwood MA: Artech House, second ed., 2010.

[7] H. Stone, A. Stroock, and A. Ajdari, "Engineering flows in small devices: Microfluidics toward a lab-on-a-chip," *Annu. Rev. Fluid Mech.*, vol. 36, pp. 381–411, 2004.

[8] T. M. Squires and S. R. Quake, "Microfluidics: Fluid physics at the nanoliter scale," *Review of modern physics*, vol. 77, pp. 977–1026, 2005.

[9] G. M. Whitesides, "The origins and the future of microfluidics," *Nature*, vol. 442, pp. 368–373, 2006.

[10] M. Faraday, "On a Peculiar Class of Acoustical Figures; and on Certain Forms Assumed by Groups of Particles upon Vibrating Elastic Surfaces," *Philosophical Transactions of the Royal Society of London*, vol. 121, pp. 299–340, 1831.

[11] A. Kundt and O. Lehmann, "Longitudinal vibrations and acoustic figures in cylindrical columns of liquids," *Ann. Phys. Chem.*, vol. 153, p. 1, 1874.

[12] L. V. King, "On the acoustic radiation pressure on spheres," *P Roy Soc Lond A Mat*, vol. 147, no. 861, pp. 212–240, 1934.

[13] H. Schlicthing, "Berechnung ebener periodischer grenzeschichtströmungen," *Physicalische Zeitschrift*, vol. 33, pp. 327 – 335, 1932.

[14] C. Eckart, "Vortices and streams caused by sound waves," *Phys Rev*, pp. 68–76, 1948.

[15] J. Markham, R. T. Beyer, and R. B. Lindsay, "Absorption of Sound in Fluids," *Reviews of Modern Physics*, vol. 23, no. 4, pp. 353–411, 1951.

[16] J. Markham, "Second-Order Acoustic Fields: Streaming with Viscosity and Relaxation," *Physical Review*, vol. 86, no. 4, pp. 497–502, 1952.

[17] J. Markham, "Second-Order Acoustic Fields: Energy Relations," *Physical Review*, vol. 86, no. 5, pp. 712–714, 1952.

[18] J. Markham, "Second-Order Acoustic Fields: Relations Between Density and Pressure," *Physical Review*, vol. 86, no. 5, pp. 710–711, 1952.

[19] J. Markham, "Second-Order Acoustic Fields: Relations between Energy and Intensity," *Physical Review*, vol. 89, no. 5, pp. 972–977, 1953.

[20] W. L. Nyborg, "Acoustic streaming due to attenuated plane waves," *Journal of the Acoustical Society of America*, vol. 25, pp. 68–75, 1953.

[21] W. L. Nyborg, "Acoustic streaming near a boundary," *Journal of the Acoustical Society of America*, vol. 30, no. 4, pp. 329–339, 1958.

[22] W. L. Nyborg, "Radiation pressure on a small rigid sphere," *Journal of the Acoustical Society of America*, vol. 42, no. 5, pp. 947–952, 1967.

[23] K. Yosioka and Y. Kawasima, "Acoustic radiation pressure on a compressible sphere," *Acustica*, vol. 5, pp. 167–173, 1955.

[24] L. P. Gorkov, "On the forces acting on a small particle in an acoustical field in an ideal fluid," *Soviet Physics - Doklady*, vol. 6, no. 9, pp. 773–775, 1962.

[25] M. F. Hamilton, Y. A. Ilinskii, and E. A. Zabolotskaya, "Acoustic streaming generated by standing waves in two-dimensional channels of arbitrary width," *J. Acoust. Soc. Am.*, vol. 113, p. 153, 2003.

[26] M. Settnes and H. Bruus, "Forces acting on a small particle in an acoustical field in a viscous fluid," *Phys Rev E*, vol. 85, p. 016327, 2012.

[27] S. Boluriaan and P. Morris, "Acoustic streaming: from rayleigh to today," *Int. J. Aeroacoustics*, vol. 2, pp. 255–292, 2003.

[28] J. Friend and L. Y. Yeo, "Microscale acoustofluidics: Microfluidics driven via acoustics and ultrasonics," *Rev Mod Phys*, vol. 83, no. 2, pp. 647–704, 2011.

[29] H. Bruus, J. Dual, J. Hawkes, M. Hill, T. Laurell, J. Nilsson, S. Radel, S. Sadhal, and M. Wiklund, "Forthcoming lab on a chip tutorial series on acoustofluidics: Acoustofluidics-exploiting ultrasonic standing wave forces and acoustic streaming in microfluidic systems for cell and particle manipulation," *Lab Chip*, vol. 11, no. 21, pp. 3579–3580, 2011.

[30] K. Yasuda, S. Umemura, and K. Takeda, "Concentration and fractionation of small particles in liquid by ultrasound," *Jpn J Appl Phys*, vol. 34, no. 5B, pp. 2715–2720, 1995.

[31] K. Yasuda, K. Takeda, and S.-i. Umemura, "Studies on particle separation by acoustic radiation force and electrostatic force," *Japanese Journal of Applied Physics, Part 1: Regular Papers & Short Notes & Review Papers*, vol. 35, no. 5B, pp. 3295–3299, 1996.

[32] J. Spengler and M. Jekel, "Ultrasound conditionering of suspensions - studies of streaming influence on particle aggregation on a lab- and pilot-plant scale," *Ultrasonics*, vol. 38, p. 624, 2000.

[33] J. Spengler, W. Coakley, and K. Christensen, "Microstreaming effects on particle concentration in an ultrasonic standing wave," *AIChE Journal*, vol. 49, no. 11, pp. 2773–2782, 2003.

[34] M. Wiklund, P. Spégel, S. Nilsson, and H. M. Hertz, "Ultrasonic-trap-enhanced selectivity in capillary electrophoresis," *Ultrasonics*, vol. 41, no. 4, pp. 329–333, 2003.

[35] L. A. Kuznetsova and W. T. Coakley, "Microparticle concentration in short path length ultrasonic resonators: Roles of radiation pressure and acoustic streaming," *Journal of the Acoustical Society of America*, vol. 116, no. 4, pp. 1956–1966, 2004.

[36] A. Nilsson, F. Petersson, H. Jönsson, and T. Laurell, "Acoustic control of suspended particles in micro fluidic chips," *Lab Chip*, vol. 4, no. 2, pp. 131–5, 2004.

[37] F. Petersson, A. Nilsson, C. Holm, H. Jönsson, and T. Laurell, "Separation of lipids from blood utilizing ultrasonic standing waves in microfluidic channels," *Analyst*, vol. 129, no. 10, pp. 938–43, 2004.

[38] F. Petersson, A. Nilsson, C. Holm, H. Jönsson, and T. Laurell, "Continuous separation of lipid particles from erythrocytes by means of laminar flow and acoustic standing wave forces," *Lab Chip*, vol. 5, no. 1, pp. 20–22, 2005.

[39] H. Li and T. Kenny, "High speed particles separation using ultrasound for microtas and lab-on-a-chip application," in *Proc. 26th Annual International Conference of the Engineering in Medicine and Biology Society EMBC 2004*, vol. 1, pp. 2631–2634, 2004.

[40] M. Bengtsson and T. Laurell, "Ultrasonic agitation in microchannels," *Anal Bioanal Chem*, vol. 378, no. 7, pp. 1716–1721, 2004.

[41] H. Jönsson, C. Holm, A. Nilsson, F. Petersson, P. Johnsson, and T. Laurell, "Particle separation using ultrasound can radically reduce embolic load to brain after cardiac surgery," *Annals of Thoracic Surgery*, vol. 78, no. 5, pp. 1572–1578, 2004.

[42] T. Lilliehorn, U. Simu, M. Nilsson, M. Almqvist, T. Stepinski, T. Laurell, J. Nilsson, and S. Johansson, "Trapping of microparticles in the near field of an ultrasonic transducer," *Ultrasonics*, vol. 43, no. 5, pp. 293–303, 2005.

[43] S. M. Hagsäter, A. Lenshof, P. Skafte-Pedersen, J. Kutter, T. Laurell, and H. Bruus, "Acoustic resonances in straight microchannels: Beyond the 1D-approximation," *Lab on a Chip*, vol. 8, pp. 1178–1184, 2008.

[44] O. Manneberg, S. M. Hagsäter, J. Svennebring, H. M. Hertz, J. P. Kutter, H. Bruus, and M. Wiklund, "Spatial confinement of ultrasonic force fields in microfluidic channels," *Ultrasonics*, vol. 49, no. 1, pp. 112–119, 2009.

[45] O. Manneberg, B. Vanherberghen, B. Onfelt, and M. Wiklund, "Flow-free transport of cells in microchannels by frequency-modulated ultrasound," *Lab Chip*, vol. 9, no. 6, pp. 833–837, 2009.

[46] J. Svennebring, O. Manneberg, P. Skafte-Pedersen, H. Bruus, and M. Wiklund, "Selective bioparticle retention and characterization in a Chip-Integrated confocal ultrasonic cavity," *Biotechnol Bioeng*, vol. 103, no. 2, pp. 323–328, 2009.

[47] A. Lenshof, A. Ahmad-Tajudin, K. Jaras, A.-M. Sward-Nilsson, L. Aberg, G. Marko-Varga, J. Malm, H. Lilja, and T. Laurell, "Acoustic whole blood plasmapheresis chip for prostate specific antigen microarray diagnostics," *Anal Chem*, vol. 81, no. 15, pp. 6030–6037, 2009.

[48] C. Grenvall, P. Augustsson, J. R. Folkenberg, and T. Laurell, "Harmonic microchip acoustophoresis: A route to online raw milk sample precondition in protein and lipid content quality control," *Anal Chem*, vol. 81, no. 15, pp. 6195–6200, 2009.

[49] T. Franke, S. Braunmueller, L. Schmid, A. Wixforth, and D. A. Weitz, "Surface acoustic wave actuated cell sorting (SAWACS)," *Lab Chip*, vol. 10, no. 6, pp. 789–794, 2010.

[50] P. Thevoz, J. D. Adams, H. Shea, H. Bruus, and H. T. Soh, "Acoustophoretic synchronization of mammalian cells in microchannels," *Anal Chem*, vol. 82, no. 7, pp. 3094–3098, 2010.

[51] R. Barnkob, P. Augustsson, T. Laurell, and H. Bruus, "Measuring the local pressure amplitude in microchannel acoustophoresis," *Lab Chip*, vol. 10, no. 5, pp. 563–570, 2010.

[52] P. Augustsson, R. Barnkob, S. T. Wereley, H. Bruus, and T. Laurell, "Automated and temperature-controlled micro-piv measurements enabling long-term-stable microchannel acoustophoresis characterization," *Lab Chip*, vol. 11, no. 24, pp. 4152–4164, 2011.

[53] C. Cierpka, M. Rossi, R. Segura, F. Mastrangelo, and C. J. Kähler, "A simple single camera 3c3d velocity measurement technique without errors due to depth of correlation and spatial averaging for micro fluidics," *Meas. Sci. Technol.*, vol. 21, p. 045401, 2010.

[54] A. Kumar, C. Cierpka, S. J. Williams, C. J. Kähler, and S. T. Wereley, "3d3c velocimetry measurements of an electrothermal microvortex using wavefront deformation ptv and a single camera," *Microfluid. Nanofluid.*, vol. 10, pp. 355–365, 2011.

[55] "`http://sv.wikipedia.org/wiki/Fil:Kundt%27s_tube_DE.svg`," March 2012.

[56] L. Prandtl, "Über flüssigkeitsbewegung bei sehr kleiner reibung," *Verhandlungen des dritten internationalen Mathematiker-Kongresses in Heidelberg 1904*, p. 484, 1905.

[57] L. D. Landau and E. M. Lifshitz, *Fluid Mechanics*, vol. 6, Course of Theoretical Physics. Oxford: Pergamon Press, second ed., 1993.

[58] T. G. Jensen, "Acoustic radiation in microfluidic systems," Master's thesis, MIC — Department of Micro and Nanotechnology, DTU — Technical University of Denmark, April 2007. http://www.nanotech.dtu.dk/microfluidics.

[59] P. Skafte-Pedersen, "Acoustic forces on particles and liquids in microfluidic systems," Master's thesis, DTU Nanotech, January 2008. http://www.nanotech.dtu.dk/microfluidics.

[60] L. M. Andersen, A. Nysteen, and M. Settnes, "Forces acting on microparticles in acoustofluidic systems," bachelor thesis, DTU Nanotech, June 2009. http://www.nanotech.dtu.dk/microfluidics.

[61] R. Barnkob, "Acoustofluidics in microsystems: investigation of resonances," Master's thesis, Technical University of Denmark, www.nanotech.dtu.dk/microfluidics, 2009.

[62] H. Bruus, "Acoustofluidics 2: Perturbation theory and ultrasound resonance modes," *Lab Chip*, vol. 12, pp. 20–28, 2012.

[63] S. Sadhal, "Acoustofluidics 13: Analysis of acoustic streaming by singular perturbation," *Lab Chip*, vol. in press, p. (Tutorial Part 13), 2011.

[64] COMSOL AB, *COMSOL Multiphysics User's Guide*, March 2012. Version 4.2a.